Astrophysical S-factor calculation for selected reactions

Author:
Carlos Alberto Calvachi Salas
201822667

Final project submitted in partial fulfillment of the requirements for the degree of

Physicist

Advisor:
Neelima Govind Kelkar Ph.D.

Universidad de los Andes
Physics Department
December, 2022
Bogotá, Colombia

Abstract

Review on relevant elements of nuclear astrophysics.

Definition, motivation and applications of the astrophysical S-factor.

Survey on models that predict S-factors. They are mainly classified as empirical, potential, macroscopic and matrix models

Use of theoretical models to calculate the S-factors of selected reactions.

Comment on the applicability of the models for each reaction. Comparison between experimental data and theoretical predictions of the S-factors.

Acknowledgments

Mom for everything.

Contents

List of Figures

List of Tables

Chapter 1

Nuclear astrophysics fundamentals

In order to apply nuclear astrophysics to the study of star element production, there are essentials to be considered. In this chapter, a general review of the main points relevant for nuclear physics are presented that emphasizes selected topics that are relevant in the field of nuclear astrophysics.

1.1 General aspects about the nucleus

Introduce a brief description of the nuclei. The structure of the nuclei

The nucleus is a bound state of a system of protons and neutrons. These substructures are bound states of a set of fundamental particles, which are called quarks.

A general treatment given in [1] and basic concepts in [2].

Nuclear concepts.

A more particular textbook on nuclear astrophysics [3].

Elementary nuclear structure - Atomic nuclei are bond states of nucleons - Two types of nucleons - Protons. Positively charged, stable. - Neutrons. No charged. Slightly heavier than protons and unstable by themselves. - Nuclear stability is explained by considering the interaction between - Long range repulsive Coulomb interaction - Short range strongly attractive nuclear interaction. - Mass difference and binding energy.

Binding energy is defined as:

$$B(A,Z) = Zm_pc^2 + (A-Z)m_nc^2 - E_0, \tag{1.1}$$

where Z, A are the atomic and mass number respectively. In addition, $E_0 = Mc^2$ with M being the mass of the nuclei. Then, $M \neq Zm_p + (N-Z)m_n$. The shape of the binding energy

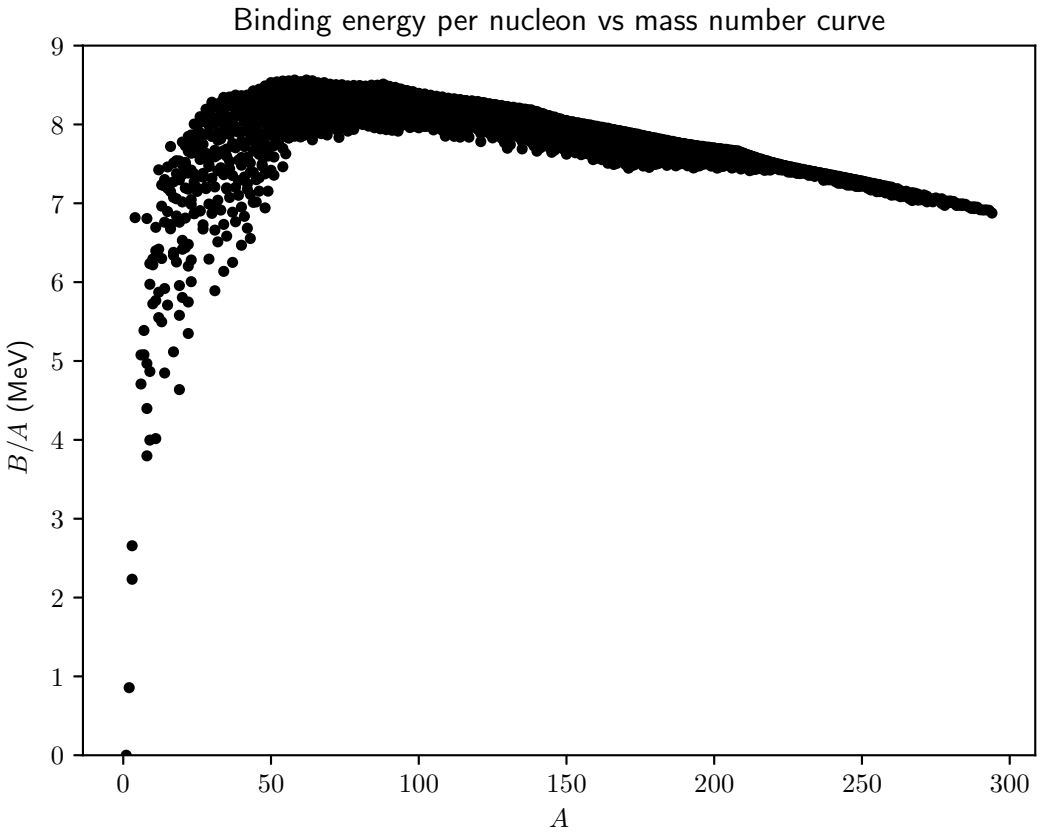

Figure 1.1: Binding energy per nucleon B/A characteristic curve . Each scatter point represents a nucleus. The plot has an overall ascending behavior until it reaches the stability peak, which is located roughly below 9MeV. Then, at higher energies, the behavior consists of a less sharper descent. B/A values were calculated from data given by the JENDL database [4].

They are particles Characteristics of nucleons - They obey the Pauli-exclusion principle like electrons - They have magnetic moment. - They are bonded in the nuclei by the strong force which compensates the repulsive electromagnetic force - Each nucleon is conformed by elementary particles.

Nuclear transmutation Decays - Alpha - Beta - Gamma Captures - Nucleon capture - Gamma capture

Quantum numbers - Electric charge - Orbital angular momentum and spin - Parity

Subatomic particles
Baryons - Mesons and hadrons - Quark model as subunits - Classifications and symmetries
Leptons Characteristics - They do not interact via strong force - Considerably lighter in mass than nucleons
Classification - Electron - Neutrino - Antiparticles are also considered

Writing strategies.
Kind of paragraphs to be used:
1. Miau meow 2. The other paragraph 3. Enthusiasm paragraph 4. Structuring
This is a short workshop on writing when the intention is to template and organize ideas.

Writing can be useful for doing the organizing exercise so it is just natural to use it directly when approaching the actual text to be intervened.
As it is natural, a hierarchy is given in the organization of ideas. However, paragraph gluing might not follow the same standards as idea production, or it can be similar in some circumstances.
I like to classify the kind of paragraphs to be encountered in this text:
Theory Experiment Computation
This is a first element of classification. All of these have their own particularities
Introduce a definition Motivate a concept Deduce results Graph analysis Argue findings
Lets take the example of the nucleus
Information about the nucleus will be found.
This is a shortcoming for further investigation. Lets mine it further
General information about the nucleus. What is a nucleus? ... some response lets see models
A 1 is a 2 with 3. 1 has some classes like those introduced in 4.
the verb is has synonyms
A is defined A is composite of A ....
More connections with paragraphs
Now, how to implement with the workflow of theory . An idea is to begin numerating but having in mind the starting and ending point.
Arguably, the finding of the extremes is an exercise of interesting thinking. Then, they are criteria that help you to naturally cover the rest of the blackbone.
Concepts wrap topics. The sequence of topics with their respective connections play roles. It uses different parts.
Nucleus: Starting point: ... Bounded state of protons and neutrons.
Stability - Stability can be quantified using the binding energy curve. - Decay is a consequence of the nuclei to find the most stable configuration
Quantum mechanics
Conservation laws - Quantum numbers - Certain processes conserve some numbers when interaction take place.
Interactions - Nuclear - Electromagnetical interaction - Weak force for decays
Ending point:
Nuclear reactions Nuclear structure
Bounding is guaranteed, which is essential to actually attempting to finish a large project.

1.2 Elements of quantum mechanics for nuclear physics

Quantum mechanics governs the physics at the nuclear scale. In particular, some elements of quantum mechanics theory that are essential for the description of nuclear reactions. For instance, quantum mechanical treatment of scattering theory is critical for determining the behavior of the rates of the reaction. In addition, tunneling phenomena, which can only be explained from the non-classical behavior of nuclear physics, permits the existence of nuclear fusion. Finally, transition phenomena will be considered in this section from the point of view of electromagnetic transitions.
Quantum mechanics text [5].

1.2.1 Scattering theory

Explain scattering theory relevant for the understanding of processes.

The sequence of the calculations on scattering is the following - Consider free path approximation -> Bessel Function solution - Expand free wave in terms of Bessel and Harmonic oscillator solutions - Obtain the coefficients of the expansion - Evaluate asymptotic behavior at $r \to \infty$

When considering a potential, it appears that the oscillatory asymptotic wave function is shifted $e^{2i\delta_l}$. This factor depends on the angular momentum l. This directly relates with differential cross sections.

A reference text on collision theory [6].

$$\sigma = \frac{\text{scattered per time}}{(\text{incident per time per area})(\text{total nuclei})}. \tag{1.2}$$

Cross sections are probabilities The probabilities are ruled by the laws of scattering theory, which can be understood as a subpart of quantum mechanics.
There is of interest the differential cross section. Particularly, there is a connection with quantum mechanics scattering amplitudes with the formula
Cross section -> Reciprocal factors -> Scattering potentials -> Coloumb Barrier (With WKB approximation) -> Breit - Weigner formula (This is for resonant behavior)-> S factors, ...

$$i\hbar\frac{\partial}{\partial t}\Psi(\vec{r},t) = \hat{H}\Psi(\vec{r},t). \tag{1.3}$$

$$-\frac{\hbar^2}{2m}\nabla^2\psi(\vec{r}) + V\psi(\vec{r}) = E\psi(\vec{r}). \tag{1.4}$$

$$\psi(\vec{r}) = u(r)Y(\theta,\phi). \tag{1.5}$$

$$Y(\theta,\phi) = \Theta(\theta)\Phi(\phi). \tag{1.6}$$

$$-\frac{\hbar^2}{2\mu}u''(r) + u(r)\left(V(r) - \frac{\hbar^2 l(l+1)}{2\mu r^2}\right) = Eu(r). \tag{1.7}$$

There are several contributions to the total rate. There are four in principal Broad resonances, thin resonances, continuum, nonresonant.
Scattering theory develops from the method of partial waves. It roughly consists on solving for the Schödinger equation in free space and, with the potential given, expand in terms of an orthonormal basis of functions, like spherical Bessel and Neumann functions and spherical harmonics. Then, conditions are adjusted via boundary condition satisfying.

Partial wave expansion

Initially, incident particles are modeled as plane waves since they are sufficiently far from the region of action of the interaction potential. Therefore, the ingoing wavefunction is exemplified by:

$$\psi_-(\vec{r}) \to Ae^{ikz}, \tag{1.8}$$

where A, k, z correspond to the amplitude, wave-number and displacement of the wave respectively. The selection of the $+z$ axis as the preferred axis obeys literature conventions.

Subsequently, when the particle gets scattered, the outgoing wavefunction $\psi_+(\vec{r})$ accounts for the changes of the state of the system after the scattering process. In the case of $r \to \infty$, the wavefunction approaches to:

$$\psi_+(\vec{r}) \to \frac{f(\theta,\phi)}{r}e^{ikr}, \tag{1.9}$$

where $f(\theta,\phi)$ corresponds to the scattering amplitude, which is proportional to the amplitude of the radial-wave contribution of equation 1.9. This term has physical relevance since it is closely connected to the details

of the interaction that causes the scattering. In particular, it has a connection with the differential cross section $d\sigma/d\Omega$, which is expressed as:

$$\frac{d\sigma}{d\Omega} = |f(\theta, \phi)|^2 \tag{1.10}$$

With this picture given, the entire wave function $\psi(\vec{r})$ is approximated as the sum of the ingoing and outgoing contributions of equations 1.8 and 1.9 as expressed in:

$$\psi(\vec{r}) = \psi_-(\vec{r}) + \psi_+(\vec{r}). \tag{1.11}$$

it is sufficient to determine the constant A and the differential cross section to fully describe the scattered system. On the one hand, the constant A can be determined by normalization. On the other hand, the differential cross section, or its related quantities like the cross section, are determined by a wide variety of methods, which are expanded in Chapter 3. On the other hand, constant A can be determined by matching appropriate boundary conditions.

As a first step towards the constant determination is the expansion of the incident term in equation 1.8 in terms of a linear combination of a convenient basis that actually solves the Schrödinger equation. For the case of $V = 0$, which happens at $r \to \infty$, the angular contribution of the wave function can be expressed in terms of spherical harmonics $Y_m^l(\theta, \phi)$ and the radial contribution in terms of Bessel functions $j_l(kr)$ as given by:

$$\psi(r, \theta, \phi) = \sum_l \sum_m c_{lm} Y_m^l(\theta, \phi) j_l(kr) \tag{1.12}$$

Then, the plane wave contribution to equation 1.9

$$e^{ikz} = 4\pi \sum_{l=0}^{\infty} \sum_{m=-l}^{m=l} i^l Y_m^l(\theta, \phi) j_l(kr). \tag{1.13}$$

Free space solution with $j_l(kr)$ the spherical Bessel function of l parameter. There are also the $n_l(kr)$ Neumann function and the Hankel functions $h^{(1)}(kr)$ and $h^{(2)}(kr)$ functions.
A result that relates cross sections and the probability current density is the theorem.

$$\sigma = \frac{4\pi}{k} \mathrm{Im}(f(\theta = 0))) \tag{1.14}$$

$$S_l = 1 - e^{2i\delta_l}. \tag{1.15}$$

$$\sigma \propto \sum_l (2l + 1)|S_l|^2. \tag{1.16}$$

Born approximation

$$(\nabla^2 - k^2)\psi(\vec{r}) = 0. \tag{1.17}$$

Born approximation that is used for estimating the scattering amplitude.

$$f(\theta) = -\frac{2m}{\hbar^2} \int_0^{\infty} \mathcal{F}\{V(r)\} dk. \tag{1.18}$$

Wavefunction ansatz with spin:

$$\psi(r, \theta, \phi, \xi) = \frac{u(r)}{r} Y_l^m(\theta, \phi) \otimes \chi(\xi). \tag{1.19}$$

1.2.2 Tunneling phenomena

Quantum tunneling phenomena is critical in understanding the phenomena of alpha particles decaying in the nuclei barriers.
WKB approximation for the classical forbidden regions.

$$T = e^{2i\delta_l}. \tag{1.20}$$

Ansatz:

$$\Psi(r) = \Psi_0 \exp\left(\Phi(r)\right). \tag{1.21}$$

The Schrödinger equation transforms as

$$\left(\Phi'' + \Phi'^2\right)\Phi = \left(\frac{2m}{\hbar^2}(U(r) - E)\right)\Phi. \tag{1.22}$$

Then, if it is considered that $\Phi'' \ll \Phi'^2$, then Φ can be directly integrated and is expressed as:

$$\Phi(E) \approx -\frac{1}{\hbar}\int_{r_1}^{r_2} \sqrt{2m(U(r) - E)}dr, \tag{1.23}$$

where r_1 and r_2 correspond to the lower and higher classical turning points respectively. In this opportunity, the negative choice for the square root was taken in order to account for the fact that the probability of transmission decreases within the non-classical region.
More information in [7].

1.2.3 Perturbation theory

Despite the existence of exact solutions on various systems in quantum mechanics, it is more frequent to find that the solution of an arbitrary system is not expressible in a closed form. Particularly, given that an exact form for the nuclear force is almost unknown, finding exactly solvable systems in nuclear physics is an nonviable task.

Perturbation theory presents a handy framework for simplifying the computations when multiple interaction are present in the Hamiltonian, which can be expressed as:

$$H = H_0 + \lambda\delta H, \tag{1.24}$$

where H_0 and δH are the known and unknown Hamiltonians respectively. In addition, there is a parameter λ, with $0 \leq \lambda \leq 1$, which is introduced to parametrize the perturbation.

Therefore, approximation methods provide the key for finding solutions in nuclear physics are required to a precision degree. For example,
are heavily restricted involve the n general rule due to the complexity of the nuclear interaction interactions that they involve. In order to overcome this, some approximation methods are introduced.
In particular, it is desirable that methods ca
hich are based on perturbation theory, which can be regarded as perturbative methods, express in order to find the solution of complex Hamiltonian with the basis of an initial known solutions.
General definition of the perturbed Hamiltonian.
Energy shifts and state shifts.
There are two main approaches:
Time-independent perturbation theory.

Time-dependent perturbation theory.

Perturbation theory is involved in the calculation of cross sections and reaction rates.
An application of perturbation theory is the Fermi Golden rule for transition decay rates.
Electromagnetic transitions are also modeled as perturbations. In this case, the perturbed Hamiltonian is proportional to an electromagnetic wave oscillating term as it is given by:

$$\delta H \propto \cos(\omega t). \tag{1.25}$$

Then, time-dependent perturbation theory calculations shall proceed by calculating the matrix elements associated with the perturbed contribution to the Hamiltonian. In particular, the transition goes from a bounded state ϕ_b to a continuum state ϕ_c.

Initially, the elements $\langle \phi_b | \delta H | \phi_c \rangle$ are calculated by integration. However, some terms of the transition matrix are anticipated to vanish due to the existence of symmetries in the potential. This convenient cancellation of some terms in the matrix imply that some transitions are forbidden. Then, the allowed transitions must obey certain rules which are related as transition rules.

Another noticeable application of perturbation theory in nuclear physics is in the calculation of the spin orbit coupling. It turns out that this perturbation is essential in nuclear structure determination, as well as in reactions involving effective potentials.

The perturbed Hamiltonian associated with this interaction contains a coupling term which relates the orbital $\vec{L}$ and spin $\vec{S}$ angular momentum operator with the form:

$$\delta H_{\mathrm{SO}} \propto r^{-3}(\vec{L} \cdot \vec{S}). \tag{1.26}$$

Cross section dependence on transition elements.

$$\sigma \propto |\langle k | \delta H | m \rangle|^2 \tag{1.27}$$

Splitting illustration in Figure 1.2.

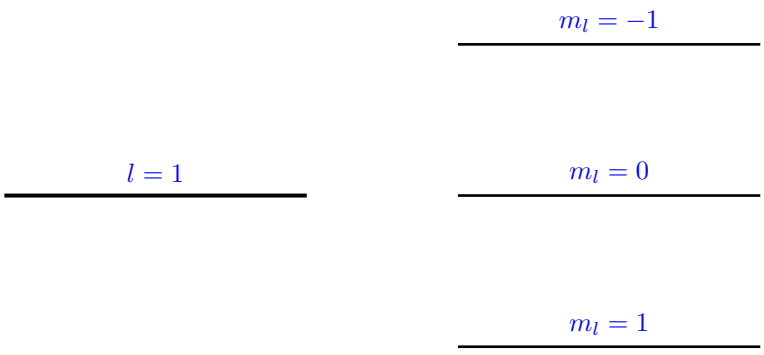

Figure 1.2: Illustration of level splitting due to orbit effect (under elaboration)

The changes of state that nuclei exhibit obey certain rules. In particular, this selection rules consider angular momentum conservation. An illustration is given in Figure 1.3.

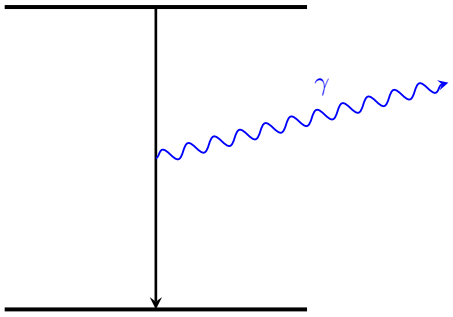

Figure 1.3: Depiction of an electromagnetic radiative transition (under elaboration)

Selection rules. Electromagnetic interaction and resonances E1 and M1 gigantic resonances (finite amplitude method - Hartree-Fock - mean field like - random phase approximation + double magic nuclei) [8].

1.2.4 Angular momentum

Angular momentum is an relevant conserved quantity in physics, in particular in nuclear reactions.

$$J = L + S. \tag{1.28}$$

.

$$[J_a, J_b] = i\epsilon_{abc} J_c. \tag{1.29}$$

.

$$|JM\rangle = \sum_{J=j_1-j_2}^{j_1+j_2} \sum_{M=-J}^{J} \langle j_1 j_2 m_1 m_2 | JM\rangle |j_1 j_2 m_1 m_2\rangle. \tag{1.30}$$

.

1.3 Nuclear structure

Nuclear structure is presented in this section.

1.3.1 Nuclear models

Stability depends closely on the biding energy. In particular, since the rest energy of the nucleus decreases with $B(A, Z)$, the more is the binding energy, the more stable is nucleus.

Liquid drop model

A first approach when modeling the binding energy is a phenomenological model which is inspired in the physical description of a liquid drop. In particular, the predictions of the binding energies are determined by the fitting of the empirical formula:

$$B(Z, A) = a_1 A - a_2 A^{2/3} - a_3 \frac{Z(Z+1)}{A^{1/3}} + a_4 \frac{(A-2Z)^2}{A} + a_5 A^{-1/2}\delta. \tag{1.31}$$

However, this model does not fit accurately the binding energy of a selected nuclei which are more stable than expected from the model. In particular, it is said that the pair of number of protons and nucleons (Z, A) of these nuclei are magic numbers.

- The more stable the nuclei, the greater the binding energy. Binding energy is the energy difference of rest energy of the nucleus constituents and the actual rest mass of the overall nucleus.

$$\delta = \begin{cases} 1, & Z \text{ and } A \text{ even} \\ -1, & Z \text{ and } A \text{ odd} \\ 0, & \text{otherwise} \end{cases} \tag{1.32}$$

Nuclear shell model

An alternative approach to the Liquid drop model is a model based on quantum mechanics. This model is closely related with the quantum mechanical modeling of the hydrogen atom. In particular, a great part of the nuclear shell model consists of solving Schrodinger equation which is expressed as:

$$-\frac{\hbar^2}{2m}\partial_{tt}\psi + V\psi = E\psi. \tag{1.33}$$

In this case, the potential V represents the effective potential of the core of the nucleus and is valid at certain radii. For example, the harmonic potential $V = m\omega^2 r^2$ models effectively the system of nucleons at most regimes.

Spin orbit coupling rules the energy levels of the nucleons. Levels are planned to be illustrated in Figure 1.4.

- Nuclear shell model is based on quantum mechanics.
-Nuclear shell model can predict the existence of the magic numbers.

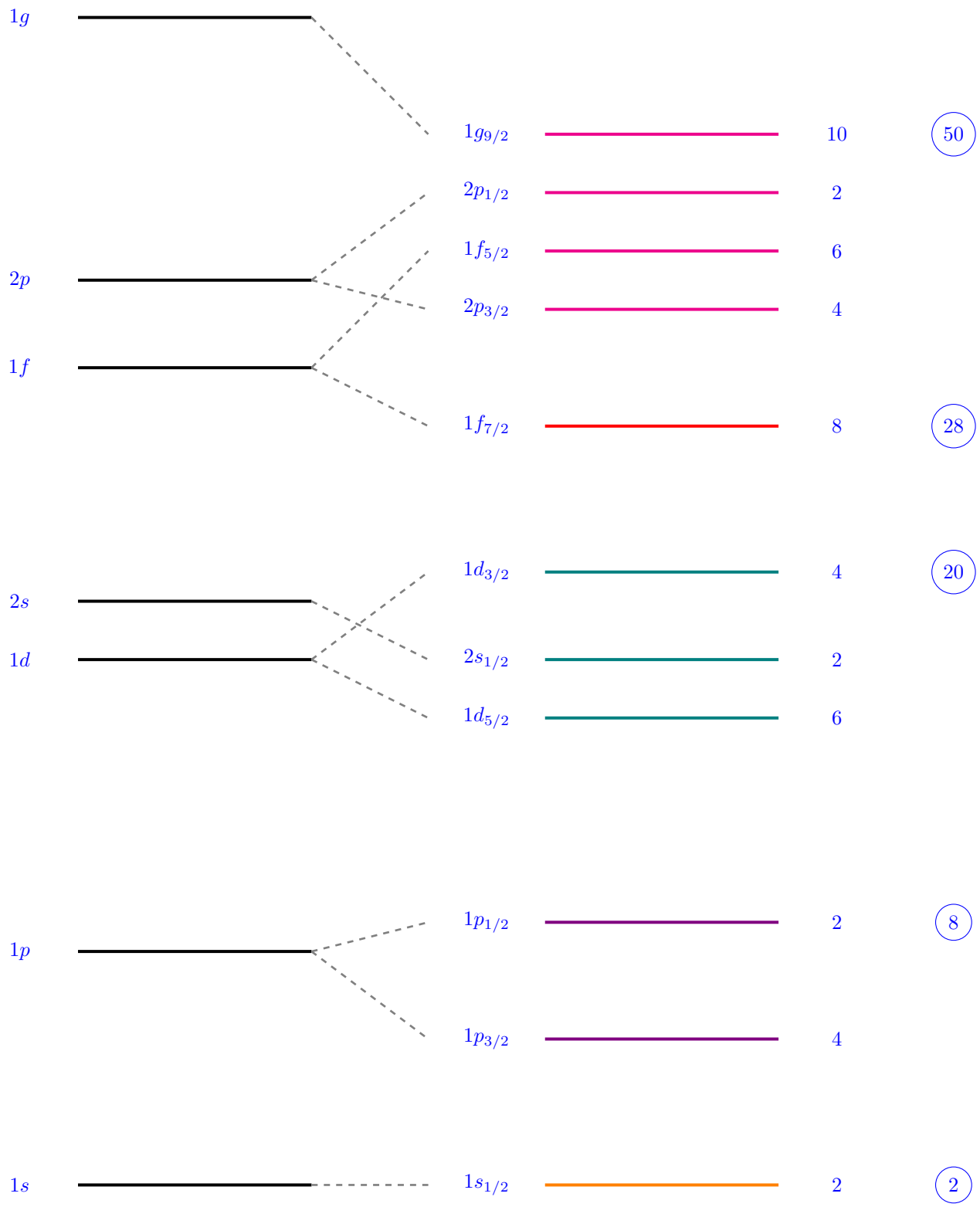

Figure 1.4: Levels picture for the nuclear shell model with the first five magic numbers included. This chart was inspired by Figure 1 of reference [9].

1.3.2 Nuclear levels and transitions

Nuclear levels work in a similar way than atomic levels. Additionally, the are possibilities of transitions between levels.

1.4 Nuclear reactions

Nuclear reactions are surveyed in [10].

A planned chart is found in Figure 1.5.

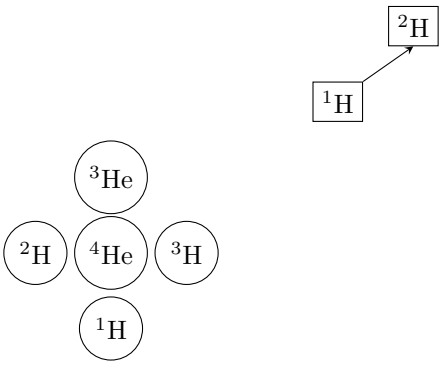

Figure 1.5: Nuclear reactions chart (under elaboration)

1.4.1 Classification of reactions

The relevant reactions for the document are:

$$0 + 1 \to 2 + 3 \tag{1.34}$$

$$\gamma + 3 \to 0 + 1 \tag{1.35}$$

Expand on how the fusion reactions occurs, their conditions and types as well as the differentiation factors with respect to fission processes.

Capture reactions

Also, radiative capture processes are considered at astrophysical energies. Various models could be used for determining potentials. There are clusters and potential models.

$$X + c \to \gamma + X'. \tag{1.36}$$

When c is a proton, the reaction is called radiative proton capture [11]. In addition, under certain circumstances, c can also be an alpha particle.
This kind of reactions are usually slower than exchange reactions. Therefore, radiative capture reactions constrain the entire rate of the chain they belong to. For example, in the CNO cycle, the reaction rate of the cycle is given by the rate of the $^{13}\mathrm{C}(\mathrm{p},\gamma)^{14}\mathrm{N}$ reaction.

Radiative capture appears in various element production contexts like pp chain, CNO cycle and also in explosive environments like X-ray burst and supernovae. There is a particular importance of the reaction $^{7}\mathrm{Be}(\mathrm{p},\gamma)^{8}\mathrm{B}$ since its product is a part of the triple alpha chain, which eventually results in the production of $^{12}\mathrm{C}$. In turn, the last nucleus is of crucial importance to the production of heavier elements.

Exchange reactions

Another common reaction happens when there are two reactants and two products. This process is expressed by:

$$X + x_1 \rightarrow x_2 + X'. \tag{1.37}$$

A case of special interest occurs when X and X' are considerable heavier than x_1 and x_2 nuclei. Then, this process can be regarded as if the x_1 and x_2 nuclei where exchanged, while the heavier nucleus X transforms to X'.

This reaction proceeds depending which is the heaviest nuclei. In particular, there are two main mechanisms: stripping and pickup [12].

Stripping follows when X' is heavier than X, and therefore x_1 is heavier than x_2. The form of this process is given by:

$$\begin{aligned} x_1 &\rightarrow x + x_2 \\ X + x &\rightarrow X'. \end{aligned} \tag{1.38}$$

On the other hand, pickup occurs when X is heavier than X', and thus x_2 is heavier than x_1. This channel proceeds like:

$$\begin{aligned} X &\rightarrow x + X' \\ x_1 + x &\rightarrow x_2. \end{aligned} \tag{1.39}$$

It is essential to be noticed that both reactions follow a two step process. The first step consists of a decay reaction with the particularity that it produces the nucleus x, which serves as a reactant in the following merging reaction. Ultimately, since x appears in both sides on the two possible processes, it is not distinguished neither as a product nor as a reactant in the simplified form of the exchange reaction of equation 1.37.

A development on the (p, n) reaction kind is given by (Distorted wave Born approximation DWBA model) [13] and for the (n, p) in (Weisskpf-Ewing) deformation without spin description [14].

$^2\mathrm{H}(\mathrm{d}, \mathrm{p})^3\mathrm{H}$ is an example of an exchange reaction relevant for BBN and pp-chain nucleosynthesis.

Fusion reactions

$$X + X \rightarrow a + X'. \tag{1.40}$$

1.4.2 Cross sections

Cross section of a process. Partial and total cross sections depending on the reaction type. Cross sections have relations with the S-matrix.

1.4.3 Reaction rates

The ratio that determines the quantity of a nucleus.

$$r = N\langle\sigma(v)\rangle v. \tag{1.41}$$

$$r = A\int_0^\infty E\sigma(E)\exp\left(-\frac{E}{kT}\right)dE. \tag{1.42}$$

$$P(v)dv \propto v^2 \exp\left(\frac{mv^2}{2kT}\right)dv. \tag{1.43}$$

On specifying the rates, it is needed to be considered.
Reaction rates are considered from calculation of transmitted, incident and interacting - Reaction rate depends on the density of particles, the velocity and the cross section - It is averaged by a convenient distribution. (Maxwell-Boltzman for fermions, Bose Einstein (Planck) for photons) - With the rates, abundance evolution is determined
For particles of matter, the statistics at the star fusing scale is Maxwell - Boltzmann and for photons the Bose - Einstein statistics.

There are broad classification of reactions.

1.5 The Astrophysical S-factor

Cross section does not count for the low-energy behavior. Then, additional factors can be obtained. For example, S-factor.

1.5.1 Definition

There are S factors associated with the energy and they are the path to determine the nature of the potential, which is not necessarily a Yukawa potential.

$$S(E) = E\exp(2\pi\eta)\sigma(E). \tag{1.44}$$

It is directly proportional to the microscopic cross section of the process $\sigma(E)$ and it represents the rate of a certain nuclear reaction.
In particular, the astrophysical S-factor scales the cross section with a factor proportional to the Coloumb repulsion.
The ν factor is defined as

$$\eta = \frac{Z_1 Z_2 e^2}{4\pi\epsilon_0 \hbar v} \tag{1.45}$$

where v corresponds to the relative speed between the reactants. At the same time, this speed can be expressed in terms of E as given by:

$$v = \sqrt{\frac{2E}{\mu}}, \tag{1.46}$$

where μ corresponds to the reduced mass of the reactant nuclei.
There is a strong relation of the astrophysical S factor with the center of mass energy.
Usually this relation depends on the square of the energy of the center of mass E_{cm}.

There are topics that are relevant in the frontiers of nuclear astrophysics [15] (classification with all the nuclear astrophysics environments).

1.5.2 General applications

Cross section extrapolation to low energies
Reaction rates and element abundance estimations.

Chapter 2

Reactions of astrophysical interest

Nuclear reactions are part of the core of nuclear astrophysics. They are accountable for the production mechanism of elements in several astrophysical environments where thermonuclear reactions can occur. In particular, there are specially relevant reactions for the explanation of the abundance of elements. For example, some of these reactions are part of critical fusion chains of stars, have challenging extrapolation techniques to low energies, or exhibit exotic underling physical phenomena.

In this section, a relevant selection of reactions types of will be reviewed. Several reaction kinds and models are given and the classification of potential, R-matrix and microscopical models are illustrated in [16].

2.1 Big Bang nucleosynthesis

Primordial reactions that where expected to happen just after the Big Bang occurred. For example:
Seconds to minutes after the Big Bang.
Neutron and proton stability difference. Neutrons are unstable. Shift towards protons permits fusion.
Two conditions: the feasibility to fuse and the disintegration stability.
Balance between photons and baryons. If photons density exceeds too much the number of baryons, disintegration dominates.
Deuterium is the first nuclear fusion product, since it consists of a proton and a neutron. began to fuse when photons had energy lower than the binding energy of deuterium nuclei.
Relaxation times and deuterium fusion possibility. Eventually, Universe cooling inhibited additional fusion.

$$^{2}\mathrm{H} + \mathrm{p} \rightarrow \gamma + {}^{3}\mathrm{H}. \tag{2.1}$$

BBN description [17] Review [18].
Elements very high temperatures [19]
Even CNO elements can be produced via BBN nucleosynthesis under specific conditions [20].
Unlike other abundances of lighter elements, lithium abundance is not well explained by Standard Big Bang theory [21].

2.2 Stellar fusion

Much after the Big Bang, stars are formed. The high temperature and density enviornment of the core of stars allows the activation of various fusion reactions.
Stellar stability is the result of the hydrostatic equilibrium established by the compensation compressing gravitational effect with the repulsive radiation pressure exerted fueled by the fusion reaction produced at the core of the star. The mechanisms of heat exchange in stars are radiation and convection.

Stars evolve in a process called stellar evolution.
The diversity of elements fusing at the core of a star heavily depends on the kind of star and the stage in the stellar evolution. Initially, when temperature and density have reached critical values, the fusion process begins. In particular, hydrogen is the first element source of fusion reactions.
The classical treatment of fusion in stars is given by the classical [22].
Summary text with aspects of stellar evolution, degenerate stars and more [23].
Hertzsprung-Russel diagram permits a classification of a star with respect to specific categories which are related to different evolution stages in the lifetime of a star [24].
Introduce the needed conditions for the creation of stars in the primordial nebula. Describe how the hydrogen is burnt in the star's core and the associated products.
Explain the required conditions that permits nuclear fusion in the star's nucleus.

2.2.1 Light heavy nuclei reactions

pp chain

Much of the initial fusion at the core of a great extent of lifetimes of main branch stars like the sun consist on hydrogen fusion reactions.The interactions of pp-chain processes are mostly electromagnetic and strong force with additional weak force mediated reactions. In addition, reaction rates of nuclear fusion processes depend on the interaction cross section and the abundance of the reactant nuclei.
pp chain review [25].
The main reaction in which this process occurs is:

$$p + p \rightarrow d + e^{+} + \nu_e. \tag{2.2}$$

Then, when deuterium is available, there is the possibility of production of tritium t, which is a name for the ^{4}He nucleus, in a reaction of the form:

$$d + d \rightarrow n + {}^3\mathrm{He}. \tag{2.3}$$

Alternatively, another tritium producing fusion reaction involving deuterium fusion is given by:

$$d + d \rightarrow p + t. \tag{2.4}$$

Tritium production opens different branches for the pp-chain. For example, the main branch proceeds like:

$${}^3\mathrm{He} + {}^3\mathrm{He} \rightarrow {}^4\mathrm{He} + 2p. \tag{2.5}$$

This process in known as the pp1 chain. On the other hand, a more unlike second branch named pp-II follows as :

$${}^3\mathrm{He} + p \rightarrow {}^4\mathrm{Li} + \gamma \rightarrow {}^4\mathrm{He} + e^{+} + \nu_e + \gamma. \tag{2.6}$$

This process is unlikely because of the instability of ^{4}Li, which decays to ^{3}He.
Lastly, an additional third branch is yet possible called pp-III given by:
As it is seen in the previous reactions, this chain ends with the production of ^{4}He. The chain stops here because this is the most stable nucleus of the light nuclei class. Additionally, this resulting nucleus is a relevant source of the production of heavier nuclei, in particular of the triple alpha process reactions.
Additionally, screening effect present in light weight nuclear reactions [26] and a review of screening effect [27].

Triple alpha process

When ^{4}He abundance, as well as temperature and density conditions are sufficient enough to fuse helium, the triple alpha process takes place. This conditions are not necessarily reached in all stars. In fact, the sun reaches this process at the last period of its lifetime.
Triple - alpha process review [28].
The process is called triple alpha because it consist of three reactions involving α particles, which are equivalent to ^{4}He nuclei.

$$^4\text{He} + {}^4\text{He} \rightarrow \gamma + {}^8\text{B} \tag{2.7}$$

The next instance:

$$^8\text{B} + {}^4\text{He} \rightarrow \gamma + {}^{12}\text{C}. \tag{2.8}$$

Finally,

$$^{12}\text{C} + {}^4\text{He} \rightarrow \gamma + {}^{16}\text{O}. \tag{2.9}$$

The resulting nuclei of this process is ^{16}O, which is a very stable nuclei since it is double magic. This reaction completes with the production of another stable nuclei like ^{12}C. These two nuclei will have a substantial role in the production of heavier elements at the last stages of giant stars.

2.2.2 CNO cycle

When the star has capacity of completing the triple alpha process, their subproducts are available for additional nuclear reactions. In particular, with the presence of ^{12}C nuclei, a series of capture reactions take place. These reactions will form cycles.
CNO cycle reactions [29].
The first cycle reactants include carbon, nitrogen and oxygen isotopes. The reaction proceeds as:

$$^{12}_{6}\text{C} \rightarrow {}^{13}_{7}\text{N} \rightarrow {}^{13}_{6}\text{C} \rightarrow {}^{14}_{7}\text{N} \rightarrow {}^{15}_{8}\text{O} \rightarrow {}^{15}_{7}\text{N} \rightarrow {}^{12}_{6}\text{C}. \tag{2.10}$$

The last cycle fuels another nuclear capture cycle. In this case, the starting point are ^{15}N nuclei and the cycle also involve oxygen and fluorine isotopes. In particular, the cycle is given explicitly by the reaction chain:

$$^{15}_{7}\text{N} \rightarrow {}^{16}_{8}\text{O} \rightarrow {}^{17}_{9}\text{F} \rightarrow {}^{17}_{8}\text{O} \rightarrow {}^{14}_{7}\text{N} \rightarrow {}^{15}_{8}\text{O} \rightarrow {}^{15}_{7}\text{N}. \tag{2.11}$$

There is even a third CNO cycle, which is far more uncommon and there fore is considerably ess dominant than the second and first CNO cycle. In this case, the process is given by:

$$^{17}_{8}\text{O} \rightarrow {}^{18}_{9}\text{F} \rightarrow {}^{19}_{10}\text{Ne} \rightarrow {}^{19}_{9}\text{F} \rightarrow {}^{16}_{8}\text{O} \rightarrow {}^{17}_{9}\text{F} \rightarrow {}^{15}_{8}\text{O}. \tag{2.12}$$

The last three processes are summarized in the illustration of Figure 2.1.

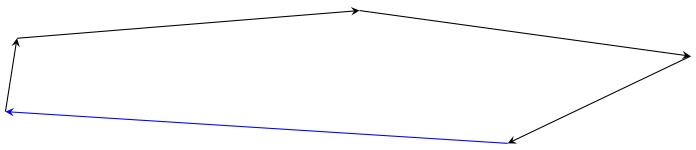

Figure 2.1: CNO I, II and III cycles representations. Notice how the byproducts of the preceding cycles are sources of the next cycle. This figure is under elaboration.

Notice that the cycle balance is established by the existence of proton capture and beta decay, which increases and decreases the atomic mass respectively. Then, any change in the rates of the previous reactions would alter the possiblity of production of certain elements. In particular, at high enough temperatures, the rate of the proton capture process surpass that of the beta capture. Then, alternative products are produced and new processes form what is called hot CNO cycles.

Further cycles related to alpha reactions Ne cycle [30]

There are more cycles of capture reaction. An example regarding the MgAl cycle is given in [31].

2.2.3 Medium heavy fusion reactions

At a certain moment, the core of big stars starts to contract. Then, various middle heavy elements start to be consumed by the star. These reactions concern nuclei with $A < 28$. Classical burning processes include carbon, neon, oxygen and silicon, as well as a whole new variety of processes are allowed given the appropriate conditions at the last period of the lifetime of the star.

Examples of this kind of reaction include the $^{12}\mathrm{C} + {}^{12}\mathrm{C}$, and the $^{16}\mathrm{O} + {}^{16}\mathrm{O}$ fusion reactions. Most of these reactions result in different channels.

With respect to the carbon fusion reaction, which is the starting reaction, the principal channel is given by:

$$^{12}\mathrm{C} + {}^{12}\mathrm{C} \rightarrow {}^{4}\mathrm{He} + {}^{20}\mathrm{Ne}. \tag{2.13}$$

Additionally, carbon burning contributes to heavy nuclei production as being a source neutrons. In particular, the process that allows this production is given by:

$$^{12}\mathrm{C} + {}^{12}\mathrm{C} \rightarrow \mathrm{n} + {}^{23}\mathrm{Mg}. \tag{2.14}$$

Later, oxygen burning starts are very high temperatures and pressures than the neon and carbon burning due to the high stability of oxygen nuclei. In fact, oxygen nucleus is double magic.The main channel of the oxygen fusion reaction occurs in the following manner:

$$^{16}\mathrm{O} + {}^{16}\mathrm{O} \rightarrow {}^{4}\mathrm{He} + {}^{28}\mathrm{Si}. \tag{2.15}$$

The neutron producing channel related to oxygen burning, which is analogous to the reaction of Equation 2.14, proceeds as:

$$^{16}\mathrm{O} + {}^{16}\mathrm{O} \rightarrow \mathrm{n} + {}^{31}\mathrm{S}. \tag{2.16}$$

Actually, there are more carbon and oxygen fusion channels than the previously mentioned. Further channels are visualized in the reaction bifurcations which are presented in Figure 2.2.

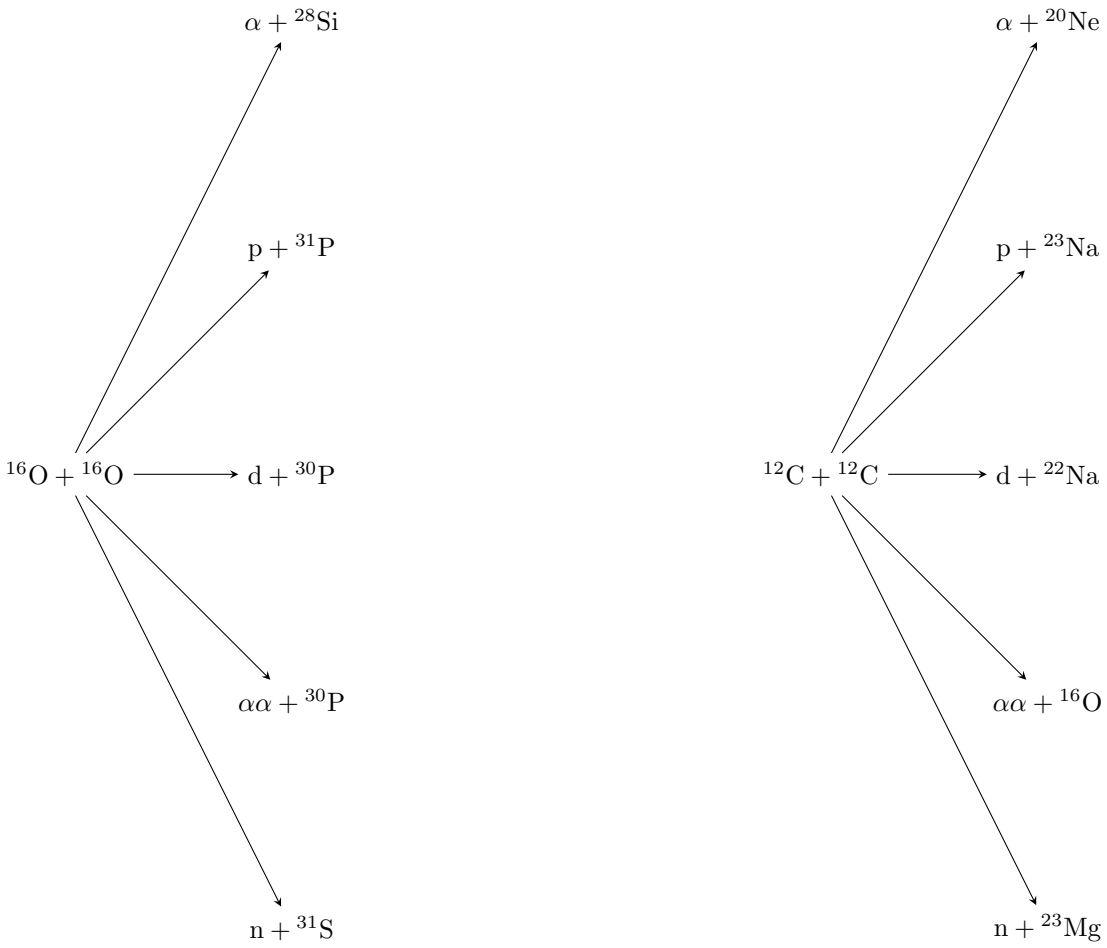

Figure 2.2: Reaction chart of carbon and oxygen burning main channels.

Additionally, there are reactions with the both carbon and oxygen as reactants. The ${}^{12}\mathrm{C} + {}^{16}\mathrm{O}$ is an example of this kind of processes.
Reactions are not limited to ground state reactants. In fact, there are inelastic channels associated with ${}^{16}\mathrm{O}$ which could increase the probability of occurrence for the overall reactions.

Additionally, neon burning stats by fusing with ${}^{4}\mathrm{He}$ nuclei to produce heavier elements.
Neon burning [32].
Fusion up to oxygen [33].
There is a silicon burning process with the following description

$$ {}^{28}_{14}\mathrm{Si} + {}^{4}_{2}\mathrm{He} \rightarrow {}^{32}_{16}\mathrm{S}. \tag{2.17} $$

Silicon burning is another process that closes the middle heavy burning. Silicon burning [34]. An example of a channel of the fusion reaction is given by:

$$ {}^{28}\mathrm{Si} + {}^{28}\mathrm{Si} \rightarrow {}^{4}\mathrm{He} + {}^{56}\mathrm{Fe}. \tag{2.18} $$

The burning processes does not continue further since ${}^{56}\mathrm{Fe}$ is one of the most stable of the whole list of nuclei. Then, as it is explained in the next section, alternative fusion process would need to occur to increment the mass of the resulting nuclei.

$^{12}C + ^{12}C$ nucleosynthesis in massive stars [35]. $^{12}C + ^{12}C$ is a source of α, n and p nuclei that are sources of further process, namely alpha capture, r-process and s-process respectively. This reaction plays important roles on other processes and depends heavily on temperature.
12C + 12C Wave packet dynamics (with two core shell model) [36]
nonresonant Bayersian (modified S-factor S^* + Woods-Saxon potential + statistical Hauser-Feshbach formula for nuclei evaporation decay)[37]
Modified Sfactor (Woods-Saxon + Bayesian analysis + Metopolis-Hastings algorithm) [38]
Trojan horse (with renormalization of S-factors) [39] (with DWBA and R-matrix mentions) [40]
full-microscopical (density functional + antisymmetrized molecular dynamics + reduced width amplitude) [41]
multichannel folding (3α microscopical calculated densities + optical + Woods-Saxon potential + coupled channels R-matrix) [42]
screening effects (WKB approximation + coupled channel formalism + Double folding cluster + exp2 + selected density distributions + cosine damped screening potential [stronger screening effect]) [43]
correlation between carbon fusion reactions ($^{12}C + ^{12}C$, $^{12}C + ^{13}C$ and $^{13}C + ^{13}C$, coupled channel calculations, ingoing wave boundary condition with various potentials [Akyüz-Winther and M3Y with repulsive core], energy peak values $^{12}C + ^{12}C$ resonances) [44] constraint 12C + 12C based on 12C + 13C reaction (potentials coupled channels M3Y with repulsive core + time dependent Hartree Fock + São Paulo folded KNS potential +wave packet dynamics) [45]
16O + 16O cross sections on models (SPP like barrier penetration model vs coupled channel model + [Zero point motion] inelastic couplings to vibrational bands + molecular effects with Woods-Saxon two core shell model + reduced and cranking masses) [46] on channels and fusion cross section [47] α, n, p and $2p$, 2α, αp, αn.
oxygen isotopes fusion $^{16}O + ^{16}O$, $^{16}O + ^{17}O$, $^{16}O + ^{18}O$ with elastic and inelastic data [48] coupled channels potential model calculation (barrier penetration model + incoming wave boundary condition) [49].
12C + 16O semi-microscopic algebraic cluster + algebraic spectroscopic factor + coupled reaction channel (scattering reaction) + (Optical potential) SPP potential real part + Woods-Saxon imaginary potential + coupling schemes [50] low-energy resonances (Potential model + two Woods-Saxon models + deformation) [51]
Gross structures 12C + 16O based on yields of 12C + 16O and 12C + 18O [52]
Selected oxygen-oxygen and oxygen-carbon reactions with experimental data and model discussion + Liquid drop model parametrization + (exp11)-1 potential [53] Fusion evaporation $^{16-18}O + ^{16}O$ and $^{16,18}O + ^{12-13}C$ reactions + Hauser.Feshbach statistical model formalism to study α clustering + new level-density formula [54]
12C + 12C and 16O + 16O density dependent M3Y nucleon interaction 3α microscopical calculation + resonant group method (optical potential with real: coupled-channel [folded] with nuclear densities and imaginary: Woods-Saxon + R-matrix solving) [55]
12C and 24Mg resonances (microscopical cluster theory + 3 cluster system 1 core, 2 bodies - α clustering + resonant group method / generator coordinate method + no-microscopical hyperspherical formalism + resonant analysis models) [56]
Fusion hidrance (steep fall in fusion cross section + coupled-channels [CCFULL code] model interpretation + Woods-Saxon + vibrational coupling) 12C + 24Mg reaction [57]

2.3 Heavy nuclei reactions

Explain the different chains going on during the carbon-oxygen combustion to heavier elements like iron or silicon.
Additional fusion reactions with nuclei with $A > 28$ are present at the last stages of the life of a star. There are two main environments: The stellar fusion and explosive events fusion.
heavy-ion reactions + coupled channels + low-energy cross section enhancements + parameter free São Paulo potential + zero point motion (ZPM) + vibrational couplings + WKB approximation for undeformed

potential + nuclei deformation [58]

2.3.1 Supernovae and other explosive environments

This reaction is essential since the ^{56}Fe nucleus has the maximum binding energy. Then, fusion reactions of heavier nuclei tend to be less spontaneous.Then, this chain of reactions continues until the process in there 56-Ni is reached.

2.3.2 Alpha reactions

$$^{52}_{26}\mathrm{Fe} + ^{4}_{2}\mathrm{He} \rightarrow ^{56}_{28}\mathrm{Ni}. \tag{2.19}$$

Alpha and cluster decay [59].
Alpha induced reactions [60].

2.3.3 The s and r processes

There exists the s and the r processes. Each permits to form heavier nuclear elements products. Now, there are aspects of the particularities of the production of the nuclei that are currently unknown

On the other hand, protons are captured at the ending of the life of a gigantic star. This process, which occurs at high densities and temperatures, is referred as proton capture. In particular, under astrophysical scenarios like supernovas, the rapid proton capture, in addition to the neutron capture, produces a considerable amount of the heavy nuclei. This process is referred as rapid proton capture, or rp process.

Further processes are not viable because they are not exothermic and potential heavier nuclei than 56-Ni are photodisintegrated. At this scale of energy, nuclear reactions start to behave similarly than chemical equilibrium reactions.
The conditions are associated with the mass. Particularly, depending on the mass regime, star evolution can differentiate. For instance, there are brown dwarfs, sun like stars.

There is an evolution process that is ruled by different instances. Each instance can be regarded as a region in the Hertzsprung-Russell diagram. This diagram consists of a two dimensional scatter plot of the intensity with respect to the spectral type of a star. Particularly, there are regions associated to the different instances of the life of a star: Main sequence (Hydrogen burning stars), red stars, neutron stars, supernova of kinds Ia Ib and other instances.

Electron degeneracy prevents the white dwarf to collapse and the neutron degeneracy pressure prevents the neutron star to collapse. These limits account for relativistic Fermi gas and neutron degeneracy with a model from general relativity.

Indicate that there exists different channels of production depending on the existence of neutron capture or fission products. Additionally, explain the needed conditions in order to those processes to occur.

If mass increases further, there is no place to any degeneracy compensation so the star would collapse to a black hole.
s-process known and unknown [61].
s-process nucleosynthesis [62].
r-process form O-Ne-Mg cores [63].
r-process and beta decay [64].
alpha-process and r-process [65].
r-process without excess neutrons [66].
Neutrino capture and r-process [67].

r-process production beyond ^{209}Bi [68].
Electron capture [69].

2.3.4 The p and rp processes

The p processes are proton capture process.

The rp processes are like the p processes going on in a faster rate.
Abundance p-process [70].
Proton drip-line middle-heavy nuclei [71].
Alpha - gamma heavy p-nuclei [72]
Proton and alpha capture p process [73] [74].
p-process nuclei [75]
End point rp processes [76].
Proton drip-line rp processes [77].

2.4 Active research topics

Enumerate the broad ranges of phenomena that are left to be explained.

Introduce current approaches of some of the unsolved questions on nuclear astrophysics, particularly on the last instances of fusion in the star's lifetime.

There are various types of supernovae. However, there are mechanisms that are not considered and yet not well explained.

Current experiments in detection of heavy nuclei are essential to determine the distribution of elements, specially in events like the fusion of neutron stars.

Heavy and superheavy nuclei production [78].
Review on active research topics and current challenges in nuclear astrophysics in general [79] and on low-energy nuclear physics [80] are given.

Chapter 3

Astrophysical S-factor models

There are several methods for estimating the astrophysical S-factor. Each method is more convenient depending on the nature of the reaction. For example, method accuracy can vary depending on the reaction type or the existence of resonant phenomena. Additionally, the methods are based on a specific approach when modeling the S-factors. In this section, the principal methods of estimating the astrophysical S-factors will be reviewed.

3.1 Microscopic models

Microscopic models are based on first principles and usually require assumptions about the nucleus and its structure.

$$H = \sum_k T_k + \sum_k V_k(r) + \sum_{k \neq j} V_{kj}(r). \tag{3.1}$$

Modern theories *ab initio* electroweak reactions (correlated spherical harmonics and variational Monte Carlo method) [81]

3.1.1 *Ab initio* models

These models start from first principles without prior empirical or phenomenological assumptions. On the other hand, clusters consider the system of interactant nuclei as a whole. In particular, there are models based on *ab initio* assumptions about a particular set of nuclei.

Ab initio: Fermionic Molecular dynamics (wave-packet dynamics) [82] Unified approach chiral effective field theory [83] Ab initio wave function no core shell model [84] No core shell model. Beta decay [85] Tensor force in microscopical cluster model [86]
The *ab initio* no core shell model [87].

3.1.2 Many body models

The nucleus can be modeled as a many body system. Naturally, the nucleons are the components of this bounded system. In addition, the interactions between the components of the nucleus are nuclear interactions of a certain shape and form.

These models take into account the different bodies that make up the nuclei.

Therefore, cross section determination is reduced to the analysis of a many body quantum mechanics problem with all the nuclear compounds.

Multi-body calculations. Non-local calculations.

Also, nuclei deformation can be considered in models. For example, there are models with no-core shell.

Three body [88]
No core shell model [89]
Hauser-Feshbach (Nuclei deformation) [90]
Hartree-Fock (mean field) [91]
Additional, about pp-chain and CNO cycle is given by (ab initio (many-body and effective field theory + ANC method + Trojan horse + quantum Monte Carlo) exp formula motivation + poly fits + empirical formulas + standard solar model + screening effect + new facilities) [92].

3.1.3 Cluster models

Despite the fact that many body microscopical models are general enough to explain many kinds of nuclear phenomena, calculations may be complex to perform as the number of nucleons growth. Therefore, in order to tackle the complexity issue, physically consistent models with less constituents are needed.

One proposal for reducing the number of entities is to model the nucleus as a bounded system of clusters. A cluster is a selected subsystem usually composed by more than one nucleon. Then, the nucleus at large is represented by the resulting cover of all of its clusters.

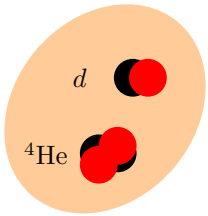

Figure 3.1: Artistic representation of a clustered ^{6}Li nucleus. The nucleus covers a two cluster system with an α particle and a deuterium as its constituencies.

An example of clustering is given with the ^{6}Li nucleus depicted in Figure 3.1. With this picture, it is observed how the number of interacting bodies has decreased from 6 nucleons to 2 clusters: the ^{4}He and deuterium nucleus.

Additionally, it is said that the α particle and the deuterium nucleus are the core and the valence clusters respectively. This classification is analogous to the core and valence electrons used in atomic physics. In particular, the core corresponds to the α particle cluster since it has more nucleons than the valence cluster which is the d nucleus.

On the other hand, in order to give this kind of models physical significance, selected interactions between clusters are introduced. The NN and NNN forces are standard examples of such needed interactions. In addition, since the constituents usually have many nucleons, extended object parameters like mass and charge density distributions may be encountered.

The mass and nuclear density of the nuclei can be modeled as a Woods-Saxon distribution as follows:

$$\rho(r) = \frac{\rho_0}{1 + \exp\left(\frac{r-R}{a}\right)}. \tag{3.2}$$

With folding.

$$\int\int \rho(r_1)\rho(r_2)dr_1dr_2. \tag{3.3}$$

A more detailed survey on cluster models [93].
Microscopical cluster light nuclei [94].
Alpha-cluster alpha-closed shell + Woods Saxon potential [95].
Shell model [96] two center shell model $^{16}\mathrm{O} + ^{16}\mathrm{O}$ [97]
Multicluster $^{12}\mathrm{C} + ^{12}\mathrm{C}$ (3α) [98]
Hartree-Fock $^{16}\mathrm{O} + ^{16}\mathrm{O}$ [99]
Break up effects (four -five body model)[100]
Linear chain (Molecular dynamics) [101]

3.2 Matrix models

The matrix models permit the modeling of resonances with an appropriate fitting of free parameters. In particular, the main formalism in this approach is the R-matrix model [102] and a more recent review [103].

On the other hand, there are matrix models with no free parameters. For example, the K-matrix model predicts the cross sections without including the channel radius, which is an arbitrary parameter required in the R-matrix calculations [104].

Finally, there is more than a single parametrization for matrix models [105]. Usually the alternative formulations surge from the need to express the parameters of the model in order to facilitate the imposition of boundary conditions.

3.2.1 Calculable R-matrix

The model includes free parameter a which is called the radius channel.

$$R_{cc'} = \sum_k \frac{\gamma_{ck}\gamma_{c'k}}{E - E_k}. \tag{3.4}$$

a is a free parameter.
γ, E_k free or not free parameters* Guess: They can be deduced from calculable R-matrix but fitted with phenomenological R-matrix
Picture A: Scattering picture ? - Potential - Microscopical ...
Picture B: Phenomenological by fitting - Raw fitting - R-matrix more sophisticted
Matrix
R-matrix has a connection with the collision matrix, which is closely related with the S-matrix.
S-matrix has already a connection with cross section.
With the difference that a plays some role here.
Channels unified parts with different contribution for a same reaction or resonances.
Does R-matrix serve to deduce the resonant levels?
Or a potential is needed with bounded solution to the Schrödinger equation.
The R-matrix approach serves as a framework for modeling several kind of reactions.
Boundaries or not boundaries. Related with wavefunction

Exchange reaction: (DWBA) Proton capture reaction: (First order perturbation theory + radiative transitions + spin implementation + ..)
WKB: potential to the wave function:
Effective field theory: Low energy L_{QCD}. QCD is SU(3). However, this is unnecessary sophisticated and effective interactions within nuclei can be introduced with fermionic fields.
Chiral and additional topological effects to be used as the description of states.
Difference between state and element of the periodic table. A nuclear state consist of an object associated with a pair of A, Z and also with a certain energy and additional quantum number values.
From the microscopical point of view, there are aspects of the microscopical world to reduced a N-body calculation to clustering or molecular calculations (examples)
Guess: SU(2) of flavor might be here. Mesons can be mediators.
The advantage is that all the quantum field theory machinery is available.
Also lattice quantum field theory could be introduced here if convenient and other stochastic methods that use, for instance, Monte Carlo methods.
The sum is over levels and the elements are parameterized as channels.

Resonances arrives from poles. Deviations from Breit-Wigner resonance prediction. A description on the physical consideration of poles in the scattering (S-matrix) is given in [106].

Applications of the R-matrix formalism to specific reactions:
In primordial nucleosynthesis [107] big-bang 3He and several reactions [108].

Bayesian fitting methods [109].
Litium detueron capture [110].

10B proton non-radiative [111] and similarly [112]. 10B radiative and resonances in 11C inverse kinematics [113].
Alpha capture reactions of carbon [114]. Hybrid potential/R-matrix [115].
13C alpha capture and 16O determination [116].
Proton capture carbon [117] for C12 and [118] for C13 and [119] for the same reaction.

15N capture in [120] and 14N in [121]. also on 14N proton capture [122].

3.2.2 Phenomenological R-matrix

The penetration factor parameter $P(E)$ which is expressed as:

$$P = \frac{\Gamma}{F_l^2 + G_l^2}, \tag{3.5}$$

where the functions $F_l = F_l(ka)$ and $G_l = G_l(ka)$ are the Coulomb functions evaluated at a particular $\rho = ka$. In addition, another parameter Q is given:

$$Q = \frac{\Gamma}{F_l G_l' + G_l F_l'}. \tag{3.6}$$

On the other hand, the phase shift is given by:

$$\delta = \delta_{\mathrm{HS}} + \delta_R. \tag{3.7}$$

An empirical formula obtained from the R-matrix formalism is given by:

$$S(E) = S_r \frac{\Gamma^2/4}{(E - E_r + \Delta)^2 + (\Gamma/2)^2}. \tag{3.8}$$

3.2.3 K-matrix

There is also the K-matrix model as an alternative of the R-matrix model [104]. The advantage of this model with respect to the R-matrix is that the K-matrix does not include the channel radius as a free parameter. Alternative formulation of R-matrix [105].

3.3 Potential models

Nuclei are considered as objects subject to effective interactions.

3.3.1 Effective potentials

These interactions are also modeled by effective potentials which account qualitatively for the nature of the underlying physics behind the nuclear reactions. In particular, different kind of potentials offer a particular shape of the interaction which make them suitable for the modeling of concrete reactions.

Electromagnetic standard potential

The effective interaction between nuclei is referred as a composite effect of the electromagnetic and nuclear interactions.

The first interaction is considered due to the electromagnetic repulsion between the nuclei. In a first approach, the substructure of the nuclei is ignored. Then, nuceli charged cloud is modeled as uniformly charged sphere. Therefore, the corresponding potential is given by:

$$V_{\mathrm{EM}} = \begin{cases} \dfrac{Z_1 Z_2 e^2}{4\pi\epsilon_0 R}\left(\dfrac{3}{2} - \dfrac{r^2}{2R^2}\right), & r \leq R \\ \dfrac{Z_1 Z_2 e^2}{4\pi\epsilon_0 r}, & r > R \end{cases} \tag{3.9}$$

Empirical potentials

Secondly, in order to account for the nuclear force, an short-distance attractive potential is needed to be included. However, unlike the electromagnetic interaction, nuclear potentials might not be deduced in a closed and fundamental form such as the expression given in 3.9. Consequently, these potentials are usually phenomenological and account for specific purposes. In fact, there is a an extent list of potentials available in literature which are used for modeling the interactions of different kind of reactions.

For instance, in a first approximation, there is the step potential.

$$V_{\mathrm{SqW}} = -V_0\theta(r). \tag{3.10}$$

Double exponential potentials:

$$V_{\mathrm{DE}}(r) = -V_0\left(e^{\alpha_1 r} + e^{\alpha_2 r}\right)^{-1}. \tag{3.11}$$

Cluster potential:

$$V_{\mathrm{CL}}(r) = -V_0\exp\left(-\alpha r^2\right) + V_1\exp\left(\beta r\right). \tag{3.12}$$

Gaussian exponential:

$$V_{\mathrm{GE}}(r) = -V_0\exp\left(-\alpha r^2\right). \tag{3.13}$$

Yukawa potential which includes screening effect.

$$V_{\rm Y} = -\frac{c}{4\pi\epsilon_0} e^{-\mu r}. \tag{3.14}$$

Yakovlev et. al model [123] consists of an estimation of the potential that is similar to the parabolic potentials with free parameters that attempt to account for the effects of the nuclear and electromagnetic interactions.

$$V_{\rm YAK} = \begin{cases} E_c \left(3 - \dfrac{r^2}{R_c^2}\right), & r \leq R_{c1} \\ \dfrac{Z_1 Z_2 e^2}{r}, & r > R_{c1} \end{cases} \tag{3.15}$$

proton capture review ^{2}H, ^{6,7}Li, ^{12,13}C reactions (two-cluster potential model, exponential 21, exponential2 + Young's scheme) + poly parametrization [124]
7Be radiative capture(exponential2 + Asymptotic normalization coefficients) [125]
Cross section deduced potential $^{12}\mathrm{C} + ^{12}\mathrm{C}$ and $^{16}\mathrm{O} + ^{16}\mathrm{O}$ reactions (exp(11)-1 potential approximated to exp(-1) empirical potential + Liquid drop radius)[126] Review nuclear potentials heavy-ion reactions (Woods-Saxon and double folding potentials (SPP) + empirical potentials + mean field model Skyrme Hartree - Fock) + poly6 + polyfrac for potential barriers [127]

Woods-Saxon potentials

In order to the potential to be more realistic, a Woods-Saxon potential consider a smooth behavior.

$$V_{\rm WS}(r) = \frac{-V_0}{1 + \exp\left(\frac{r-R}{a}\right)}, \tag{3.16}$$

where V_0 represents the potential depth, a the parametrization and R a computed radius which is defined as:

$$R = r_0(A_1^{1/3} + A_2^{1/3}). \tag{3.17}$$

Further details about capture reactions (potential model Woods-Saxon + spin-orbit coupling + ANC + SF) with single-particle states is given by [128].

Coupled channels E1, M1 and E2 transitions (Woods-Saxon + spin-orbit coupling + spectroscopic factor) [129]
9Be radiative capture. Mostly E1 transition. (modified Woods-Saxon + spin-orbit + SF + ANC) [130]
11C radiative capture (modified Woods-Saxon + spin orbit coupling)[131]
On the other hand, it is relevant, specially at low energies, the inclusion of angular momentum effects in the potential. In order to account for that effect, there is the potential with angular moment.

$$V_{\rm WS} = -V_0 f(r), \tag{3.18}$$

Fermi-Dirac distribution like term:

$$f(r) = \frac{1}{1 + \exp\left(\frac{r-R}{a}\right)}. \tag{3.19}$$

Surface Fermi-Dirac, which is related to the derivative, is a distribution like the following term:

$$f_{\rm S}(r) = \frac{\exp\left(\frac{r-R}{a}\right)}{\left(1 + \exp\left(\frac{r-R}{a}\right)\right)^2}. \tag{3.20}$$

$$V_{\rm GWS} = -V_0 f(r) - V_1 f_{\rm S}(r). \tag{3.21}$$

Woods-Saxon and Generalized Woods-Saxon potential. Cut-off inclusion for numerical implementations. Woods-Saxon potential can be solved analytically with $l = 0$ [132]
coupled channels and modified energy dependent diffuseness parameter for modified Woods-Saxon [133]
$V_0(E)$ and $a(E)$

Spin orbit contribution

On the other hand, it is relevant, specially at low energies, the inclusion of angular momentum effects in the potential. In order to account for that effect, there is the potential with angular moment.

Also, spin orbit coupling effect is noticeable for certain kind of reactions. The contribution to the potential associated with this effect is expressed as:

$$V_{\mathrm{SO}}(r) = k\langle L \cdot S\rangle \frac{1}{m_\pi r}\frac{d}{dr}V(r), \tag{3.22}$$

where the coupling $\langle L \cdot S\rangle$ is expressed as:

$$\langle L \cdot S\rangle = J(J+1) - l(l+1) - s(l+1). \tag{3.23}$$

Optical potentials

Optical model (Modified Woods-Saxon energy dependent) ^{12}C with $A = 6$ projectile reactions + double folding São Paulo (SPP) and double folding cluster model dynamic polarization potential + poly2 empirical formulas [134].

Hill-Wheeler approximation for transmission probability and applications in fission reactions [135].
Hill-Wheeler approximation application to $^{11}\mathrm{Li} + {}^{12}\mathrm{C}$ reaction + optical model + Wong's formula [136].
Coupled channels + optical potential + polarization + Hill-Wheeler approximation + WKB approximation [137].

$$V(r) = V_R(r) + iW_R(r). \tag{3.24}$$

Optical energy dependent model (parabolic approximation with analytical cross section) [138]

3.3.2 Calculations

The potentials just introduced are useful for the calculation of cross sections and, therefore, S-factors. The connection between potentials and cross sections depends on the kind of reaction to be modeled. In the general approach, cross sections are directly computed form wave functions, which are numerically estimated from the numerical solution of the Schroödinger equation.

WKB approximation

Fusion cross section calculations using the WKB approximation method are closely related with the Barrier penetration model (BPM). In this model, the factor $\Phi(E)$, which was introduced in section 1.2.2 and in equation 1.23, is calculated for the effective potential, which consists of the sum of the nuclear, electromagnetic and centrifugal terms. The last term is associated with an specific l value. Then, it is possible to compute the transmission coefficient T_l for each value of l as it is given by [43]:

$$T_l = \frac{1}{1 + \exp(\Phi(E))}. \tag{3.25}$$

Subsequently, a summation over all the values of l is performed until convergence is achieved. It turns out that there is a direct relation with the fusion cross section and the referred sum as it is expressed by [43, 58]:

$$\sigma = \frac{\pi}{k^2} \sum_l (2l+1) T_l, \tag{3.26}$$

where $k = \sqrt{2\mu E/\hbar^2}$ and μ corresponds to the reduced mass of the reactant nuclei.

It is quiet remarkable that the calculation of the cross section of a sophisticated process like the fusion reaction can be reduced to a discrete sum of transmission coefficients. In fact, the expression of equation 3.26 does not need to take into account the outcome of the initial or final state. It also, it permits the evaluation of the cross section without considering further details about the structure of the fusing nuclei.

However, the BPM has the main disadvantage that does not account for couplings that might exist among the sub components of the nuclei. In particular, this approach, at it will be detailed later in this work, lens to underestimate the cross-section values for nuclei. In order to overcome this issue, further models, like the zero point motion model (ZPM), are introduced in literature [46, 58].

Additionally, there are empirical alternatives to the calculation of S-factor by introducing additional free parameters. For instance, in the Yakovlev et. al potential model, the S-factor is parametrized in two regions and it uses two free parameters. The details of this model are going to be introduces, as they given in [123]. For the first region, which consists of energies below the Coulomb barrier E_c, the astrophysical S-factor is estimated as:

$$S(E) = S_0 \exp(\Psi(E)), \tag{3.27}$$

with $\Psi(E)$ defined as:

$$\Psi(E) = 2\pi\eta(E) + \Phi(E), \tag{3.28}$$

where $\eta(E)$ is the Sommerfeld parameter, and $\Phi(E)$ is the wavefunction calculated by the WKB, which is given in equation 1.23 with $m = \mu$, where μ corresponds to the reduced mass of the colliding nuclei. Further details on the calculation of the last parameter are presented in section 1.2.2.

It is worth noticing that S_0 corresponds to a free parameter closely related with the S-factor value extrapolation at zero energy. In addition, as it happens usually to free parameters, S_0 is determined by fitting the model with experimental data.

On the other hand, for the second region, which corresponds to energies above the barrier, the S-factor is given by:

$$S(E) = S(0) \exp(2\pi\eta(E)) \sqrt{\frac{Ec}{E}} \left(1 + \xi \frac{E - E_c}{E}\right), \tag{3.29}$$

where ξ is the other free parameter which accounts for the deviation from Coulombic behavior of the S-factor.

Exchange reactions

The form of the reaction is $A(a,b)B$. Then, there are four interacting nuclei and two substeps that account for the global behavior of the reaction . In fact, depending on a and b nuclei, there are two options the reaction to proceed [12].

The first option is related with $a \to x + b$, $A + x \to B$ and happens when a is heavier than b. In contrast, the second option has the processes: $a + x \to b$ and $A \to B + x$, which are possible if a is lighter than b.

Distorted Born wave approximation (DWBA) is privileged for exchange reaction calculations.
The transition matrix is expressed as.

$$\langle \phi_c | \frac{\phi}{r} | \phi'_c \rangle. \tag{3.30}$$

Radiative capture reactions

Given that photons are emitted in these processes, it is essential to model the reaction as the composed effect of all electromagnetic transitions going from a bounded to a continuum state.

In fact, each transition is classified depending of its origin and multipolarity. The first criteria distinguish whether the transition has electric or magnetic nature. The second item is related to the order of the contribution in terms of the multipole expansion. For example, E1 corresponds to an electric transition of first, which corresponds to an electric dipole.

Since contributions from higher multipolarity decay more rapidly, the most important contributions to the cross section of the process are dipole radiation. Additionally, electric transitions are stronger than magnetic transition in a factor of c^2/v^2, which is noticeable given that energies are non-relativistic.
In addition, parity must be considered for each reactant. For example, photon has $\pi = -1$. Therefore, when electric processes are given, the product of initial π_1 and final π_2 parties must take into account whether the transition is electric or magnetic. More particularly, the referred product has the form:

$$\pi_1 \pi_2 = \begin{cases} (-1)^{\lambda}, & \mathrm{E}\lambda \\ (-1)^{\lambda+1}, & \mathrm{M}\lambda \end{cases} \tag{3.31}$$

In the last equation, Eλ and Mλ denote electric and magnetic transitions with multipolarity λ.

As it happens in all reactions, the total angular momentum is conserved. Then, all the spin, orbital and total contributions should be considered. With this picture given, it is imperative the use of Clebsh-Gordan coefficients.

In the radiative capture reactions, cross sections are computed based on electromagnetic field operators as it is observed by [128]:

$$\sigma_m = \sum_k \langle k | \mathcal{O} | m \rangle C_{klm}. \tag{3.32}$$

It is usual that certain transitions cannot be completely described by equation 3.32. In order to account for defect, some authors introduce a new constant called spectroscopic factor for each transition such that the total cross section of the process is expressed as:

$$\sigma = \sum_m (SF)_m \sigma_m, \tag{3.33}$$

where each SF_m correspond to the weight of the mth transition.

Usually, this new term is obtained by experimental fitting [130, 12]. However, it is also common to find the spectroscopic factor to be set at $SF_m = 1$ for all transitions [129].

Fusion reactions

On the other hand, in certain specific cases when the expressions of the potentials are not mathematically sophisticated, approximations can be made. In particular, WKB approximation offers a comprehensive approach towards handy estimation of the cross sections.

3.3.3 Folding

During the previous discussion, mass and charge distributions were not considered in detail. However, with nuceli with higher mass, the intrinsic distribution of the mass and charge gains relevance in the reaction cross section estimation. In particular, mass and charge is usually concentrated at the center of the nuceli and there is a sharp drop of the mentioned variables in the surrounding of the radius.

In order to account for this effect, an initial formula which accounts
São Paulo [139]

$$V_{\mathrm{SPP}}(r) = V_{\mathrm{F}}(r) e^{-4V^2/c^2}. \tag{3.34}$$

$$V^2 = \frac{2}{\mu}\left(E - V_{\mathrm{F}}(r) - V_{\mathrm{C}}(r)\right), \tag{3.35}$$

where the reduced mass is μ, the Coulomb potential is $V_{\mathrm{C}}(r)$ and the folding potential $V_{\mathrm{F}}(r)$ is expressed as:

$$V_{\mathrm{F}}(r) = \int\int \rho_1(\vec{r}_1)\rho_2(\vec{r}_2)\delta(\vec{r} - \vec{r}_1 + \vec{r}_2)d\vec{r}_1 d\vec{r}_2. \tag{3.36}$$

An illustration is planned to appear in Figure 3.2.

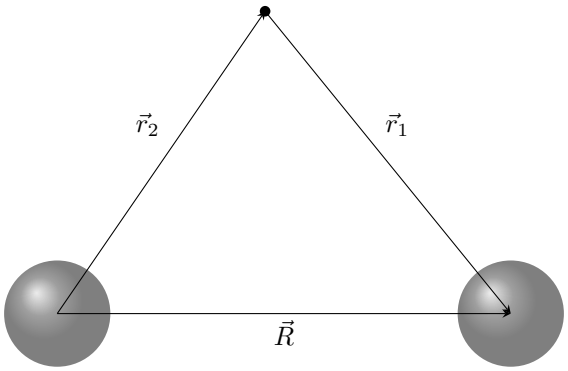

Figure 3.2: Double folding model calculation illustration. This figure is under elaboration.

Capture reaction review light nuclei (Double folding model + Yukawa-like + spin orbit coupling)[140]

3.3.4 Non-locality

And, potentials with non-locality are also found in literature. For example, there is the São Paulo potential that accounts for the effect of non-local interactions between the interactant nuclei.

p2H radiative capture E1, M1, E2 (exponential 21 + variational method + Young's scheme) [141]
2Hdp reaction in metallic environments (theoretical and experimental screening effect) [142]

13C radiative capture (modified Woods-Saxon + spin-orbit + SF + ANC) , R-matrix treatment for resonant cross section and poly2 empirical formula [143] potential cluster model (exp2 potential + variational method + Young's schemes) [144]
16O fusion two-center shell model with Wood-Saxon potentials (cranking and reduced mass + molecular dynamics) [145]

3.4 Special models

Models which do not fit in the previously presented categories.

3.4.1 Trojan Horse models

It occurs in a two step reaction process as expressed in:

$$A + B \rightarrow a + (b + x) \rightarrow a + (c + d), \tag{3.37}$$

where the first and second steps correspond to the $A+B \rightarrow a+(b+x)$ and $b+x \rightarrow c+d$ reactions respectively. Notice that the b nucleus does not appear as a final product of the reaction as it is consumed in the second step.
The Trojan horse method. Selection of reactions and consideration of the characteristics of the nuclei to be considered in the method [146].

3.4.2 Effective field theories

Based on effective field theories. The general principle of these theories is that nuclear interactions correspond to low-energy approximate solutions of the physics described in quantum chromodynamics.

$$\mathcal{L} = N^{\dagger} i\hbar\gamma^{\mu}\partial_{\mu}N + ... \tag{3.38}$$

Diagrams associated with the processes of low-energy nuclear force. Mediators are mesons like pions.

Effective field theory $^{2}\mathrm{H}(\mathrm{p},\gamma)^{3}\mathrm{He}$ and three body interaction, M1 is the dominant contribution [147]
Halo effective field theory $^{7}\mathrm{Be}(\mathrm{p},\gamma)^{8}\mathrm{B}$ reaction + coupled channel implementation + two theories with and without ^{7}Be excited core + E1 and M1 transitions + ANC + Bayesian analysis Metropoli-Hasting algorithm + polynomial empirical formula [148].

3.4.3 Hybrid models

These models include aspect of potential, microscopical and even R-matrix models. For example, there are models with clustering and effective potentials.

3.5 Empirical formulas

And some empirical formulas can be given.

3.5.1 Interpolations

Non-resonant reactions S-factors can be calculated with polynomial interpolations and fits.
In particular, there is a polynomial expansion that is reported in literature to be useful.

$$S(E) = \exp\left(g_0 + g_1 E + g_2 E^2 + g_3 E^3 + ...\right). \tag{3.39}$$

Also, more generic expansions are modeled by fitting a Laurent series expansion.

$$S(E) = \frac{a_{-1}}{E} + a_0 + a_1 E + a_2 E^2 + ... \ . \tag{3.40}$$

For most of the reactions, $a_{-1} = 0$, since $S(E)$ should be smooth at very low energies. Therefore, the S-factor is described as a Taylor series expansion.

$$S(E) = a_0 + a_1 E + a_2 E^2 + ... \ . \tag{3.41}$$

3.5.2 Fusion reactions formulas

Fusion reactions, which is a more sophisticated model [149].

$$S(E) = \sum_{k=0}^{N} a_k E^k + \left(1 + \exp\left(1 + \frac{E_c - E}{D}\right)\right)^{-1} \sum_{l=0}^{M} b_l E^l. \tag{3.42}$$

3.5.3 Resonances and composite formulas

For resonant reactions, the Breit-Wigner formula

$$S(E) = S_r \frac{\Gamma_r^2/4}{(E - E_r)^2 + (\Gamma_r/2)^2}. \tag{3.43}$$

This formulation permits empirical formulas to add resonant terms to the non-resonant estimation. Usually the resonant terms are added to background which is fitted to a non-resonant formula. For example, consider the expression:

$$S(E) = \sum_{k=0}^{N} a_k E^k + \sum_{l=1}^{M} \frac{\Gamma_l^2/4}{(E - E_l)^2 + \Gamma_l^2/4}, \tag{3.44}$$

Analogously, if the non-resonant term has a polynomial form, the S-factor hybrid resonant and non-resonant expansion is expressed as:

$$S(E) = \exp\left(\sum_{k=0}^{N} a_k E^k\right) + \sum_{l=1}^{M} \frac{\Gamma_l^2/4}{(E - E_l)^2 + \Gamma_l^2/4}, \tag{3.45}$$

where N is the maximum order of the polynomial to be fitted, which accounts for the non-resonant behavior of the reaction, and M represents the number resonances present in the reaction.
Applications in direct capture [150]. Exchange reactions (p, n) kind [151].
Charged particle collisions non-resonant [152] and resonant [153].

Chapter 4

S-factor calculations for selected reactions

Astrophysical S-factor calculations for a selected list of reactions will be presented. The list of reactions distinguish between resonant and non-resonant reactions. Additionally, reactions from various astrophysical environments like Big Bang Nucleosynthesis, pp-chain, CNO cycle and middle heavy nuclei fusion are included.

Selected reactions calculations are based on specific models, which are conveniently chosen to reproduce the S-factor behavior. Particularly, since most of microscopical and R-matrix treatments require sophisticated parametrizations and imply considerable computational resources, potential models and empirical formulas are preferred as a first approximation for S-factor calculations in this work.

Potential models and empirical formulas usually include free parameters. The values of these parameters are fitted to experimental data in order to obtain the error minimizing prediction. Consequently, S-factor experimental data gathering is of special concern in this work. In order to account for this need, several experimental data sources were consulted. Most of these references were extracted form databases like NACRE II [12]. Further related details are given in Appendix A.

With experimental data given, fitting of the S-factor values of the selected reaction follows. Details corresponding to fitting procedures are covered in Appendix C. In particular, the values of the fitting parameters determined in this work are detailed in Section C.2.

In order to perform the numerical computations for fits, a set of programs were written as specified in Appendix E. The programming language used was Python [154]. In addition, data management depended on Pandas [155], numerical computations were performed on top of subroutines from NumPy [156], fitting parameters were obtained with SciPy [157] and data was visualized with the support of Matplotlib [158].

The evaluation of the models to be studied in this chapter is divided in two main parts: non-resonant and resonant reactions. In addition, for each subsection of the chapter, calculations considerations are included. Subsequently, the results and analysis on the S-factor calculation for each selected reaction are presented.

4.1 Non-resonant reactions

The results produced by this work starts with the study of the background of the S-factor energy curves for the selected reactions. In particular, most of the backgrounds of reactions are modeled as having non-resonant behavior. Then, the study of non resonant reactions has priority as a first approximation to the

calculation of the astrophysical S-factor.

The selected non-resonant reactions include light heavy nuclei exchange reaction $^2\mathrm{H(d,p)^3H}$ and radiative capture reaction $^2\mathrm{H(p,\gamma)^3He}$. The first reaction is critical for Big Bang Nucleosynthesis since it provides a way of fusing deuterium, which is essential for the production of heavier nuclei in the early universe [17]. The second reaction is a pivotal process in the pp-chain as it produces ^{3}He, which is a prerequisite for producing the ending product of the chain ^{4}He [25].

On the other hand, the middle heavy nuclei fusion reactions to be considered contain carbon and oxygen isotopes as reactants. These type of reactions are considered since the low-energy study of these two reactions are of recent research interest [39, 41, 51]. In fact, new successful models usually include aspects inherent on middle heavy nuclei like clustering [42] or couplings to vibrational modes [46].

Particularly, the $^{12}\mathrm{C} + {}^{12}\mathrm{C}$ and $^{16}\mathrm{O} + {}^{16}\mathrm{O}$ reactions are selected since they are essential for the burning process in massive stars at the end period of their lives. Additionally, the $^{12}\mathrm{C} + {}^{16}\mathrm{O}$ reaction is also chosen due to the relevance of the study of the fusion of the two more stable carbon and oxygen nuclei. Lastly, other oxygen fusion channels like $^{16}\mathrm{O} + {}^{17}\mathrm{O}$ and $^{16}\mathrm{O} + {}^{18}\mathrm{O}$ are selected given their close relation to the $^{16}\mathrm{O} + {}^{16}\mathrm{O}$ reaction, as well due to the existence of inelastic contributions corresponding to excited O^{17*} and O^{18*} nuclei [48].

4.1.1 Calculation considerations

Empirical formulas are initially considered for the light heavy S-factor description. In particular, the non-resonant part of the equations 3.45 and 3.44 are fitted to experimental data.

Fitting parameters to best describe experimental data were determined for empirical formulas. In particular, the parameters chosen minimized the chi-squared χ^2 function as it is described in appendix C. In some cases, it was necessary to constraint the interval of validity of the parameters in order to avoid unphysical behaviour of the fittings. Further details about this constraints can be found in section C.2.

On the other hand, fusion reactions are described by the Yakovlev et. al empirical formula [149] and analytical potential model [123].

Particularly, in the Yakovlev model, parameters are fitted as follows: The initial free parameters are δ, E_c, ξ and S_0 which parametrize the nuclear-electromagnetic transition of the potential, the Coulomb barrier, the asymptotic value of the S-factor at higher energies and the low energy extrapolation of the S-factor respectively.

Then, additional parameters are introduced in order to take into account the atomic and massive numbers of the colliding nuclei. For example, the Coulomb barrier like term is given in terms of a new parameter R as follows:

$$E_c = \frac{\alpha}{R}, \tag{4.1}$$

where $\alpha = \sqrt{Z_1 Z_2 e^2}$ and R is determined in terms of the mass numbers A_1 and A_2 as well as the atomic numbers Z_1 and Z_2 of the reacting nuclei as:

$$R = R_0 + \Delta R_1 |2Z_1 - A_1| + \Delta R_2 |2Z_2 - A_2|. \tag{4.2}$$

In particular, the parameter R_0 is unique for a given combination of Z_1 and Z_2 values, the parameters ΔR_1 and ΔR_2 are specific for each reactant nuclei. In addition, this parameter takes different values given in the following way:

$$\Delta R_1 = \begin{cases} \Delta R_{10}, & 2Z_1 \geq A_1. \\ \Delta R_{11}, & 2Z_1 < A_1. \end{cases} \tag{4.3}$$

Analogously, ΔR_2 is determined as:

$$\Delta R_2 = \begin{cases} \Delta R_{20}, & 2Z_2 \geq A_2. \\ \Delta R_{21}, & 2Z_2 < A_2. \end{cases} \tag{4.4}$$

In quiet a similar manner, the ξ parameter is expressed in terms of two new parameters ξ_0 and ξ_1 with the form:

$$\xi = \xi_0 + \xi_1(A_1 + A_2). \tag{4.5}$$

Then, ξ_0 can be interpreted as a zero order approximation for ξ while ξ_1 is the correction term coupled to the total mass number of the reacting nuclei.

The numerical values of the 9 lastly mentioned parameters are provided in the Table II contained in [123].

Finally, although Yakovlev et. al model is used for middle-heavy fusion reactions, is not expected to work for radiative capture reactions since it predicts a decrement of the S-factor for all energies. In contrast, the S-factor increases in radiative capture reactions.

4.1.2 Results and analysis

Results are given in this section regarding to the $^2\mathrm{H(d,p)}^3\mathrm{H}$ reaction as presented in Figure 4.1.

Initially, polynomial interpolations were calculated with orders $N = 1$ to $N = 5$ as it is visualized in Figure 4.1a. The generality of these fits is that the greater the polynomial order, the better the fit. In particular, the best is obtained with a polynomial of order $N = 5$.

Similarly, exponential interpolations were obtained with N ranging from 1 to 5. These fits are visualized in Figure 4.1b. Additionally, as it happens with polynomial fits, the best fit is given with $N = 5$. However, the polynomial fitting approach gives a better result than this exponential treatment.

In particular, this difference could be attributed to the fact that exponential fitting is more ideal when the order of magnitude varies considerably. Therefore, since the S-factor values have all roughly the same order of magnitude, the fitting capacity of the exponential function is limited. In addition, given that exponential fit leans to reproduce data with higher S-factor values, which happens because choosing to fitting better these data points will minimize the square error, the low energy entries are more sensible to errors.

Additionally, it is observed that fits slightly overestimate the reaction S-factor at the lower energies of the plot. This deviation is due to the fact that values from RA02 data principally, as well as GR95 data in a minor extent, are pushing the S-factor estimations up. This S-factor increase is attributed to enhancements caused by the screening effect. A treatment of this S-factor increase is going to be treated in a moment.

In fact, it is noticeable that very low energy values for the S-factor are not entirely consistent since various experiments give noticeable different values for points with similar energy. Then, an additional fifth order fit called poly5-exclude was calculated by not including disruptive data in which are included RA02 and GR95. This fit is visualized, with polynomial and exponential order five fits, in the best fit graph given in Figure 4.1c.

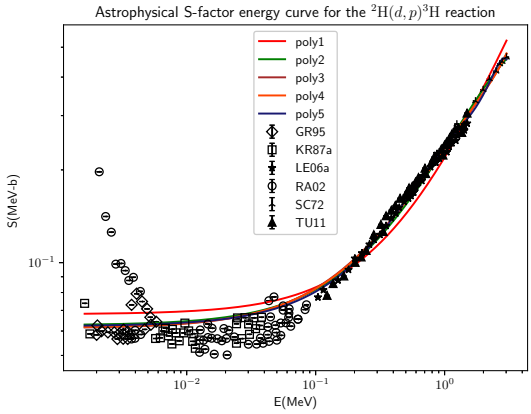

(a) Polynomial fits.

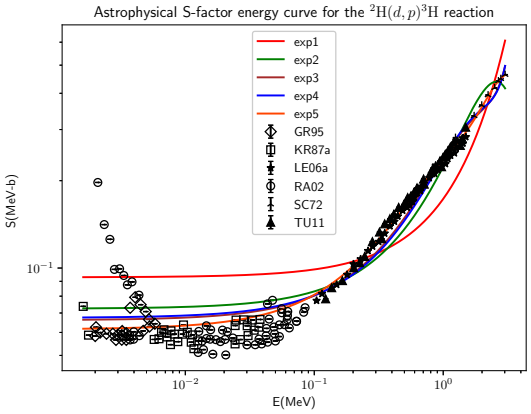

(b) Exponential fits.

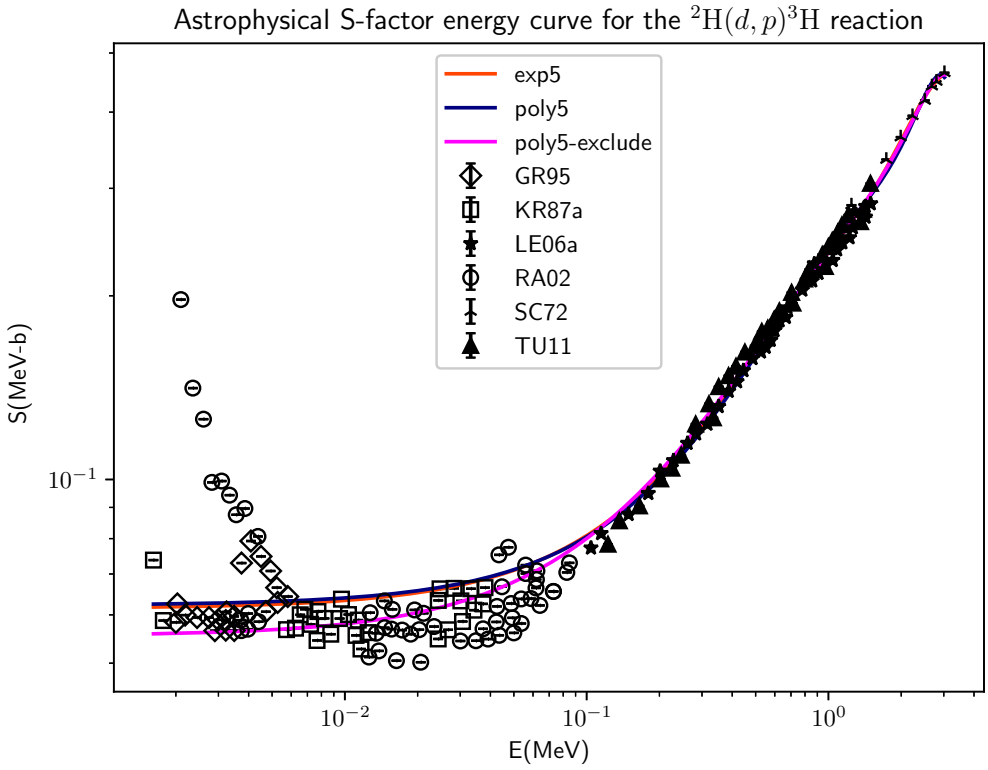

(c) Best fits.

Figure 4.1: Empirical formulas fitted to ^{2}H(d, p)^{3}H reaction S-factor data. In panel a), poly1, poly2, poly3, poly4, and poly5 represent fits to polynomials from 1st to 5th order. Similarly, in panel b), exp1, exp2, exp3, exp4 and exp5 represent exponential fits up to 5th order. Additionally, in panel c), poly5-exclude corresponds to a poly5 fit without data from RA02 and GR95. References to the sources of the black colored experimental points are given in Table A.1. Fitting parameters values are given in Tables C.2 and C.3.

Now, resuming the screening effect considerations, at low-energies as far as 10^{-3} MeV $< E < 10^{-2}$ MeV,

an exponential-like damping of the S-factor is observed. In fact, this behavior could explained due to the electron screening effect [26]. In particular, the enhancement factor f for the S-factor is defined as [27]:

$$f = \frac{E}{E + U_e} \exp\left(\frac{\pi \eta U_e}{E}\right), \tag{4.6}$$

where E is the center of mass energy, η is the Sommerfeld parameter and U_e is a parameter that quantifies the degree of enhancement of the S-factor. The sharp increase of the S-factor at low energies is explained by the shielding of the Coulomb potential produced by the electron cloud that surrounds the interacting nuclei [27]. In particular, this dismissal of the strength of the potential reduces the Coluomb barrier. Therefore, as the tunneling probability increases, the cross-section, and thus the S-factor, of the reaction also increases.

Additionally, the value of the U_e parameter is usually obtained by fitting. An example of such fitting is found in the graphs of Figure 4.2.

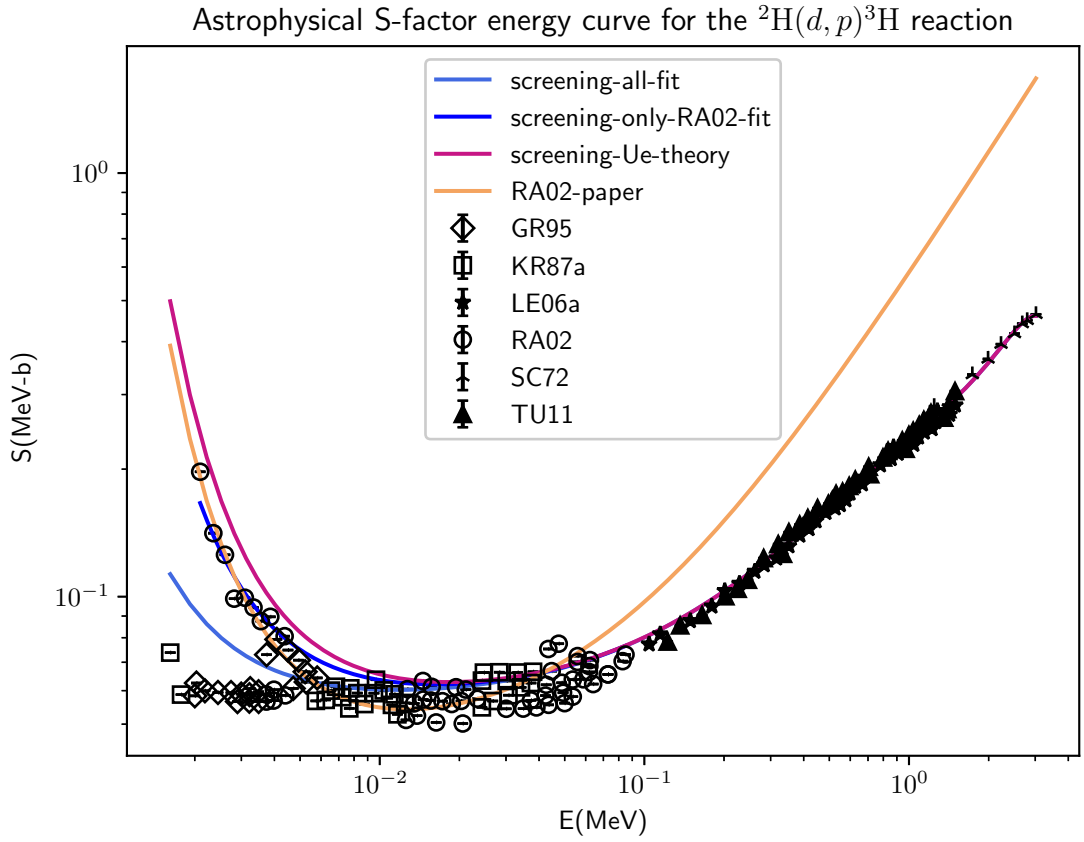

Figure 4.2: Polynomial fits to experimental data with screening effect. The curve labeled as screening-all-fit is obtained by fitting U_e with all data points, screening-only-RA02-fit is obtained only with RA02 data, *screening-Ue-theory* is calculated with U_e fixed to the value given in RA02. The poly5-exclude fit of Figure 4.1 was used as the S-factor estimation without screening of the last three curves. Additionally, the screening-RAO2 curve presents the S-factor prediction made in the RA02 paper. Further details about the fitting parameters and their values are given in Table C.4.

Initially, the RA02 calculation [26] was tested against data. This estimation is referred as RAO2-paper in

the last plot. Despite the fact that this prediction is able to accurately reproduce the S-factor values of their measurements, namely those marked with the RA02 tag, it is unable to fit appropriately points with higher energies than 0.1MeV. Then, a more comprehensive fitting was needed to be introduced.

In response to this improvement need, the poly5-exclude curve for background estimation calculated in this work was used. Then, in order to account for the screening data, the enhancement factor given in equation 4.6 was multiplied to the background estimation. In a first approach, a fitting with all data was made, which is visualized with the label screening-all-fit. However, since the S-factor prediction for the RA02 entries were improvable, a second curve was determined by only taking into account RA02 data, which is given the name of screening-only-RA02-fit. In this case, the fit appropiartely fits both the screening affected RA02 data and the remaining background. Therefore, this result can be regarded as an improvement for the RA02 calculation.

Finally, as is visualized in the curve labeled as screening-Ue-theory, the S-factor background estimation calculated in this work also approximates acceptably the S-factor values with the value of the U_e parameter given in the RA02 paper [26]. In particular, details regarding the determination of this parameter are encountered in Table C.4.

The analysis now proceeds with the study of the S-factor curves related to the $^2\mathrm{H}(\mathrm{p},\gamma)^3\mathrm{He}$ presented in Figure 4.3. This reaction was treated in a similar manner than previous reaction since there are polynomial and exponential fits. However, there is not a considerable screening effect caused S-factor enhancement.

Firstly, polynomial interpolations fits were determined. The result of this fitting is visualized in Figure 4.3a. As it happened with the polynomial fits related to the $^2\mathrm{H}(\mathrm{d},\mathrm{p})^3\mathrm{H}$ reaction, there is a general tendency of S-factor estimation improvement with the increase of polynomial order. However, in this case the best fit occurred with $N = 4$, not with $N = 5$.

A possible cause of this finding can be associated with parameter overestimation. In addition, it is essential to comment that it was not possible to obtain fitting parameters without constraints, which eventually affected the least-squares optimization process. Then, it was likely that the polynomial with $N = 4$ had the necessary parameters to reproduce the S-factor results but also the sufficient number of them to not overestimate the selection of data with higher energies, as it happens with the $N = 5$ interpolation.

Secondly, exponential fits were calculated with results visible in Figure 4.3b. Fits approximate better to S-factor values with greater N. However, in the $^2\mathrm{H}(\mathrm{p},\gamma)^3\mathrm{He}$ case, the fits do not entirely converge for low energy values. In particular, it seems that the fitting process is choosing the higher S-factor values rather than lower values for error minimizing. Then, it is more complex to this empirical formula to account for low energy data. This reasoning is similar to those made when commenting the exponential fits of the $^2\mathrm{H}(\mathrm{d},\mathrm{p})^3\mathrm{H}$ reaction.

Lastly, selected fits are zoomed in as it is shown in Figure 4.3c. Given the comparison of the fits, it follows that the most robust is given by the fourth order polynomial interpolation.

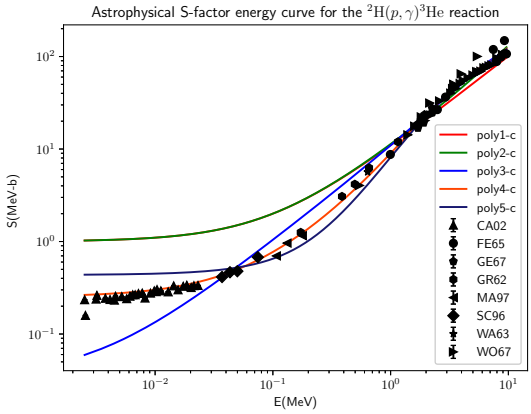

(a) Polynomial fits with constraints.

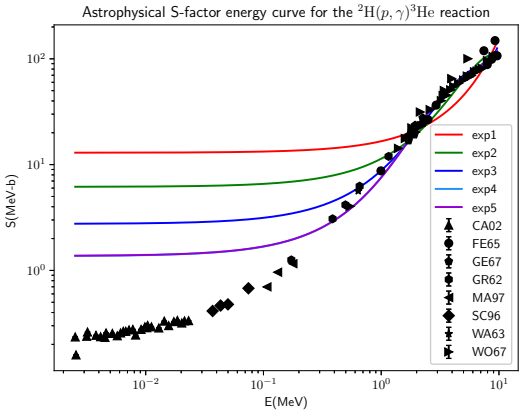

(b) Exponential fits.

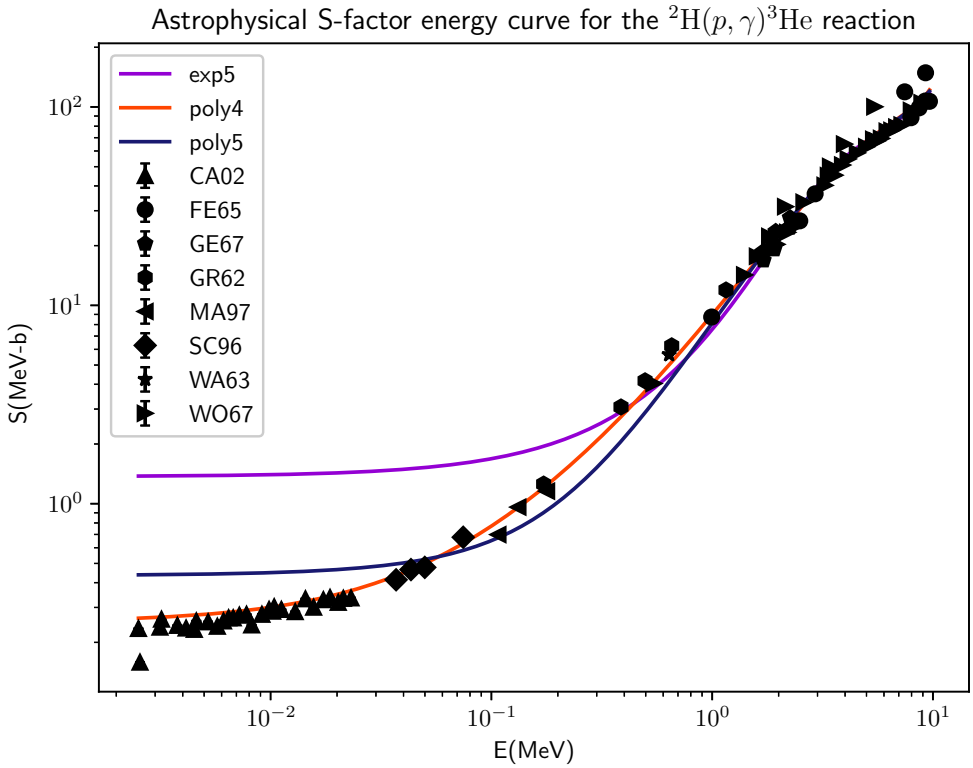

(c) Selected fits.

Figure 4.3: Empirical formulas fitted to the S-factor for the ^{2}H(p,γ)^{3}He reaction. In panels a) and b) polynomial and exponential fits up to fifth order are presented respectively. In particular, the fit parameters used for the graphs in panel a) were constrained. Additionally, in panel c), the best selected fits are visualized. The references to the experimental points are given in Table A.1. The values of the fitting parameters are encountered in Tables C.5 and C.6.

With respect to middle heavy nuclei fusion reactions, the Yakovlev et al. model of [123] is considered as the

analytical model. In addition, Beard and collaborators, in which Yakovlev is included, present an empirical formula useful to reproduce middle heavy fusion behavior [149] is also used.

In this work, fits are done based on the previous empirical formula with the advantage that parameters are determined by fitting data points directly. In contrast, both of the referenced approaches attempt to estimate São Paulo potential model calculations which are not necessarily close to actual experimental data, specially at energies below the Coulomb barrier.

As a starting point, S-factor estimations for the $^{12}C + ^{12}C$ reaction are presented in Figure 4.4 using the potential and empirical Yakovlev estimations, as well as empirical fits to equation 3.42 with $N = 3$ and $M = 2$. In addition, data survey for this reaction was concentrated at energies below the Coulomb barrier given that both of the cited models were already tested successfully at energies above the barrier against experimental data.

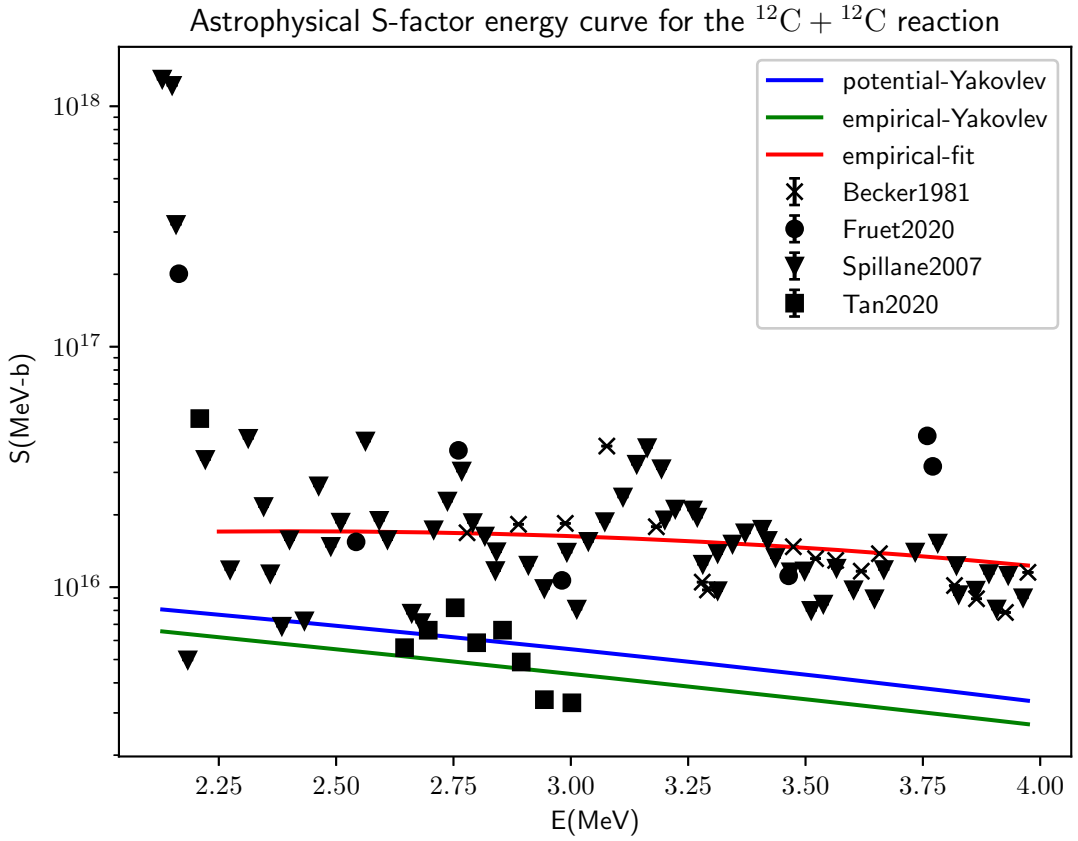

Figure 4.4: Astrophysical S-factor prediction for the $^{12}C + ^{12}C$ reaction as parametrized in the Yakovlev et. al analytical potential model [123]. In addition, two empirical fittings are included. Experimental points references are presented in Table A.3. Parameters related to empirical fits are given in Table C.9.

It is observed that both the potential and empirical external calculations underestimate the value of S-factor. Meanwhile, the plot calculated from this work passes through most of data points. This distinction is not exclusive for the $^{12}C + ^{12}C$ reaction. In fact, this is a pattern present in more middle heavy fusion reactions.

Additionally, one of the key features of the $^{12}C + ^{12}C$ channel is the presence of various low-energy resonances [44]. In fact, this resonant behavior seems to be out of the scope of the Yakovlev potential predicting capacity, as well certainly far from being taken into account with the empirical formula used. Therefore, further predictions should be able to parametrize this resonances and to give a more accurate S-factor estimation with composite non-resonant and resonant contributions.

In fact, the $^{12}C + ^{16}O$ reaction also presents resonant peaks at energies below the Coulomb barrier as it is seen in Figure 4.5 and as it is reported in literature [51].

As it happens with the $^{12}C + ^{12}C$ reaction, this work fit passes through most of the experimental points up to a certain energy, when there is a deviation from the main behavior of the S-factor data. In contrast, both of the Yakovlev et al. estimations underestimate the S-factor values at low energies but predict closely values at higher energies.

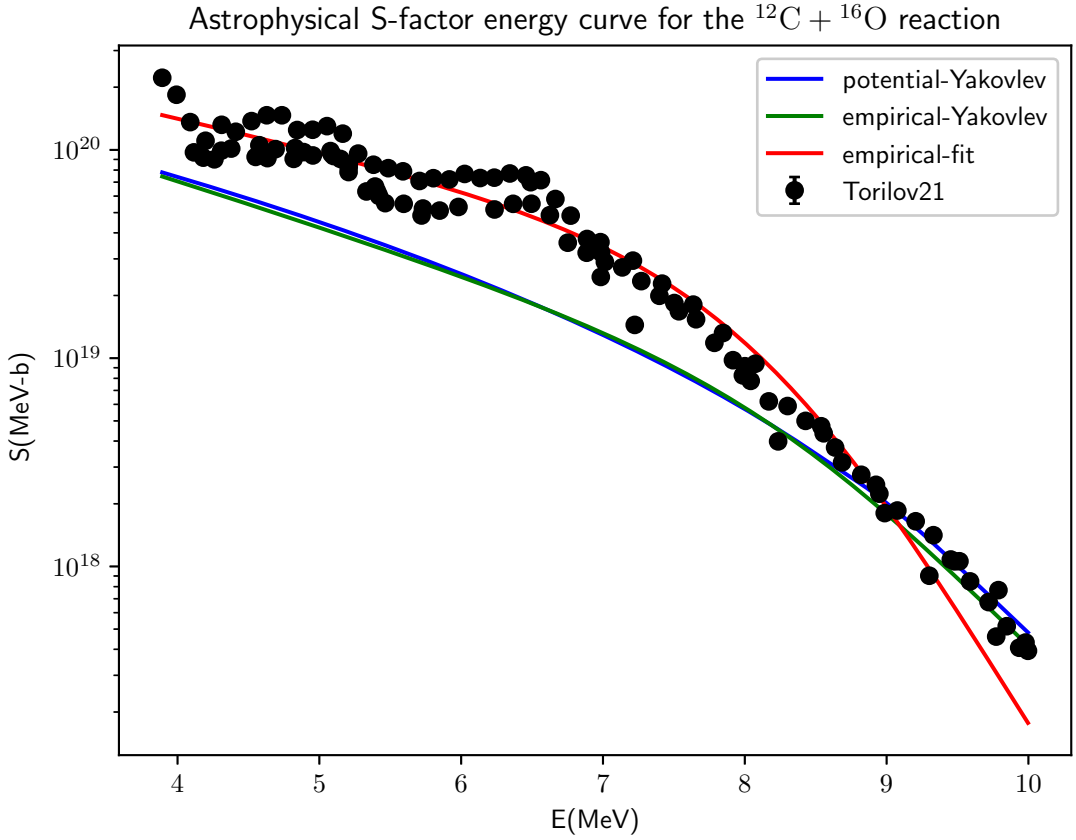

Figure 4.5: Astrophysical S-factor prediction for the $^{12}C + ^{16}O$ reaction as parametrized in the Yakovlev et. al analytical potential model [123]. Additionally, two empirical fittings are included. The reference for the experimental points is given in Table A.3. The values of the empirical fits parameters are given in Table C.10.

This difference might be explained by considering that the fittings presented in work are minimizing error by usually choosing to fit more appropriately values with higher S-factor. This bias could sufficiently explain

why the accuracy of S-factor calculations decreases at energies above the Coulomb barrier. On the other hand, discrepancies between the predictions of the cited models and data are produced since they do not account for aspects inherent to the microscopical behavior of middle heavy nuclei like carbon and oxygen [46].

In particular, since Yakovlev et al. are based in barrier penetration models like the São Paulo model reported in [123] which does not account for nuclei substructures, it underestimates the fusion cross section since this approach does not include details on the nuclei like coupling with inelastic states or the existence of screening effect S-factor enhancement [43].

In a similar way, the S-factor of oxygen fusion reactions of Figure 4.6 present low-energy differences in the prediction at low energies for the referred Yakovlev et al. calculations. Then, the empirical fitting proposed in this work serves as an improvement for low energy data extrapolation.

With respect to the results related to the $^{16}O + {}^{18}O$ reaction as presented in Figure 4.6c, it is observed how the fit calculated in this work estimates appropriately the S-factor for the complete range of energies of the graph. On the other hand, as anticipated, the cited models underestimates the S-factor at energies below the Coulomb barrier.

Similarly, the S-factor values related to the $^{16}O + {}^{17}O$ reaction illustrated in Figure 4.6b shares a similar behavior as compared to the previous reaction. However, there were not available calculations for the Beard et al. empirical formula. Additionally, both of the fits were less accurate than those presented for the $^{16}O + {}^{18}O$ reaction analysis.

This difference might be caused because of inherent aspects of the ^{17}O nuclei. In particular, it is known the existence of inelastic channels related to both ^{17}O and ^{18}O nuclei [53]. Moreover, the fact that ^{17}O has an even A number could introduce more instability and potentially higher fusion capacity.

Finally, $^{16}O + {}^{16}O$ data is visualized in Figure 4.6a. As it happened to the last two reactions, the values corresponding to the S-factor are fitted better at energies below the Coulomb barrier with the empirical fit determined in this work and at energies above the barrier with the Yakovlev and collaborators potential model and empirical formula. Particularly, an entry with theoretical perdition with São Paulo data was included in order to illustrate the closeness of the cited papers results to this theoretical calculation.

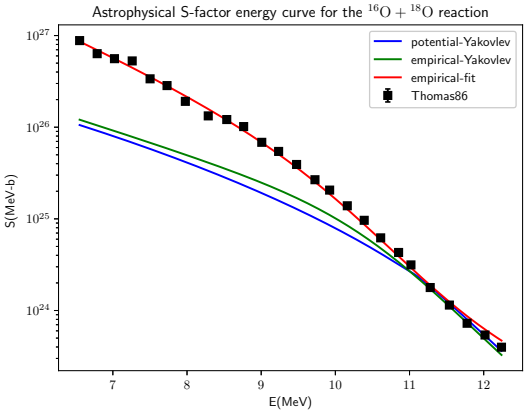

(a) $^{16}O + ^{18}O$ reaction.

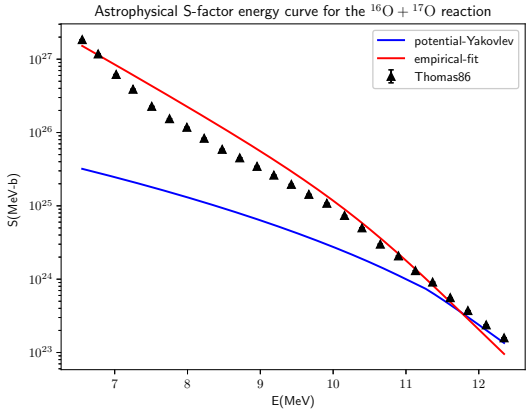

(b) $^{16}O + ^{17}O$ reaction.

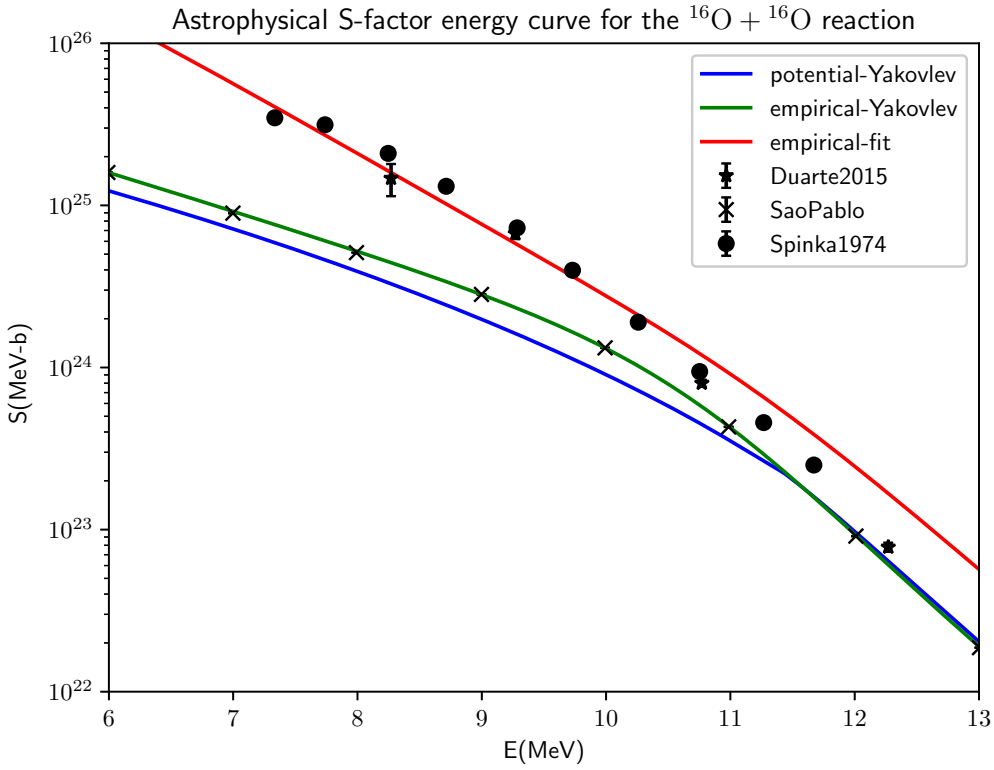

(c) $^{16}O + ^{16}O$ reaction.

Figure 4.6: Potential model prediction for a selection of oxygen fusion reactions. In panels a), b) and c) are presented the Yakovlev et. al prediction for the S-factor, as well as empirical two empirical fittings, of the $^{16}O + ^{18}O$, $^{16}O + ^{17}O$ and $^{16}O + ^{16}O$ reactions respectively. Additionally, in panel c), the *SaoPablo* entry corresponds with the predictions made in [123] which were obtained by using the São Paulo potential model. Experimental data sources are cited in Table A.3.Values of empirical fits parameters are given in Tables C.11, C.12 and C.13.

4.2 Resonant reactions

It is frequent to find sharp peaks in the S-factor values of some nuclear reactions. The existence of these fluctuations usually suggests the presence of resonant phenomena, which cannot be explained effectively with only background estimation.

In this work, the radiative capture $^{7}\mathrm{Be}(\mathrm{p},\gamma)^{8}\mathrm{B}$ and $^{13}\mathrm{C}(\mathrm{p},\gamma)^{14}\mathrm{N}$ reactions were selected. The first reaction has astrophysical relevance since it produces a tripe-alpha nuclei like ^{8}B [28]. The second reaction is essential in the CNO and hot CNO cycles [29].

A first approach towards the description of resonances consists of introducing a Breit-Wigner (BW) term in the S-factor calculation. In particular, the most simple estimation is given by assuming that the reaction proceeds with a single channel. Then, the astrophysical S-factor can be approximated as the expression given in equation 3.8.

In particular, each peak is characterized by additional variables like its height, width and energy center, which are referred as S_0, Γ_r and E_r respectively. With this new variables taken into account, the non-resonant astrophysical S-factor predictions of section 4.1 shall be modified.

Usually, more sophisticated treatments of resonances require more advanced approaches than bare curve fitting. For instance, the S-factor values of several radiative capture reactions can be analyzed by using the R-matrix model [159]. The main advantage of this approach is that resonances are intuitively included by adding parameters to the model.

4.2.1 Calculation considerations

The Breit-Wigner empirical formula is used for empirical fitting of the resonant part. However, not all the regions of S-factor energy curve for a reaction with resonances are going to coincide with resonant behavior. In contrast, these regions are critical in order to estimate the non-resonant background of the reaction.

For the purpose of this work, there are two methods for estimating this background. The first method consist of fitting a polynomial or exponential function to data including the whole dataset. This is specially convenient when resonances are narrow as compared to the total energy range like it happens in the $^{7}\mathrm{Be}(\mathrm{p},\gamma)^{8}\mathrm{B}$ reaction.

On the other hand, when a resonance occupies almost all the energy range, it is better to fit the Breit-Wigner function first. Then, residuals, which are the differences between predictions and experimental values, are calculated. Ultimately, the background estimation is given by fitting the remaining residuals of the fit. An example of this approach is given in the study of the $^{13}\mathrm{C}(\mathrm{p},\gamma)^{14}\mathrm{N}$ reaction.

On both cases, the total S-factor is computed by summing the resonant and non-resonant contributions. This sum is consistent since the S-factor is proportional to the cross section, which are allowed to be summed.

Finally, for the special case of estimating the background of the reactions with polynomial functions, it is usually convenient to modify slightly the Breit-Wigner fitting function. In particular, an extra parameter c related to the width is included. Then, the resonant contribution of equation 3.8 is substituted with the expression [108]:

$$S(E) = S_0 \frac{c_r}{(E - E_r)^2 + \Gamma_r^2/4}. \tag{4.7}$$

4.2.2 Results and analysis

Estimation for background and resonant contributions for the $^7\mathrm{Be}(\mathrm{p},\gamma)^8\mathrm{B}$ reaction are visualized in Figure 4.7.

In particular, in Figures 4.7a and 4.7b the polynomial and exponential background estimations, which were calculated in this work, are illustrated. Notice that, in contrast to the general tendency about fitting improvement with order increase reported in section 4.1.2, fits with higher order present a rather nonphysical behavior at higher energies. In fact, the best fits are those with $N = 1, 2$.

This difference can be also contrasted in the high values of most the errors of the parameters as N increases, as it is shown in Tables C.8 and C.7. In particular, the curves with $N = 4$ for both exponential and polynomial formulas were too deviated from S-factor data that the fitting algorithm was unable to determine errors for the parameters.

This finding could be explained by considering the effect of parameter overdetermination. In particular, since low order fits are ideal enough, a further increment in the degrees of freedom of the fitting function will cause conflicts between already well determined parameters and new parameters which have a higher contribution at larger energies.

Therefore, for the sake of simplicity, the selected background estimations for the $^7\mathrm{Be}(\mathrm{p},\gamma)^8\mathrm{B}$ reaction are those related with $N = 1$ order fitting formulas as it is visualized in Figure 4.7c.

Actually, a fine splitting is observed between the exponential and polynomial fits. In particular, the exponential contribution presents slightly higher values than those calculated from the polynomial contribution. Although at this range of energies this discrepancy might not be considered as substantial, this could be of interest when extrapolating S-factor data to larger energies. In particular, it seems more plausible that the exponential fit would extrapolate better than the polynomial fit when considering the SC06 entry point at $E \approx 3.0\mathrm{MeV}$.

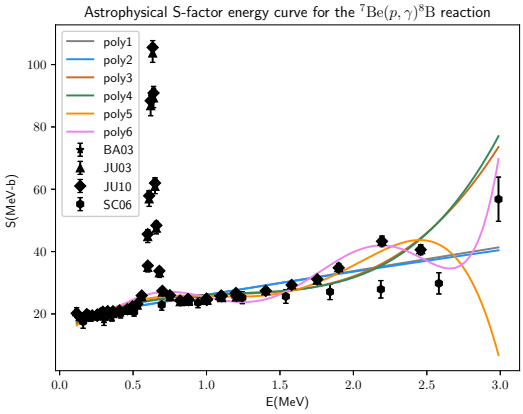

(a) Polynomial fits.

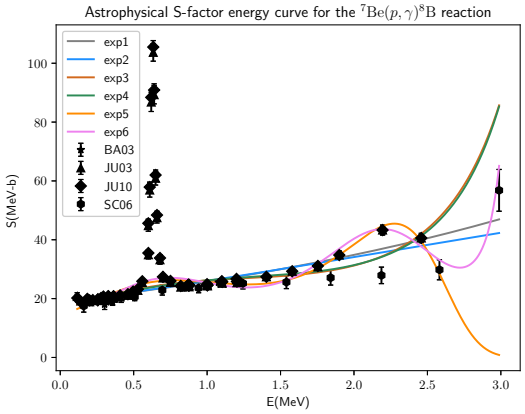

(b) Exponential fits.

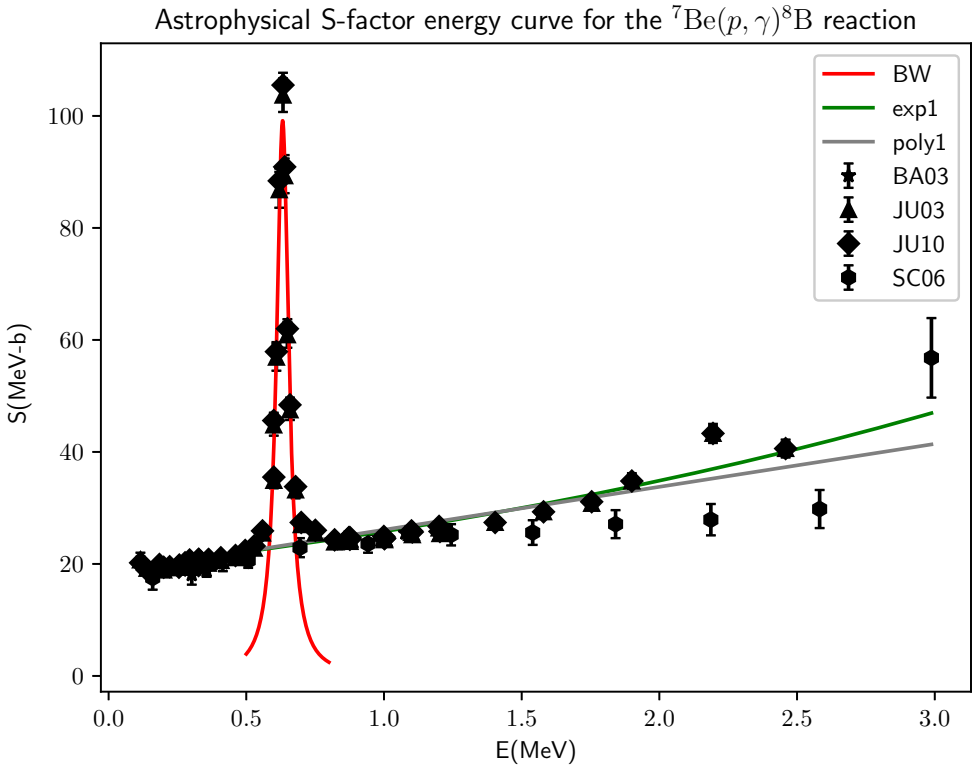

(c) Selected fits.

Figure 4.7: Empirical formulas fitted to background of the S-factor for the ^{7}Be(p,γ)^{8}B reaction. In panels a) and b) polynomial and exponential fits up to sixth order are presented respectively. Additionally, in panel c), the most simple and accurate fits, in this case exp1 and poly1, were selected. In addition, the BW labeled curve corresponds to a Breit-Wigner fit for the resonance. The references to the experimental points are given in Table A.2. The values of the fitting parameters are found in Tables C.7, C.8 and C.14.

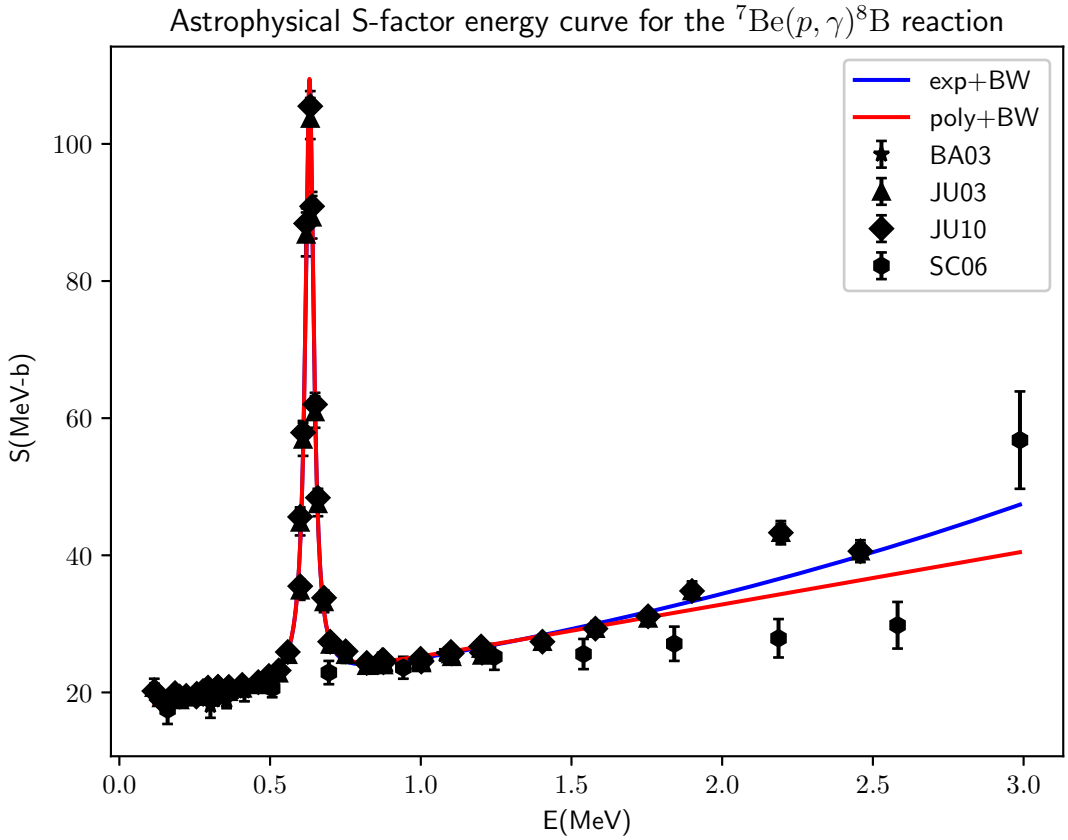

Figure 4.8: Empirical fit for the ^{7}Be(p,γ)^{8}B reaction. In this graph, the resonant contribution, as modeled with a Breit-Wigner, was added to the non-resonant background estimation, which was modeled with first order polynomial and exponential formulas. In addition, fitting parameters are found in Table C.15.

A single resonance with a peak close to $E \approx 0.7$ MeV is observed in Figure 4.8. Then, in order to describe the single resonance, a Breit-Wigner fit was performed. In particular, the fitting parameters are given in Table C.14.

However, as it is visualized in S-factor dependence, this fit does not account for the entire behavior of the experimental points far from the resonance. Consequently, there is the need of including the non-resonant part which was previously calculated.

Lastly, with both the resonant and non-resonant parts considered, it is possible to plot a single function estimation of the ^{7}Be(p,γ)^{8}B S-factor as it is presented in Figure 4.9. In order to achieve the result presented, it was needed to slightly adjust some of the parameters for the non-resonant and resonant formulas before the sum. The final values determined in this work for the resonant and non-resonant parameters are tabulated in Table C.15.

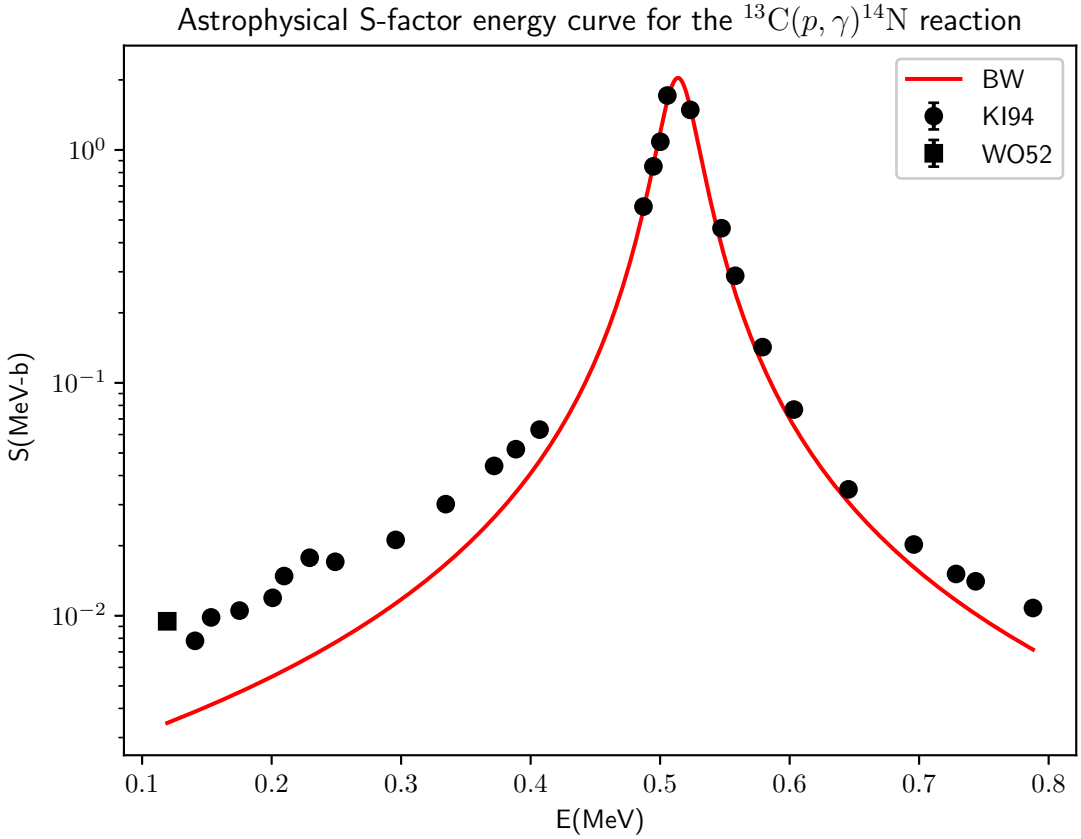

Figure 4.9: Breit-Wigner fit for the S-factor of the resonant $^{13}C(p,\gamma)^{14}N$ reaction. The experimental data points were taken from sources cited in Table A.2. Further details about the fitting parameters and their values are given in Table C.16.

On the other hand, with respect to the S-factor of the $^{13}C(p,\gamma)^{14}N$ reaction, a resonance with a peak close to $E \approx 0.6$ MeV is observed in Figure 4.9. Then, a Breit-Wigner fit was initially calculated.

Despite the global correspondence between the experimental data and the predictions of the fit, the resonant behavior does not entirely explain the shape of the S-factor data. This discrepancy specially occurs far from the resonance peak at low energies. In order to improve the prediction, the non-resonant contribution to the S-factor needs to be included.

In a first approach, the non-resonant background was estimated empirically with the residuals of the BW fitting In particular, the polynomial and exponential expansion was used as it is illustrated in Figures 4.10a and 4.10b with polynomial and exponential fits respectively.

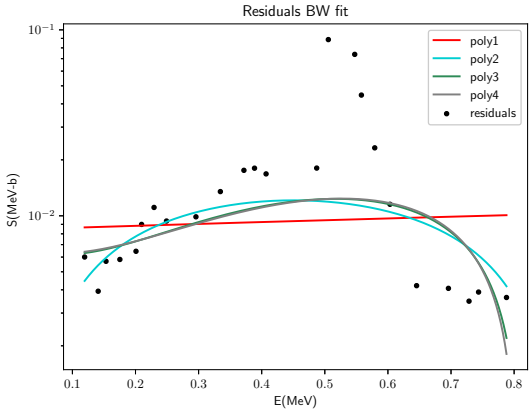

(a) Polynomial fits.

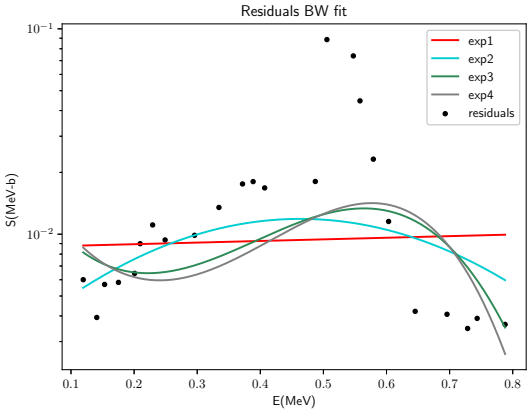

(b) Exponential fits.

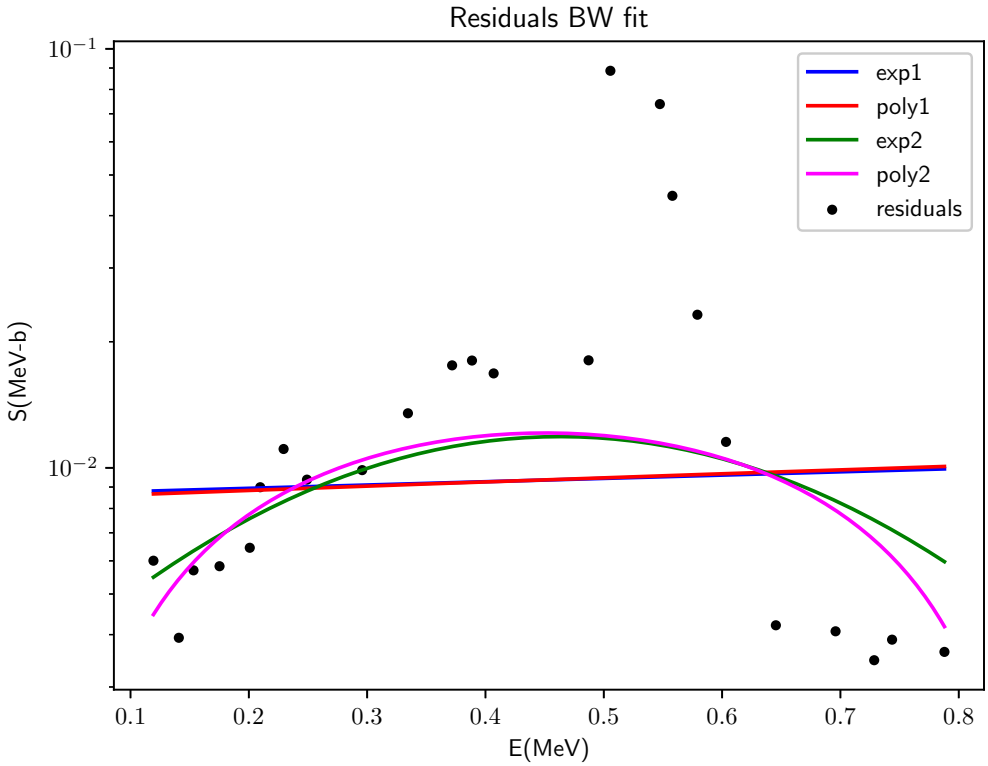

(c) Selected fits.

Figure 4.10: Empirical formulas fitted to background of the S-factor for the $^{13}C(p,\gamma)^{14}N$ reaction. The background was quantified with the residuals of the Breit-Wigner fit of Figure 4.9. he values of the fitting parameters are found in Tables C.17 and C.18.

In order to avoid unrealistic physical behavior, only fits with orders up to $N = 2$ were selected as it is shown in Figure 4.10c. In particular, it is visualized that the fits do not entirely account for the discrepancies between data and the BW fit. This suggests that the initial assumption of a single channel contribution for

the resonance has limitations in predicting the S-factor of the $^{13}C(p,\gamma)^{14}N$ reaction.

The last observation is supported correspondence by comparing the joint resonant and non-resonant prediction with experimental data, both found in Figure 4.11. Even though the S-factor estimation improved at low energies, new fits actually overestimate the S-factor for entries with energies above the resonance peak. Additionally, the poly2 + BW fit has an unphysical stepping descent at low energies.

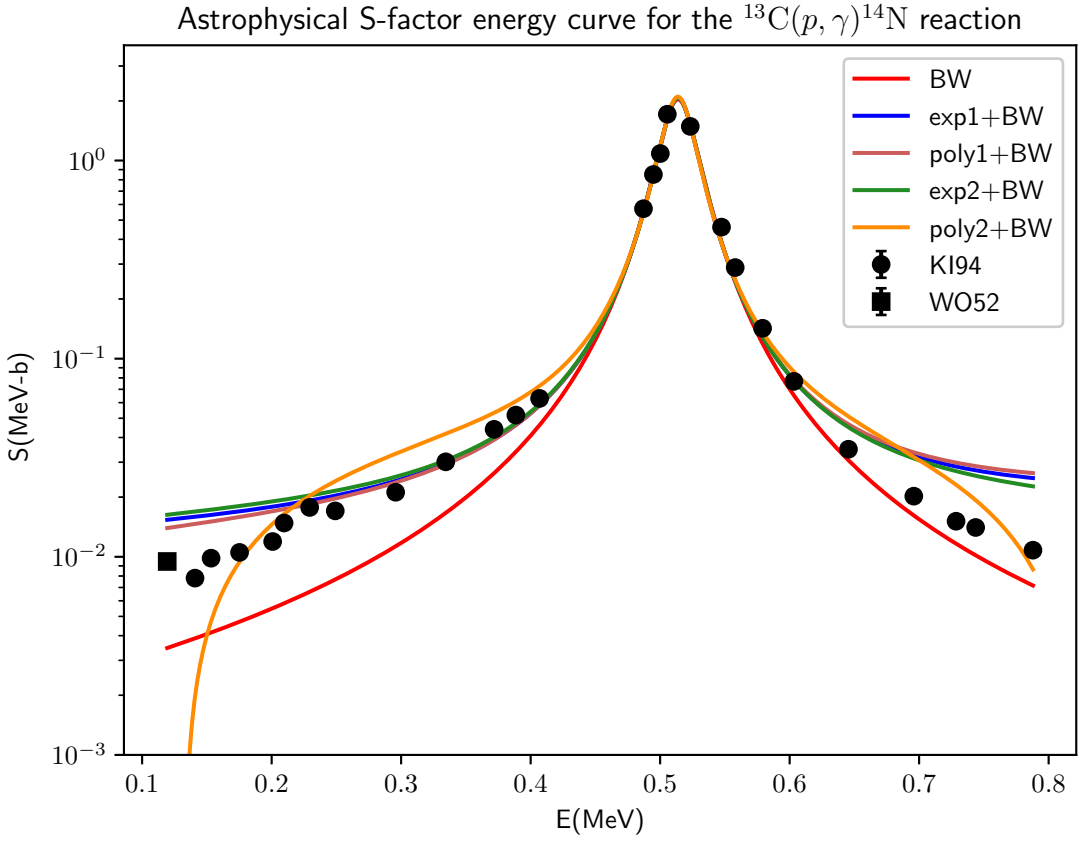

Figure 4.11: Empirical fit for the S-factor of the resonant $^{13}C(p,\gamma)^{14}N$ reaction. The resonant part was estimated with a Breit-Wigner fit added to a non-resonant background, which was fitted with exponential and polynomial with first and second order formulas. All the values of the parameters used are found in Table C.19.

This overall difference between S-factor experimental data and the prediction of the empirical formulas could be explained due to particularities of the physical phenomena underlying the $^{13}C(p,\gamma)^{14}N$ reaction. In fact, the S-factor values presented in Figure 4.9 corresponds to the sum of different channels associated with non-excited and excited states of ^{14}N [12]. This means that the theoretical prediction should consider the transitions to all possible states of the reactants and product nuclei.

Chapter 5

Conclusions

Astrophysical S-factors were calculated for the selected reactions and compared with available experimental data.

Nuclear physics of stars. Christian Iliadis.

Cauldrons in the cosmos. Claus Rolfs.

Hyde and Basdevant Nuclear physics.

Appendix A

Literature selected data

A.1 General data of nuclei

In this section general data about the structure of the nuclei will be presented.
EXFOR [160].
JENDL (Japanese Evaluated Nuclear Data Library) [4].

A.1.1 Selected constants

NIST selected constants and conversion factors to convenient units.

The units used for calculations are those suitable for calculations of astrophysical S-factors. In particular, the unit of energy is given in mega-electronvolts (MeV), and the distances between nuclei are given in fentometers (fm), and the cross sections in barns ($1\text{b} = 10^{-28}\text{cm}$). Therefore, various fundamental constant are converted to consistent units with respect to the mentioned convention as shown in the next table.

Some constants to be considered: c, h, $\hbar$, m_e, m_p, m_n.

In the units to be used for nuclear physics calculations: $4\pi\epsilon_0 = 1$. So, the fine structure constant is expressed as:

$$\alpha = \frac{e^2}{\hbar c}. \tag{A.1}$$

Therefore, the elementary charge is given by:

$$e = \sqrt{\alpha\hbar c} \approx \sqrt{1.41...}\sqrt{\text{MeV fm}}. \tag{A.2}$$

Masses can be expressed in terms of MeV/c^2 or MeV fm^{-2} s^2 depending on the context.

A.1.2 Nuclei structure data

atomic, massic, mass excess, spin, charge, data. L^π.

A.2 Astrophysical S-factor data

In this section, the reference to the experimental data on astrophysical S-factors for the selected reactions will be presented. In particular, the II database was widely used for reactions with $A < 10$. On the other hand, for reactions with $A > 10$, more specific references were used to obtain the experimental data.

Additional, light heavy experimental data pd reaction [161] and 2H proton capture c[162] and He3 photo-disintegration [163] with [164]

A.2.1 Nacre II database

The experimental data for a wide selection of radiative capture and exchange reactions at low energies is found in the Nacre II database [12]. This database serves as a compilation of data obtained form various experiments for the relevant reactions. In addition, in this paper a potential model calculation for each reaction is also included.

In the following tables, the references to the papers form which experimental data was obtained form this work will be presented.

Light nuclei reactions

Name	Reference	Reaction
GR85	[165]	$^{2}\mathrm{H(d,p)^{3}H}$
KR87a	[166]	
LE06a	[167]	
RA02	[26]	
SC72	[168]	
TU11	[169]	
CA02	[170]	$^{2}\mathrm{H(p,\gamma)^{3}He}$
FE65	[171]	
GE67	[172]	
GR62	[173]	
MA97	[174]	
SC96	[175]	
WA63	[164]	
WO67	[176]	

Table A.1: Experimental data references for a selection of non-resonant light heavy nuclei reactions. This table includes data corresponding to the $^{2}\mathrm{H(d,p)^{3}H}$ and $^{2}\mathrm{H(p,\gamma)^{3}He}$ reactions.

Resonant reactions

Name	Reference	Reaction
BA03	[177]	$^{7}\mathrm{Be(p,\gamma)^{8}B}$
JU03	[178]	
JU10	[179]	
SC06	[180]	
KI94	[181]	$^{13}\mathrm{C(p,\gamma)^{14}N}$
WO52	[182]	

Table A.2: Experimental data references for a selection of resonant reactions. This table includes data corresponding to the $^{7}\mathrm{Be(p,\gamma)^{8}B}$ and $^{13}\mathrm{C(p,\gamma)^{14}N}$ reactions.

A.2.2 Middle heavy nuclei data

Selected reaction reference table for the $^{12}\mathrm{C}+{}^{12}\mathrm{C}$, $^{12}\mathrm{C}+{}^{16}\mathrm{O}$, $^{16}\mathrm{O}+{}^{16}\mathrm{O}$, $^{13}\mathrm{C}+{}^{13}\mathrm{C}$ reactions.
$^{12}\mathrm{C}+{}^{12}\mathrm{C}$ reaction.

Name	Reference	Reaction
Becker1981	[183]	$^{12}C + ^{12}C$
Fruet2020	[184]	
Spillane2007	[185]	
Tan2002	[186]	
Torilov21	[51]	$^{12}C + ^{16}O$
Thomas86	[48]	$^{16}O + ^{18}O$
		$^{16}O + ^{17}O$
Duarte2015	[46]	$^{16}O + ^{16}O$
Spinka1974	[187]	

Table A.3: Experimental data citations for a selection of oxygen and carbon fusion reactions.

A.3 Resonances and transitions

Resonant specific data will be presented. In particular, for those reactions with the aviable information, the experimental peak as well as the reaction peak will be detailed. Additionally, with special observance on the radiative capture reactions, the transitions will be specified.
Data on the resonant 7Be + p and experimental methods [188].

A.3.1 Resonance data

Selection reaction reference list.

A.3.2 Transitions data

Transition type data, energy levels, energy peak and widths.

A.4 Fitting parameters

The fitting parameters in a selected list of articles will be presented. In particular, this section distinguish between specific model parameters, like empirical, potential or microscopical models, and R-matrix fitting, whose special calculation considerations will be detailed.

A.4.1 Specific model parameters

Tables of models and parameters, with uncertainties.

A.4.2 R-matrix parameters

Tables of parameters that were chosen for the selected reactions

Appendix B

Special functions

In this section will be encountered special functions to be used in scattering theory and solution of analytical equations.

B.1 Bessel functions

Differential equation, solutions, 1st and 2nd kind and some useful properties. There are standard and spherical Bessel functions.

The spherical functions are solutions for the differential equation:

$$\frac{d^2x}{d\rho^2} + 2\rho\frac{dx}{d\rho} + (\rho^2 - l(l+1))x = 0. \tag{B.1}$$

In particular, the solutions $J_l(\rho)$ and $Y_l(\rho)$ are called the Bessel and Von-Neumann solutions. One difference between these solutions is that $J_l(\rho)$ is well defined while $Y_l(\rho)$ has a pole at that $\rho = 0$.

In addition, the asymptotic behavior when $\rho \to \infty$ is different for each function as shown:

$$J_l(\rho) \to \sqrt{\frac{2}{\pi\rho}} \cos\left(\rho - \frac{\pi}{4} - \frac{l\pi}{2}\right). \tag{B.2}$$

and

$$Y_l(\rho) \to \sqrt{\frac{2}{\pi\rho}} \sin\left(\rho - \frac{\pi}{4} - \frac{l\pi}{2}\right). \tag{B.3}$$

B.2 Coulomb functions

Differential equations, solutions and more properties.

$$\frac{d^2x}{d\rho^2} + (\rho^2 - 2\eta\rho - l(l+1))x = 0. \tag{B.4}$$

There are two solutions for this equations. In the context of scattering theory, the solutions $F_{l\eta}(\rho)$ and $G_{l\eta}(\rho)$ are analogous to the $J_l(\rho)$ and $Y_l(\rho)$ solutions of the Bessel differential equation respectively.

The formulas are connected as [189].

$$G_{l\eta} = \frac{F_{l\eta} - iF_{-l\eta}}{2i}. \tag{B.5}$$

In a similar way than the Bessel functions, the Coulomb functions have harmonic like asymptotic behavior. In particular, $F_{l\eta} \to \sin\theta_{l\eta}$ and $G_{l\eta} \to \cos\theta_{l\eta}$ with $\theta_{l\eta}$ defined as:

$$\theta_{l\eta}(\rho) = \rho - l\frac{\pi}{2} - \eta\ln(2\rho) + \arg\Gamma(l+1+i\eta). \tag{B.6}$$

B.3 Additional selected functions

Hypergeometric equations and connection with coulomb functions with implementation.

Spherical harmonics and Legendre polynomials for the expansions used in scattering theory. Hyperspherical harmonics

B.4 Clebsch-Gordan coefficients

Motivation, definition and some computations. Generalization to further spins and couplings that are useful for determining effects like the spin-orbit coupling.

The total angular momentum and change of basis.
Tensor products are reported as to be useful in describing generalized sums and products. For instance, the direct product is expressed.

$$a \otimes b. \tag{B.7}$$

On the other hand, the direct sum is given by:

$$a \oplus b. \tag{B.8}$$

A convenient application of the last operations is encountered within the framework of addition of angular momenta is given by the expression:

$$j_1 \oplus j_2 = j_1 \otimes 1 \oplus 1 \otimes j_2. \tag{B.9}$$

Then, the added angular momentum assumes a representation in a higher dimension.
In addition, Clebsh-Gordan coefficients appear connected with expressions where spherical harmonics are included. For instance, the integral of a triple product of these special functions can be expressed as:

$$\int Y_l^m Y_{l'}^{m'} Y_{l''}^{m''} d\Omega d\Omega' d\Omega'' = \begin{pmatrix} s & l & I_x \\ j_s & j & J \end{pmatrix} \begin{pmatrix} s & l & I_x \\ j_s & j & J \end{pmatrix}. \tag{B.10}$$

Wigner symbols are introduced for expressing recurrent expressions involving Clebsh-Gordan coefficients. There are two types of such numbers: the $3j$ and the $6j$ Wigner numbers.

The $3j$ number is related to a single Clebsh-Gordan coefficient as it is useful for the addition of two angular momentum operators. The definition has the form:

$$\begin{pmatrix} s & l & I_x \\ j_s & j & J \end{pmatrix} = \frac{(-1)^{J-j_s-I_x}}{\sqrt{2l+1}} \langle s l j_s j | I_x J \rangle. \tag{B.11}$$

On the other hand, the $6j$ number is related to multiple Clebsh-Gordan coefficients. In fact, this coefficient is convenient when there are three angular momentum operators adding and when a change of sub coupling is needed.

$$\left\{ \begin{array}{ccc} s & l & I_x \\ j_s & j & J \end{array} \right\} = (-1)^{J-j_s-I_x} \langle s(lj_s)J|(sl)j_sJ\rangle. \tag{B.12}$$

B.5 Microscopic model functions

Those relevant microscopic model methods. Specially, those that account for cluster model and effective field theory models.

Hamiltonians and Lagrangians of related field theories.

Appendix C

Fitting

This section is about fitting considerations on the different approaches used to calculate the astrophysical S-factor.

C.1 Calculation procedures

Least square minimization of the quantity shown in equation C.1.

$$\chi^2 = \sum_{k=1}^{N} \frac{(x_k - \bar{x})^2}{\sigma_k^2}, \tag{C.1}$$

where k is an index running through all N of the sample points, x_k is the value, σ_k is the error of each point and $\bar{x}$ corresponds to the average of the value taken from all points.

There are two process depending if the optimization is bounded or unbounded.

C.1.1 Unconstrained fitting

Leavenberg-Marquardt algorithms [190] gradient descent and Newton method like for searching This model has a damping parameter. More recently (focused on computational implementations) [191].

C.1.2 Constrained fitting

Trust region reflective algorithm with computational implementation [192] and more theory with illustrations on reflective line search [193].

C.2 Empirical formulas fitting

Parameter list with uncertainty for its respective formula.

Units for the fitting parameters related with exponential and polynomial fits.

Label	g_0	g_1	g_2	g_3	g_4	g_5	g_6
poly	MeV b	b	MeV^{-1} b	MeV^{-2} b	MeV^{-3} b	MeV^{-4} b	MeV^{-5} b
exp		MeV^{-1}	MeV^{-2}	MeV^{-3}	MeV^{-4}	MeV^{-5}	MeV^{-6}

Table C.1: Units of the exponential and polynomial parameters.

Polynomial. ^{2}H(d, p)^{3}H reaction.

Label	g_0	g_1	g_2	g_3	g_4	g_5
poly1	0.0680 ± 0.0017	0.152 ± 0.0025				
poly2	0.0627 ± 0.0016	0.193 ± 0.0052	-0.0205 ± 0.0023			
poly3	0.0613 ± 0.0016	0.218 ± 0.011	-0.0523 ± 0.013	0.00847 ± 0.0034		
poly4	0.0615	0.212	-0.0401	0.00128	1.000	
poly5	0.0622 ± 0.0018	0.173 ± 0.032	0.116 ± 0.094	-0.189 ± 0.097	0.0886 ± 0.040	-0.0133 ± 0.0058
poly5-exclude	0.0554 ± 0.0013	0.254 ± 0.015	-0.0827 ± 0.041	-0.00712 ± 0.042	0.0197 ± 0.017	-0.00417 ± 0.0024

Table C.2: Fitting parameters of the polynomial fits, presented in Figures 4.1a and 4.1c, of the ^{2}H(d, p)^{3}H reaction.

Exponential

Label	g_0	g_1	g_2	g_3	g_4	g_5
exp1	0.0929 ± 0.003	0.622 ± 0.019				
exp2	0.0724 ± 0.0018	1.397 ± 0.039	-0.271 ± 0.013			
exp3	0.066 ± 0.0016	2.028 ± 0.075	-0.888 ± 0.066	0.145 ± 0.015		
exp4	0.0674	1.847	-0.623	0.0191	1.000	
exp5	-2.789 ± 0.026	3.011 ± 0.22	-2.818 ± 0.51	1.495 ± 0.46	-0.384 ± 0.17	0.459 ± 0.023

Table C.3: Fitting parameters of the exponential fits, presented in Figure 4.1b, of the ^{2}H(d, p)^{3}H reaction.

Screening with poly5-exclude

Label	Comment	U_e(eV)
screening-all-fit	Fitting	100.0 ± 8.6
screening-only-RA02-fit	Fitting with only RA02 data included	230.7 ± 9.2
screening-Ue-theory	Calculation with RA02 U_e value	309 ± 12 [26]
RA02-paper	Prediction RA02 paper	

Table C.4: Screening effect parameter U_e values related to ^{2}H(d, p)^{3}H reaction fits presented in Figure 4.2. In the RA02-paper curve a poly1 for background estimation was used with parameters $g_0 = 0.0043 \pm 0.0001$ MeV b and $g_1 = 0.54 \pm 0.05$ b [26].

Polynomial.

Label	g_0	g_1	g_2	g_3	g_4	g_5
poly1-c	1.0 ± 1.5	10.00 ± 0.43				
poly2-c	1.0 ± 1.2	10.00 ± 0.93	0.309 ± 0.11			
poly3-c	0.0342 ± 1.1	10.0 ± 1.8	1.011 ± 0.55	-0.0839 ± 0.043		
poly4-c	0.253 ± 1.1	4.712 ± 3.30	4.803 ± 1.9	-0.830 ± 0.34	0.0432 ± 0.019	
poly5-c	0.434 ± 1.2	1.389 ± 5.96	7.980 ± 5.1	-1.829 ± 1.5	0.169 ± 0.19	-0.00547 ± 0.0081

Table C.5: Fitting parameters polynomial fits, shown in Figure 4.3a, ^{2}H(p, γ)^{3}He reaction.

Exponential

Label	g_0	g_1	g_2	g_3	g_4	g_5
exp1	12.958 ± 1.4	0.250 ± 0.014				
exp2	6.165 ± 0.86	0.649 ± 0.047	-0.0367 ± 0.038			
exp3	2.754 ± 0.64	1.334 ± 0.14	-0.181 ± 0.025	0.00865 ± 0.0014		
exp4	0.311 ± 0.45	2.116 ± 0.39	-0.447 ± 0.12	0.0439 ± 0.014	-0.00159 ± 0.00063	
exp5	0.315 ± 0.62	2.109 ± 0.73	-0.444 ± 0.33	0.0431 ± 0.067	-0.00151 ± 0.0064	-0.000294 ± 0.00023

Table C.6: Fitting parameters exponential fits, shown in Figure 4.3b, related to the ^{2}H(p, γ)^{3}He reaction.

Polynomial. ^{7}Be(p, γ)^{8}B reaction. Non-resonant background.

Label	g_0	g_1	g_2	g_3	g_4	g_5	g_6
poly1	18.429 ± 0.86	7.668 ± 1.1					
poly2	18.316 ± 1.3	8.042 ± 3.3	-0.217 ± 1.8				
poly3	13.868 ± 2.3	29.490 ± 10.0	-24.403 ± 10.8	7.101 ± 3.1			
poly4	15.075	22.690	-13.835	1.106	0.000		
poly5	13.219 ± 5.4	27.594 ± 35.8	-0.187 ± 79.8	-35.841 ± 78.3	26.055 ± 34.3	-5.072 ± 5.4	
poly6	27.181 ± 7.7	-103.057 ± 63.1	419.070 ± 185.7	-631.656 ± 251.3	435.745 ± 167.9	-138.269 ± 53.8	16.382 ± 6.6

Table C.7: Parameters polynomial fits, included in Figure 4.7a, corresponding to ^{7}Be(p, γ)^{8}B reaction.

Exponential

Label	g_0	g_1	g_2	g_3	g_4	g_5	g_6
exp1	19.091 ± 0.71	0.301 ± 0.042					
exp2	18.731 ± 1.1	0.356 ± 0.13	-0.0278 ± 0.060				
exp3	16.162 ± 1.5	1.024 ± 0.36	-0.734 ± 0.36	0.194 ± 0.096			
exp4	16.985	0.770	-0.388	0.0261	0.000		
exp5	2.645 ± 0.29	1.355 ± 1.9	0.295 ± 4.3	-2.425 ± 4.2	1.720 ± 1.9	-0.344 ± 0.30	
exp6	3.071 ± 0.36	-2.499 ± 2.7	12.451 ± 7.5	-19.720 ± 9.6	13.799 ± 6.1	-4.382 ± 1.9	0.516 ± 0.22

Table C.8: Parameters exponential fits, included in Figure 4.7b, associated with the $^{7}\mathrm{Be}(\mathrm{p},\gamma)^{8}\mathrm{B}$ reaction.

$^{12}\mathrm{C} + {}^{12}\mathrm{C}$ fusion reaction

Label	a_0	a_1	a_2	b_1	b_2	b_3	b_4	E_c(MeV)	D(MeV)
empirical -Yakovlev [149]	37.333	-0.4065	-0.0137	4.881	-1.1909	0.0418	0.00014	7.134	0.94
empirical -fit	36.623 ± 2.7	0.625 ± 1.8	-0.132 ± 0.28						

Table C.9: Parameters empirical formula, associated with Figure 4.4, for the $^{12}\mathrm{C} + {}^{12}\mathrm{C}$ reaction.

$^{12}\mathrm{C} + {}^{16}\mathrm{O}$ fusion reaction.

Label	a_0	a_1	a_2	b_1	b_2	b_3	b_4	E_c(MeV)	D(MeV)
empirical -Yakovlev [149]	47.541	-0.4158	-0.01195	7.454	-1.3683	0.04019	-0.000005	8.998	1.00
empirical -fit	47.717 ± 83.5	-0.294 ± 43.2	-0.01 ± 13.5	7.6	-1.299	0	-0.00001	8.9	0.99

Table C.10: Parameters empirical formula, associated with Figure 4.5, for the $^{12}\mathrm{C} + {}^{16}\mathrm{O}$ reaction.

$^{16}\mathrm{O} + {}^{18}\mathrm{O}$ fusion reaction.

Label	a_0	a_1	a_2	b_1	b_2	b_3	b_4	E_c(MeV)	D(MeV)
empirical -Yakovlev [149]	63.550	-0.4610	-0.01137	5.498	-0.2623	-0.05928	0.002232	10.871	0.89
empirical -fit	66.914 ± 541	-0.6 ± 214	-0.0223 ± 24.4	3.5	-0.25	-0.1	0.00679	10.86	0.90

Table C.11: Parameters empirical formula, associated with Figure 4.6a, for the $^{16}\mathrm{O} + {}^{18}\mathrm{O}$ reaction.

$^{16}\mathrm{O} + {}^{17}\mathrm{O}$ fusion reaction.

Label	a_0	a_1	a_2	b_1	b_2	b_3	b_4	E_c(MeV)	D(MeV)
empirical -fit	70.5	-1.110	-0.015	3.9	-0.16	-0.05	0.002	11.0	0.88

Table C.12: Parameters empirical formula, associated with Figure 4.6b, for the $^{16}\mathrm{O} + {}^{17}\mathrm{O}$ reaction.

$^{16}O + {}^{16}O$ fusion reaction.

Label	a_0	a_1	a_2	b_1	b_2	b_3	b_4	E_c(MeV)	D(MeV)
empirical -Yakovlev [149]	60.932	-0.4236	-0.01018	2.485	0.3363	-0.09320	0.002830	11.079	0.88
empirical -fit	64.9	-0.6085	-0.028	2.49	0.34	-0.079	0.003	10.9	0.89

Table C.13: Parameters empirical formula, associated with Figure 4.6c, for the $^{16}O + {}^{16}O$ reaction.

BW $^{7}Be(p,\gamma)^{8}B$

Label	S_r(MeV b)	E_r(MeV)	Γ_r(MeV)
BW	99.153 ± 4.9	0.632 ± 0.0010	0.0535 ± 0.0034

Table C.14: Fitting parameters to the Breit-Wigner function, shown in Figure 4.7c, for the $^{7}Be(p,\gamma)^{8}B$ reaction.

Composite $^{7}Be(p,\gamma)^{8}B$

Label	S_r(MeV b)	E_r(MeV)	Γ_r(MeV)	c_r(MeV^2)	g_0	g_1
exp + BW	87.097 ± 2.2	0.631 ± 0.00036	0.0335 ± 0.00095		17.935 ± 0.13	0.325 ± 0.0077
poly + BW	21.227	0.631 ± 0.00062	0.0331	0.00113	17.370 ± 0.20	7.725 ± 0.27

Table C.15: Fitting parameters for composite resonant and non-resonant behavior fits, as visualized in Figure 4.8, for the $^{7}Be(p,\gamma)^{8}B$ reaction.

BW $^{13}C(p,\gamma)^{14}N$

Label	S_r(MeV b)	E_r(MeV)	Γ_r(MeV)
BW	2.040 ± 0.059	0.514 ± 0.00026	0.0325 ± 0.0013

Table C.16: Fitting parameters Breit-Wigner fits, included in Figure 4.9, related to the $^{13}C(p,\gamma)^{14}N$ reaction.

Residuals polynomial fit $^{13}C(p,\gamma)^{14}N$ reaction.

Label	g_0	g_1	g_2	g_3	g_4
poly1	0.00841 ± 0.016	0.00211 ± 0.033			
poly2	-0.00204 ± 0.032	0.0628 ± 0.17	-0.0697 ± 0.19		
poly3	0.00694 ± 0.076	-0.0193 ± 0.65	0.135 ± 1.6	-0.150 ± 1.1	
poly4	0.00678	-0.0134	0.0943	-0.0606	1.000

Table C.17: Fitting parameters polynomial fit residuals, as visible in Figure 4.10a, for the $^{13}C(p,\gamma)^{14}N$ reaction.

Residuals exponential fit $^{13}C(p,\gamma)^{14}N$ reaction.

Label	g_0	g_1	g_2	g_3	g_4
exp1	0.00862 ± 0.015	0.181 ± 3.6			
exp2	0.00292 ± 0.013	6.049 ± 21.3	-6.526 ± 23.9		
exp3	0.0238 ± 0.23	-13.564 ± 83.3	42.626 ± 205.1	-36.166 ± 153.3	
exp4	0.0306	-15.084	39.610	-17.343	0.000

Table C.18: Fitting parameters exponential fit t residuals, as shown in Figure 4.10b, for the $^{13}C(p,\gamma)^{14}N$ reaction.

Composite $^{13}C(p,\gamma)^{14}N$

Label	S_r	E_r	Γ_r	c_r	g_0	g_1	g_2
exp1 + BW	2.056 ± 0.062	0.514 ± 0.00025	0.0314 ± 0.0014		0.0113 ± 0.014	0.612 ± 2.4	
poly1 + BW	2.057	0.514 ± 0.00026	0.0314	0.000247 ± 0.0014	0.00910 ± 0.017	0.0135 ± 0.037	
exp2 + BW	2.057 ± 0.063	0.514 ± 0.00026	0.0314 ± 0.0015		0.0117 ± 0.033	1.0 ± 15.1	-0.770 ± 16.3
poly2 + BW	2.041	0.514 ± 0.00025	0.031 ± 0.0015	0.000236	-0.037 ± 0.039	0.294 ± 0.22	-0.310 ± 0.24

Table C.19: Fitting parameters composite fits, included in Figure 4.11, corresponding to the $^{13}C(p,\gamma)^{14}N$ reaction.

C.3 Free parameters fitting on potential models

Parameter list, uncertainty and its respective formula.
São Paulo potential + Brazilian potential model + nuclear densities + phase shift data fits + computational implementation + optical models [194].

Woods-Saxon potential + two core shell model + spin orbit coupling + dynamical (adiabatic and non -adiabatic) coupling + computational implementation [195] .

C.4 Microscopic model fitting

Parameter list, uncertainty and its respective formula.
Double folding two spherical nuclei + modified (logarithmic Gross-Kalinowski profile) Woods-Saxon potential + computational implementation [196].

C.5 R-matrix fitting

Parameter list, uncertainty and its respective formula. Widths and channels.

Reaction	E_R(MeV)	Γ(MeV)	References
1	0.504	0.102	REF1
4	0.607	0.304	REF2

Table C.20: A new Table

Coupled channels R-matrix + Numerov algorithm computational implementation [197] ^{7}Be nucleus structure. General, phenomenological and simplified R-matrix theory + transformations + numerical implementation [198] AZURE R-matrix code + formalism + channels + transformations + analysis for selected reactions + single and multi channel [199]

Appendix D

Numerical integration and differential equation solving

In this section will be introduced the generalities of the numerical solution of integrals and differential equation that were used throughout the document. In particular, a special subsection on the numerical solution for the Schroödinger equation for scattering phenomena will be presented.

D.1 Integration of selected potentials

WKB numerical implementation based on the Gaussian quadrature algorithm.

D.2 Numerical solution of the Schrödinger equation

The numerical solution of the Schrödinger equation is found to be useful for the approaches where it is not possible to find a solution for the problem in closed form, mainly analytical solutions.
Schrodinger and Dirac equation numerical solver with central potentials [200]
Coupled channels (CCFULL code) + Woods-Saxon parametrization + boundary conditions specified + rotational, vibrational and transfer couplings [201].

D.2.1 Main approach

The different methods to be solved the Schroödinger equation and overall differential equation solving strategy.

D.2.2 Implementation of the potential functions

Different potential considerations.

D.2.3 Boundary conditions implementation

Expected boundary conditions at $r \to \infty$ and their numerical implementation.

Appendix E

Computer codes implementation

In this section is going to be presented the aspects related with the `sfactors` python module. The code related to this module is found in a public GitHub repository:

https://github.com/CarlosAlbertoCalvachiSalas/astrophysicalSfactors

E.1 Structure of the computer program

The full tree with the files with explanation of the detailed packages is presented in Figure E.1.

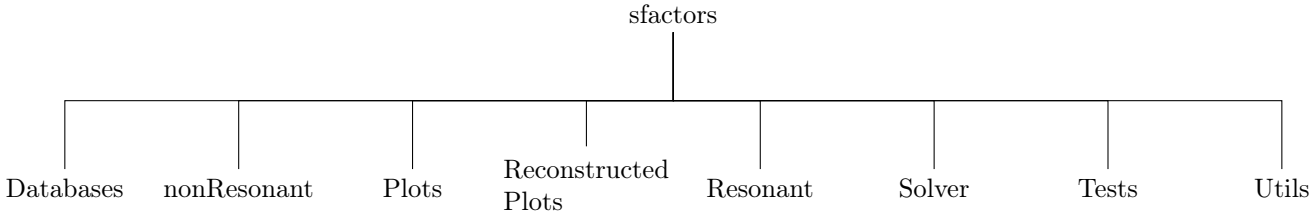

Figure E.1: Tree of the dependencies of the program (under elaboration)

E.2 User manual

In this section the user manual should be presented. This contains instructions regarding to installation, plotting and fitting. Also, in special cases, there are special kind of fittings related to models which are not empirical formulas. All these processes well behavior can be checked by executing prepared tests given by the program.

E.2.1 Installation

In this section a full installation sequence will be presented.

The first step consists of downloading the source code with the command:

```
git clone https://github.com/CarlosAlbertoCalvachiSalas/astrophysicalSfactor
```

Then, the FILE - PATH variable contained in the root file should be changed to the convenient path to be determined by the user.

E.2.2 Plotting

Plotting of S-factors.

E.2.3 Empirical fitting

Empirical fitting based on predetermined and custom functions.

E.2.4 Specific model fitting

Model fitting.

E.2.5 Model testing

Different tests of the program code.

E.3 Documentation

The description of the components of the package is going to be presented in the upcoming sections.

E.3.1 Databases

Contains all the databases used for calculations. Most of the files in this section are related with astrophysical S-factor data.

E.3.2 Non resonant

Subroutines for specific model functions are presented. The polynomial and exponential function to be fitted to light nuclei non-resonant reactions are within this folder. In addition, fusion reaction empirical formula given in [149] is also coded in this section of the code.

In addition, the files corresponding to Yakovlev et. al analytical potential model [123] calculations are contained in this section.

E.3.3 Resonant

The Breit-Wigner formula subroutine, as well as hybrid resonant and non-resonant subroutines, are coded in files within this folder.

E.3.4 Plots

The codes related to S-factor plotting are contained within this folder. In particular, when executing this program subroutines, experimental points, manual function, as well as fitted curves are plotted.

E.3.5 Reconstructed Plots

All the relevant graphs used in this work are contained in this folder with .eps extension. This format in convenient since it is convertible to .pdf and is also adequate for LaTeX implementation.

E.3.6 Solver

Model calculations files are saved in this folder. In particular, subroutines were created for implementing WKB approximation. Additionally, Coulomb functions are permitted to be calculated from functions contained in files included in this folder.

E.3.7 Tests

Some relevant tests concerning the functionality of the program are contained in this folder.

E.3.8 Utils

In order to make programming more handy, selected subroutines were added to the program. In particular, functions contained in files of this folder can create exp and poly fits, retrieve data from sources like the exact nuclear mass, as well as automatize processes regarding to the creation of graphs.

Bibliography

[1] J. L. Basdevant, J. Rich, and M. Spiro. *Fundamentals in nuclear physics: From nuclear structure to cosmology.* Springer Verlag New York, 2004.

[2] K. Heyde. *Basic ideas and concepts in nuclear physics: An introductory approach.* CRC Press, 2020.

[3] C. Iliadis. *Nuclear physics of stars.* Wiley-VCH, 2015.

[4] O. Iwamoto, N. Iwamoto, K. Shibata, A. Ichihara, S. Kunieda, F. Minato, and S. Nakayama. Status of JENDL. *EPJ Web of Conferences*, 239:09002, 2020.

[5] R. Dick. *Advanced Quantum Mechanics: Materials and photons.* Springer, 2016.

[6] C. J. Joachain. *Quantum collision theory.* North-Holland Pub. Co., 1983.

[7] R. G. Newton. *Quantum Physics: A Text for Graduate Students.* Graduate Texts in Contemporary Physics. Springer, 2002.

[8] H. Sasaki, T. Kawano, and I. Stetcu. Noniterative finite amplitude methods for $E1$ and $M1$ giant resonances. *Physical Review C*, 105(4), 2022.

[9] D. T. Tran, H. J. Ong, G. Hagen, T. D. Morris, N. Aoi, T. Suzuki, Y. Kanada-En'yo, L. S. Geng, S. Terashima, I. Tanihata, and et al. Evidence for prevalent $Z = 6$ magic number in neutron-rich carbon isotopes. *Nature Communications*, 9(1), 2018.

[10] C. A. Bertulani. Nuclear reactions. *digital Encyclopedia of Applied Physics*, page 45–92, 2003.

[11] C. R. Brune and B. Davids. Radiative capture reactions in astrophysics. *Annual Review of Nuclear and Particle Science*, 65(1):87–112, 2015.

[12] Y. Xu, K. Takahashi, S. Goriely, M. Arnould, M. Ohta, and H. Utsunomiya. NACRE II: an update of the NACRE compilation of charged-particle-induced thermonuclear reaction rates for nuclei with mass number $A < 16$. *Nuclear Physics A*, 918:61–169, 2013.

[13] T. R. Whitehead, T. Poxon-Pearson, F. M. Nunes, and G. Potel. Prediction for (p, n) charge-exchange reactions with uncertainty quantification. *Physical Review C*, 105(5), 2022.

[14] A. Sharma, A. Gandhi, and A. Kumar. Investigation of Weisskopf-Ewing approximation for the determination of (n, p) cross sections using the surrogate reaction technique. *Physical Review C*, 105(1), 2022.

[15] C. A. Bertulani and T. Kajino. Frontiers in nuclear astrophysics. *Progress in Particle and Nuclear Physics*, 89:56–100, 2016.

[16] P. Descouvemont. Nuclear reactions of astrophysical interest. *Frontiers in Astronomy and Space Sciences*, 7, 2020.

[17] A. Coc and E. Vangioni. Big-Bang Nucleosynthesis with updated nuclear data. *Journal of Physics: Conference Series*, 202:012001, 2010.

[18] C. Patrignani et. al (Particle Data Group). Review of Particle Physics. *Chinese Physics C*, 40(10):100001, 2016.

[19] R. V. Wagoner, W. A. Fowler, and F. Hoyle. On the Synthesis of Elements at Very High Temperatures. *The Astrophysical Journal*, 148:3, 1967.

[20] H. Su-Qing, W. Kai-Su, C. Yong-Shou, S. Neng-Chuan, and L. Zhi-Hong. The Main Path to C, N, O Elements in Big Bang Nucleosynthesis. *Chinese Physics Letters*, 27(8):082601, 2010.

[21] C. A. Bertulani. Big Bang Nucleosynthesis and the Lithium Problem. *Journal of Physics: Conference Series*, 1291(1):012002, 2019.

[22] E. Margaret Burbidge, G. R. Burbidge, W. A. Fowler, and F. Hoyle. Synthesis of the Elements in Stars. *Reviews of Modern Physics*, 29(4):547–650, 1957.

[23] W. Kundt. *Astrophysics: A New Approach*. Springer, 2005.

[24] A. A. Arsentieva and I. I. Shevchenko. Host Stars of Planets on the Hertzsprung–Russell Diagram. *Astronomy Letters*, 47(9):651–660, 2021.

[25] W. A. Fowler. Completion of the Proton-Proton Reaction Chain and the Possibility of Energetic Neutrino Emission by Hot Stars. *The Astrophysical Journal*, 127:551, 1958.

[26] F. Raiola, P. Migliardi, G. Gyürky, M. Aliotta, A. Formicola, R. Bonetti, C. Broggini, L. Campajola, P. Corvisiero, H. Costantini, and et al. Enhanced electron screening in d(d,p)t for deuterated Ta*. *The European Physical Journal A*, 13(3):377–382, 2002.

[27] H. J. Assenbaum, K. Langanke, and C. Rolfs. Effects of electron screening on low-energy fusion cross sections. *Zeitschrift für Physik A Atomic Nuclei*, 327(4):461–468, 1987.

[28] A. Coc. Variation of fundamental constants and the triple- alpha reaction in Population III stars and BBN. *Journal of Physics: Conference Series*, 337:012037, 2012.

[29] M. Wiescher, J. Görres, and H. Schatz. Break-out reactions from the CNO cycles. *Journal of Physics G: Nuclear and Particle Physics*, 25(6), 1999.

[30] F. Kaeppeler, M. Wiescher, U. Giesen, J. Goerres, I. Baraffe, M. El Eid, C. M. Raiteri, M. Busso, R. Gallino, M. Limongi, and et al. Reaction rates for $^{18}\mathrm{O}(\alpha,\gamma)^{22}\mathrm{Ne}$, $^{22}\mathrm{Ne}(\alpha,\gamma)^{26}\mathrm{Mg}$, and $^{22}\mathrm{Ne}(\alpha,\mathrm{n})^{25}\mathrm{Mg}$ in stellar helium burning and s-process nucleosynthesis in massive stars. *The Astrophysical Journal*, 437:396, 1994.

[31] G. Lotay, D. T. Doherty, R. V. Janssens, D. Seweryniak, H. M. Albers, S. Almaraz-Calderon, M. P. Carpenter, A. E. Champagne, C. J. Chiara, C. R. Hoffman, and et al. Revised decay properties of the key 93-keV resonance in the $^{25}\mathrm{Mg}(\mathrm{p},\gamma)$ reaction and its influence on the MgAl cycle in astrophysical environments. *Physical Review C*, 105(4), 2022.

[32] W. D. Arnett. Advanced evolution of massive stars. V - Neon burning. *The Astrophysical Journal*, 193:169, 1974.

[33] M. F. El Eid, B. S. Meyer, and L.-S. The. Evolution of Massive Stars Up to the End of Central Oxygen Burning. *The Astrophysical Journal*, 611(1):452–465, 2004.

[34] D. Bodansky, D. D. Clayton, and W. A. Fowler. Nucleosynthesis During Silicon Burning. *Physical Review Letters*, 20(4):161–164, 1968.

[35] M. Pignatari, R. Hirschi, M. Wiescher, R. Gallino, M. Bennett, M. Beard, C. Fryer, F. Herwig, G. Rockefeller, F. X. Timmes, and et al. The $^{12}C + ^{12}C$ reaction and the impact on nucleosynthesis in massive stars. *The Astrophysical Journal*, 762(1):31, 2012.

[36] A. Diaz-Torres and M. Wiescher. Characterizing the astrophysical S factor for $^{12}C + ^{12}C$ fusion with wave-packet dynamics. *Physical Review C*, 97(5), 2018.

[37] Y. J. Li, X. Fang, B. Bucher, K. A. Li, L. H. Ru, and X. D. Tang. Modified astrophysical S-factor of $^{12}C + ^{12}C$ fusion reaction at sub-barrier energies. *Chinese Physics C*, 44(11):115001, 2020.

[38] T.-P. Luo, P.-W. Wen, C.-J. Lin, L. Yang, H.-M. Jia, F. Yang, D.-H. Huang, C. Chang, M.-H. Zhang, Y. Yang, and et al. Bayesian analysis on non-resonant behavior of $^{12}C + ^{12}C$ fusion reaction at sub-barrier energies. *Chinese Physics C*, 46(6):064105, 2022.

[39] A. M. Mukhamedzhanov, D. Y. Pang, and A. S. Kadyrov. Astrophysical factors of $^{12}C + ^{12}C$ fusion extracted using the Trojan horse method. *Physical Review C*, 99(6), 2019.

[40] A. M. Mukhamedzanov. Status of deep subbarrier $^{12}C + ^{12}C$ fusion and advancing the Trojan horse method. *The European Physical Journal A*, 58(4), 2022.

[41] Y. Taniguchi and M. Kimura. $^{12}C + ^{12}C$ fusion S^*-factor from a full-microscopic nuclear model. *Physics Letters B*, 823:136790, 2021.

[42] M. Assunção and P. Descouvemont. $^{12}C + ^{12}C$ fusion in a multichannel folding model. *Journal of Physics: Conference Series*, 665:012010, 2016.

[43] F. Koyuncu and A. Soylu. Screening effects on $^{12}C + ^{12}C$ fusion reaction. *Chinese Physics C*, 42(5):054106, 2018.

[44] M. Notani, H. Esbensen, X. Fang, B. Bucher, P. Davies, C. L. Jiang, L. Lamm, C. J. Lin, C. Ma, E. Martin, and et al. Correlation between the $^{12}C + ^{12}C$, $^{12}C + ^{13}C$, and $^{13}C + ^{13}C$ fusion cross sections. *Physical Review C*, 85(1), 2012.

[45] N. T. Zhang, X. Y. Wang, D. Tudor, B. Bucher, I. Burducea, H. Chen, Z. J. Chen, D. Chesneanu, A. I. Chilug, L. R. Gasques, and et al. Constraining the $^{12}C + ^{12}C$ astrophysical S-factors with the $^{12}C + ^{13}C$ measurements at very low energies. *Physics Letters B*, 801:135170, 2020.

[46] J. G. Duarte, L. R. Gasques, J. R. Oliveira, V. A. Zagatto, L. C. Chamon, N. H. Medina, N. Added, W. A. Seale, J. A. Alcántara-Núñez, E. S. Rossi, and et al. Measurement of fusion cross sections for $^{16}O + ^{16}O$. *Journal of Physics G: Nuclear and Particle Physics*, 42(6):065102, 2015.

[47] A. Kuronen, J. Keinonen, and P. Tikkanen. Cross section of $^{16}O + ^{16}O$ near the Coulomb barrier. *Physical Review C*, 35(2):591–596, 1987.

[48] J. Thomas, Y. T. Chen, S. Hinds, D. Meredith, and M. Olson. Sub-barrier fusion of the oxygen isotopes: A more complete picture. *Physical Review C*, 33(5):1679–1689, 1986.

[49] L. Guimin, F. Deji, and C. Xiaowu. Sub-Barrier Fusion Coupled-Channels Calculations for $^{16}O + ^{16,18}O$. *Chinese Physics Letters*, 9(11):577–580, 1992.

[50] J. L. Ferreira, J. Lubian, R. Linares, M. J. Ermamatov, H. Yépez-Martínez, and P. O. Hess. Analysis of the alpha-transfer reaction in the $^{12}C + ^{16}O$ system using the semi-microscopic algebraic cluster model. *The European Physical Journal A*, 55(6), 2019.

[51] S. Y. Torilov, N. A. Maltsev, and V. I. Zherebchevsky. Studying Low-Energy Resonances in the $^{12}C + ^{16}O$ system. *Bulletin of the Russian Academy of Sciences: Physics*, 85(5):548–551, 2021.

[52] Y.-D. Chan, H. Bohn, R. Vandenbosch, R. Sielemann, J. G. Cramer, K. G. Bernhardt, H. C. Bhang, and D. T. Chiang. Influence of Extra Neutrons Added to the $^{12}C + ^{16}O$ System: Gross Structures in γ-ray Yields Following the $^{13}C + ^{16}O$ and $^{12}C + ^{18}O$ reactions. *Physical Review Letters*, 42(11):687–690, 1979.

[53] D. G. Kovar, D. F. Geesaman, T. H. Braid, Y. Eisen, W. Henning, T. R. Ophel, M. Paul, K. E. Rehm, S. J. Sanders, P. Sperr, and et al. Systematics of carbon- and oxygen-induced fusion on nuclei with $12 \leq A \leq 19$. *Physical Review C*, 20(4):1305–1331, 1979.

[54] B. Wang, Z. Ren, and D. Bai. $^{16-18}O + ^{16}O$ and $^{16,18}O + ^{12,13}C$ fusion-evaporation reactions at near-Coulomb-barrier energies from statistical model calculations. *Physical Review C*, 101(2), 2020.

[55] M. Assunção and P. Descouvemont. $^{12}C + ^{12}C$ and $^{16}O + ^{16}O$ fusion reactions at low energies. *Journal of Physics: Conference Series*, 590:012038, 2015.

[56] P. Descouvemont. Resonances in ^{12}C and ^{24}Mg: what do we learn from a microscopic cluster theory? *The European Physical Journal A*, 57(1), 2021.

[57] G. Montagnoli, A. M. Stefanini, C. L. Jiang, G. Colucci, A. Goasduff, D. Brugnara, M. Mazzocco, M. Siciliano, F. Scarlassara, L. Corradi, and et al. Study of fusion hindrance in the system $^{12}C + ^{24}Mg$. *Journal of Physics: Conference Series*, 1643(1):012098, 2020.

[58] G. P. Nobre, L. C. Chamon, L. R. Gasques, B. V. Carlson, and I. J. Thompson. Consistent analysis of fusion data without adjustable parameters for a wide variety of heavy-ion systems. *Physical Review C*, 75(4), 2007.

[59] N. Maroufi, V. Dehghani, and S. A. Alavi. Alpha and cluster decay of some deformed heavy and superheavy nuclei. *Nuclear Physics A*, 983:77–89, 2019.

[60] N. N. Le, N. N. Duy, and N. Q. Hung. Examination of α-induced fusion reactions relevant to the production of p-nuclei. *The European Physical Journal A*, 57(6), 2021.

[61] J. C. Lattanzio and M. A. Lugaro. What we do and do not know about the s-process in AGB stars. *Nuclear Physics A*, 758:477–484, 2005.

[62] F. Käppeler. s-Process nucleosynthesis and the interior of Red Giants. *Nuclear Physics A*, 752:500–509, 2005.

[63] S. Wanajo, M. Tamamura, N. Itoh, K. Nomoto, Y. Ishimaru, T. C. Beers, and S. Nozawa. The r-process in supernova explosions from the collapse of O-Ne-Mg cores. *The Astrophysical Journal*, 593(2):968–979, 2003.

[64] T. Suzuki, S. Shibagaki, T. Yoshida, T. Kajino, and T. Otsuka. β-decay Rates for Exotic Nuclei and r-process Nucleosynthesis up to Thorium and Uranium. *The Astrophysical Journal*, 859(2):133, 2018.

[65] S. E. Woosley and R. D. Hoffman. The alpha -Process and the r-Process. *The Astrophysical Journal*, 395:202, 1992.

[66] B. S. Meyer. r-Process Nucleosynthesis without Excess Neutrons. *Physical Review Letters*, 89(23), 2002.

[67] B. S. Meyer, G. C. McLaughlin, and G. M. Fuller. Neutrino capture and r-process nucleosynthesis. *Physical Review C*, 58(6):3696–3710, 1998.

[68] Y.-Z. Qian, P. Vogel, and G. J. Wasserburg. Probing r-process production of nuclei beyond ^{209}Bi with gamma rays. *The Astrophysical Journal*, 524(1):213–219, 1999.

[69] K. Langanke, G. Martínez-Pinedo, and R. G. Zegers. Electron capture in stars. *Reports on Progress in Physics*, 84(6):066301, 2021.

[70] J. R. De Laeter. Abundances for p-process nucleosynthesis. *Physical Review C*, 77(4), 2008.

[71] B. Cai, G. Chen, C. Yuan, and H. Jian-Jun. Shell-model study on properties of proton dripline nuclides with Z, N = 30-50 including uncertainty analysis. *Chinese Physics C*, 2022.

[72] G. G. Kiss, T. Szücs, G. Gyürky, Z. Fülöp, J. Farkas, Z. Kertész, E. Somorjai, M. Laubenstein, C. Fröhlich, T. Rauscher, and et al. Activation method combined with characteristic X-ray counting: A possibility to measure (α, γ) cross sections on heavy p-nuclei. *Nuclear Physics A*, 867(1):52–65, 2011.

[73] S. Harissopulos, A. Lagoyannis, A. Spyrou, C. Zarkadas, S. Galanopoulos, G. Perdikakis, H.-W. Becker, C. Rolfs, F. Strieder, R. Kunz, and et al. Proton and alpha-particle capture reactions at sub-Coulomb energies relevant to the p process. *Journal of Physics G: Nuclear and Particle Physics*, 31(10), 2005.

[74] S. Harissopulos, A. Spyrou, A. Lagoyannis, C. Zarkadas, H.-W. Becker, C. Rolfs, F. Strieder, J. W. Hammer, A. Dewald, K.-O. Zell, and et al. Systematic measurements of proton- and alpha-capture cross sections relevant to the modelling of the p process. *Nuclear Physics A*, 758:505–508, 2005.

[75] S. J. Quinn, A. Spyrou, A. Simon, A. Battaglia, M. Couder, P. A. DeYoung, A. C. Dombos, X. Fang, J. Görres, A. Kontos, and et al. Probing the production mechanism of the light p-process nuclei. *Physical Review C*, 88(1), 2013.

[76] H. Schatz, A. Aprahamian, V. Barnard, L. Bildsten, A. Cumming, M. Ouellette, T. Rauscher, F.-K. Thielemann, and M. Wiescher. End Point of the rp Process on Accreting Neutron Stars. *Physical Review Letters*, 86(16):3471–3474, 2001.

[77] B. A. Brown, R. R. Clement, H. Schatz, A. Volya, and W. A. Richter. Proton drip-line calculations and the rp process. *Physical Review C*, 65(4), 2002.

[78] G. G. Adamian and N. V. Antonenko. Optimal ways to produce heavy and superheavy nuclei. *The European Physical Journal A*, 58(6), 2022.

[79] A. Arcones, D. W. Bardayan, T. C. Beers, L. A. Bernstein, J. C. Blackmon, B. Messer, B. A. Brown, E. F. Brown, C. R. Brune, A. E. Champagne, and et al. White paper on nuclear astrophysics and low energy nuclear physics Part 1: Nuclear astrophysics. *Progress in Particle and Nuclear Physics*, 94:1–67, 2017.

[80] J. Carlson, M. P. Carpenter, R. Casten, C. Elster, P. Fallon, A. Gade, C. Gross, G. Hagen, A. C. Hayes, D. W. Higinbotham, and et al. White paper on nuclear astrophysics and low-energy nuclear physics, Part 2: Low-energy nuclear physics. *Progress in Particle and Nuclear Physics*, 94:68–124, 2017.

[81] L. E. Marcucci, K. M. Nollett, R. Schiavilla, and R. B. Wiringa. Modern theories of low-energy astrophysical reactions. *Nuclear Physics A*, 777:111–136, 2006.

[82] T. Neff, H. Feldmeier, and K. Langanke. Towards microscopic ab initio calculations of astrophysical S-factors. *Progress in Particle and Nuclear Physics*, 66(2):341–345, 2011.

[83] P. Navrátil, S. Quaglioni, G. Hupin, C. Romero-Redondo, and A. Calci. Unified *ab initio* approaches to nuclear structure and reactions. *Physica Scripta*, 91(5):053002, 2016.

[84] P. Navratil, C. A. Bertulani, and E. Caurier. ^{7}Be(p,γ)^{8}B S-factor from ab *initio* wave functions. *Journal of Physics: Conference Series*, 49:15–20, 2006.

[85] M. C. Atkinson, P. Navrátil, G. Hupin, K. Kravvaris, and S. Quaglioni. *Ab initio* calculation of the β decay from ^{11}Be to a $^{10}\mathrm{Be} + p$ resonance. *Physical Review C*, 105(5), 2022.

[86] K. Arai, S. Aoyama, Y. Suzuki, P. Descouvemont, and D. Baye. Tensor force manifestations in *ab initio* study of the ^{2}H(d, γ)^{4}He, ^{2}H(d, p)^{3}H and ^{2}H(d, n)^{3}He reactions. *Journal of Physics: Conference Series*, 436:012024, 2013.

[87] B. R. Barrett, P. Navrátil, and J. P. Vary. *Ab Initio* no core shell model. *Progress in Particle and Nuclear Physics*, 69:131–181, 2013.

[88] L. V. Grigorenko, B. V. Danilin, V. D. Efros, N. B. Shul'gina, and M. V. Zhukov. Structure of the ^{8}Li and ^{8}B nuclei in an extended three-body model and astrophysical S_{17} factor. *Physical Review C*, 57(5), 1998.

[89] J. Dohet-Eraly, P. Navrátil, S. Quaglioni, W. Horiuchi, G. Hupin, and F. Raimondi. ^{3}He$(\alpha,\gamma)^7$Be and ^{3}H$(\alpha,\gamma)^7$Li astrophysical S factors from the no-core shell model with continuum. *Physics Letters B*, 757:430–436, 2016.

[90] H. Jayatissa, M. L. Avila, K. E. Rehm, R. Talwar, P. Mohr, K. Auranen, J. Chen, D. A. Gorelov, C. R. Hoffman, C. L. Jiang, and et al. First direct measurement of the ^{13}N$(\alpha,\mathrm{p})^{16}$O reaction relevant for core-collapse supernovae nucleosynthesis. *Physical Review C*, 105(4), 2022.

[91] N. Le Anh and B. Minh Loc. Low-energy ^{7}Li(n, γ)^{8}Li and ^{7}Be(p, γ)^{8}B radiative capture reactions within the Skyrme Hartree-Fock approach. *Physical Review C*, 106(1), 2022.

[92] E. G. Adelberger, A. García, R. G. Robertson, K. A. Snover, A. B. Balantekin, K. Heeger, M. J. Ramsey-Musolf, D. Bemmerer, A. Junghans, C. A. Bertulani, and et al. Solar fusion cross sections. II. The *pp* chain and CNO cycles. *Reviews of Modern Physics*, 83(1):195–245, 2011.

[93] C. Beck. *Clusters in nuclei, vol. 2.* Springer Berlin Heidelberg, 2012.

[94] M. Freer, H. Horiuchi, Y. Kanada-En'yo, D. Lee, and U.-G. Meißner. Microscopic clustering in light nuclei. *Reviews of Modern Physics*, 90(3), 2018.

[95] D. Bai and Z. Ren. Woods-Saxon-Gaussian potential and alpha-cluster structures of alpha + closed shell nuclei. *Chinese Physics C*, 42(12):124102, 2018.

[96] G. X. Dong, X. B. Wang, N. Michel, and M. Płoszajczak. Gamow shell model description of the radiative capture reaction ^{8}Li(n, γ)^{9}Li. *Physical Review C*, 105(6), 2022.

[97] T. Tazawa. Nucleus-Nucleus potential in the Two-Center Shell Model. *Progress of Theoretical Physics*, 51(6):1764–1782, 1974.

[98] M. Dufour and P. Descouvemont. Multicluster study of the ^{12}C + n and ^{12}C + p systems. *Physical Review C*, 56(4):1831–1839, 1997.

[99] C. Simenel, R. Keser, A. S. Umar, and V. E. Oberacker. Microscopic study of ^{16}O + ^{16}O fusion. *Physical Review C*, 88(2), 2013.

[100] Shubhchintak and P. Descouvemont. Breakup effects in the ^{16}C + p and ^{16}C + d reactions. *Physical Review C*, 105(2), 2022.

[101] T. Baba, Y. Taniguchi, and M. Kimura. 4α linear-chain state produced by ^{9}Be + ^{9}Be collisions. *Physical Review C*, 105(6), 2022.

[102] A. M. Lane and R. G. Thomas. R-matrix theory of nuclear reactions. *Reviews of Modern Physics*, 30(2):257–353, 1958.

[103] P. Descouvemont and D. Baye. The *R*-matrix theory. *Reports on Progress in Physics*, 73(3):036301, 2010.

[104] J. Humblet. K-matrix analysis of resonance nuclear reactions. *Physical Review C*, 42(4):1582–1591, 1990.

[105] C. R. Brune. Alternative parametrization of R-matrix theory. *Physical Review C*, 66(4), 2002.

[106] D. F. Ramírez Jiménez and N. G. Kelkar. Different manifestations of S-matrix poles. *Annals of Physics*, 396:18–43, 2018.

[107] R. S. de Souza, C. Iliadis, and A. Coc. Astrophysical S-factors, Thermonuclear Rates, and Electron Screening Potential for the ^{3}He(d, p)^{4}He Big Bang Reaction via a Hierarchical Bayesian Model. *The Astrophysical Journal*, 872(1):75, 2019.

[108] R. Spartá, R. G. Pizzone, C. A. Bertulani, S. Hou, L. Lamia, and A. Tumino. Direct and Indirect Measurements for a Better Understanding of the Primordial Nucleosynthesis. *Frontiers in Astronomy and Space Sciences*, 7, 2020.

[109] D. Odell, C. R. Brune, and D. R. Phillips. How bayesian methods can improve R-matrix analyses of data: The example of the dt reaction. *Physical Review C*, 105(1), 2022.

[110] J. Grineviciute, L. Lamia, A. M. Mukhamedzhanov, C. Spitaleri, and M. La Cognata. Low-energy R-matrix fits for the ^{6}Li(d, α)^{4}He S factor. *Physical Review C*, 91(1), 2015.

[111] B. Vande Kolk, K. T. Macon, R. J. deBoer, T. Anderson, A. Boeltzig, K. Brandenburg, C. R. Brune, Y. Chen, A. M. Clark, T. Danley, and et al. Investigation of the ^{10}B(p, α)^{7}Be reaction from 0.8 to 2.0 MeV. *Physical Review C*, 105(5), 2022.

[112] A. Sieverding, J. S. Randhawa, D. Zetterberg, R. J. deBoer, T. Ahn, R. Mancino, G. Martínez-Pinedo, and W. R. Hix. Role of low-lying resonances for the ^{10}Be(p, α)^{7}Li reaction rate and implications for the formation of the Solar System. *Physical Review C*, 106(1), 2022.

[113] G. Kaur, V. Guimarães, J. C. Zamora, M. Assunção, J. Alcantara-Nuñez, A. L. de Lara, E. O. Zevallos, J. B. Ribeiro, R. Lichtenthäler, K. C. Pires, and et al. New resonances in ^{11}C above the ^{10}B+p threshold investigated by inverse kinematic resonant scattering. *Physical Review C*, 105(2), 2022.

[114] D. Schürmann, L. Gialanella, R. Kunz, and F. Strieder. The astrophysical S factor of ^{12}C(α, γ)^{16}O at stellar energy. *Physics Letters B*, 711(1):35–40, 2012.

[115] J.-M. Sparenberg. Hybrid potential/R-matrix models for the 12C + α system. *Nuclear Physics A*, 758:423–426, 2005.

[116] P. S. Prusachenko, T. L. Bobrovsky, I. P. Bondarenko, M. V. Bokhovko, A. F. Gurbich, and V. V. Ketlerov. Measurement of the cross section for the ^{13}C(α, n)^{16}O reaction and determination of the cross section for the ^{16}O(n, α)^{13}C reaction. *Physical Review C*, 105(2), 2022.

[117] N. Burtebaev, S. B. Igamov, R. J. Peterson, R. Yarmukhamedov, and D. M. Zazulin. New measurements of the astrophysical S factor for ^{12}C(p, γ)^{13}N reaction at low energies and the asymptotic normalization coefficient (nuclear vertex constant) for the $p + {}^{12}\mathrm{C} \to {}^{13}\mathrm{N}$ reaction. *Physical Review C*, 78(3), 2008.

[118] S. Chakraborty, R. deBoer, A. Mukherjee, and S. Roy. Systematic R-matrix analysis of the ^{13}C(p, γ)^{14}N capture reaction. *Physical Review C*, 91(4), 2015.

[119] G. Genard, P. Descouvemont, and G. Terwagne. S-factor measurement of the ^{13}C(p, γ)^{14}N reaction in reverse kinematics. *Journal of Physics: Conference Series*, 202:012015, 2010.

[120] F. C. Barker. ^{15}N(p, γ_0)^{16}O S factor. *Physical Review C*, 78(4), 2008.

[121] C. Angulo, A. E. Champagne, and H.-P. Trautvetter. R-matrix analysis of the $^{14}\mathrm{N}(\mathrm{p},\gamma)^{15}\mathrm{O}$ astrophysical S-factor. *Nuclear Physics A*, 758:391–394, 2005.

[122] A. Formicola, G. Imbriani, H. Costantini, C. Angulo, D. Bemmerer, R. Bonetti, C. Broggini, P. Corvisiero, J. Cruz, P. Descouvemont, and et al. Astrophysical S-factor of $^{14}\mathrm{N}(\mathrm{p},\gamma)^{15}\mathrm{O}$. *Physics Letters B*, 591(1-2):61–68, 2004.

[123] D. G. Yakovlev, M. Beard, L. R. Gasques, and M. Wiescher. Simple analytic model for astrophysical S factors. *Physical Review C*, 82(4), 2010.

[124] S. Dubovichenko and A. Dzhazairov-Kakhramanov. Examination of the astrophysical S-factors of the radiative proton capture on $^{2}\mathrm{H}$, $^{6}\mathrm{Li}$, $^{7}\mathrm{Li}$, $^{12}\mathrm{C}$ and $^{13}\mathrm{C}$. *International Journal of Modern Physics E*, 21(03):1250039, 2012.

[125] E. M. Tursunov, S. A. Turakulov, A. S. Kadyrov, and L. D. Blokhintsev. Astrophysical S factor and rate of $^{7}\mathrm{Be}(\mathrm{p},\gamma)^{8}\mathrm{B}$ direct capture reaction in a potential model. *Physical Review C*, 104(4), 2021.

[126] R. Bass. Nucleus-Nucleus Potential Deduced from Experimental Fusion Cross Sections. *Physical Review Letters*, 39(5):265–268, 1977.

[127] T. Nandi, D. K. Swami, P. S. Gupta, Y. Kumar, S. Chakraborty, and H. C. Manjunatha. Search for a viable nucleus–nucleus potential in heavy-ion nuclear reactions. *Pramana*, 96(2), 2022.

[128] J. T. Huang, C. A. Bertulani, and V. Guimarães. Radiative capture of nucleons at astrophysical energies with single-particle states. *Atomic Data and Nuclear Data Tables*, 96(6):824–847, 2010.

[129] C. A. Bertulani. $^{7}\mathrm{Be}(\mathrm{p},\gamma)^{8}\mathrm{B}$ cross section from indirect breakup experiments. *Zeitschrift für Physik A: Hadrons and Nuclei*, 356(1):293–297, 1996.

[130] A. Kabir and J.-U. Nabi. Re-examination of astrophysical S-factor of proton capture $^{9}\mathrm{Be}(\mathrm{p},\gamma)^{10}\mathrm{B}$ in stellar matter. *Nuclear Physics A*, 1007:122118, 2021.

[131] A. Kabir, B. F. Irgaziev, J.-U. Nabi, and S. Sagheer. Re-analysis of radiative capture $^{11}\mathrm{C}(\mathrm{p},\gamma)^{12}\mathrm{N}$ at low energy. *Journal of Physics G: Nuclear and Particle Physics*, 49(7):075101, 2022.

[132] P. Salamon, Á. Baran, and T. Vertse. Distributions of the S-matrix Poles in Woods–Saxon and cut-off Woods–Saxon potentials. *Nuclear Physics A*, 952:1–17, 2016.

[133] M. Singh, Sukhvinder, and R. Kharab. Analysis of fusion excitation functions of various systems using modified Woods–Saxon potential. *Nuclear Physics A*, 897:179–197, 2013.

[134] A. H. Amer and Y. E. Penionzhkevich. Elastic scattering analysis of isobar nuclei $A = 6$ projectiles on $^{12}\mathrm{C}$ using different models of optical potential. *Nuclear Physics A*, 1015:122300, 2021.

[135] D. L. Hill and J. A. Wheeler. Nuclear Constitution and the Interpretation of Fission Phenomena. *Physical Review*, 89(5):1102–1145, 1953.

[136] H. Esbensen. Structures in high-energy fusion data. *Physical Review C*, 85(6), 2012.

[137] W. H. Z. Cárdenas, L. F. Canto, R. Donangelo, M. S. Hussein, J. Lubian, and A. Romanelli. Approximations in fusion and breakup reactions induced by radioactive beams. *Nuclear Physics A*, 703(3-4):633–648, 2002.

[138] M. Singh, Sukhvinder, and R. Kharab. Analysis of fusion excitation function data by using an energy dependent potential model. *Nuclear Physics A*, 897:198–217, 2013.

[139] L. C. Chamon. The São Paulo potential. *Nuclear Physics A*, 787(1-4):198–205, 2007.

[140] R. Ghasemi and H. Sadeghi. S-factor for radiative capture reactions for light nuclei at astrophysical energies. *Results in Physics*, 9:151–165, 2018.

[141] S. B. Dubovichenko and A. V. Dzhazairov-Kakhramanov. Astrophysical S -factor of p^2H radiative capture. *The European Physical Journal A*, 39(2):139–143, 2009.

[142] K. Czerski, A. Huke, P. Heide, and G. Ruprecht. Experimental and theoretical screening energies for the $^2H(d,p)^3H$ reaction in metallic environments. *The European Physical Journal A*, 27(S1):83–88, 2006.

[143] A. Kabir, B. F. Irgaziev, and J.-U. Nabi. Radiative capture of proton by ^{13}C at low energy. *Astrophysics and Space Science*, 365(6), 2020.

[144] S. B. Dubovichenko. Astrophysical S-factor for the radiative-capture reaction $p^{13}C \to {}^{14}N\gamma$. *Physics of Atomic Nuclei*, 75(2):173–181, 2012.

[145] A. Diaz-Torres, L. R. Gasques, and M. Wiescher. Effects of nuclear molecular configurations on the astrophysical S-factor for $^{16}O + {}^{16}O$. *Physics Letters B*, 652(5-6):255–258, 2007.

[146] C. Spitaleri, A. M. Mukhamedzhanov, L. D. Blokhintsev, M. La Cognata, R. G. Pizzone, and A. Tumino. The Trojan Horse Method in Nuclear Astrophysics. *Physics of Atomic Nuclei*, 74(12):1725–1739, 2011.

[147] H. Sadeghi, H. Khalili, and M. Godarzi. Astrophysical S-factor of the $d(p,\gamma)^3He$ process by effective field theory. *Chinese Physics C*, 37(4):044102, 2013.

[148] R. Higa, P. Premarathna, and G. Rupak. Coupled-channels treatment of $^7Be(p,\gamma)^8B$ in effective field theory. *Physical Review C*, 106(1), 2022.

[149] M. Beard, A. V. Afanasjev, L. C. Chamon, L. R. Gasques, M. Wiescher, and D. G. Yakovlev. Astrophysical S factors for fusion reactions involving C, O, Ne, and Mg isotopes. *Atomic Data and Nuclear Data Tables*, 96(5):541–566, 2010.

[150] B. K. Jennings, S. Karataglidis, and T. D. Shoppa. Direct capture astrophysical S factors at low energy. *Physical Review C*, 58(1):579–581, 1998.

[151] M. I. Hussein and R. H. Abdullah. Calculation of astrophysical S-factor and thermonuclear reaction rates for (p,n) medium elements reactions. *Journal of Physics: Conference Series*, 1660(1):012102, 2020.

[152] M. Ueda, A. J. Sargeant, M. P. Pato, and M. S. Hussein. Evaluation of effective astrophysical S factor for non-resonant reactions. *Progress of Theoretical Physics Supplement*, 146:634–635, 2002.

[153] M. Ueda, A. J. Sargeant, M. P. Pato, and M. S. Hussein. Resonances and thermonuclear reaction rates for charged particle collisions. *Physical Review C*, 70(2), 2004.

[154] G. V. Rossum and F. L. Drake. *Python 3: Reference Manual*. SohoBooks, 2009.

[155] W. McKinney. *9th Python in Science Conference*, page 56–61. Scipy, 2010. Editors Stéfan van der Walt and Jarrod Millman.

[156] C. R. Harris, K. J. Millman, S. J. van der Walt, R. Gommers, P. Virtanen, D. Cournapeau, E. Wieser, J. Taylor, S. Berg, N. J. Smith, and et al. Array programming with NumPy. *Nature*, 585(7825):357–362, 2020.

[157] P. Virtanen, R. Gommers, T. E. Oliphant, M. Haberland, T. Reddy, D. Cournapeau, E. Burovski, P. Peterson, W. Weckesser, J. Bright, and et al. Scipy 1.0: Fundamental algorithms for scientific computing in Python. *Nature Methods*, 17(3):261–272, 2020.

[158] J. D. Hunter. Matplotlib: A 2D Graphics Environment. *Computing in Science & Engineering*, 9(3):90–95, 2007.

[159] P. Descouvemont, A. Adahchour, C. Angulo, A. Coc, and E. Vangioni-Flam. Compilation and R-matrix analysis of Big Bang nuclear reaction rates. *Atomic Data and Nuclear Data Tables*, 88(1):203–236, 2004.

[160] V. V. Zerkin, B. Pritychenko, J. Totans, L. Vrapcenjak, A. Rodionov, and G. I. Shulyak. EXFOR-NSR PDF database: A system for nuclear knowledge preservation and data curation. *Journal of Instrumentation*, 17(03), 2022.

[161] V. M. Bystritsky, V. V. Gerasimov, A. R. Krylov, S. S. Parzhitskii, G. N. Dudkin, V. L. Kaminskii, B. A. Nechaev, V. N. Padalko, A. V. Petrov, G. A. Mesyats, and et al. Study of the pd reaction in the astrophysical energy region using the Hall accelerator. *Nuclear Instruments and Methods in Physics Research Section A: Accelerators, Spectrometers, Detectors and Associated Equipment*, 595(3):543–548, 2008.

[162] G. J. Schmid, R. M. Chasteler, C. M. Laymon, H. R. Weller, R. M. Prior, and D. R. Tilley. Polarized proton capture by deuterium and the $^2\mathrm{H}(\mathrm{p},\gamma)^3\mathrm{He}$ astrophysical S factor. *Physical Review C*, 52(4), 1995.

[163] B. L. Berman, L. J. Koester, and J. H. Smith. Photodisintegration of He^3. *Physical Review*, 133(1B), 1964.

[164] J. B. Warren, K. L. Erdman, L. P. Robertson, D. A. Axen, and J. R. Macdonald. Photodisintegration of He^3 near the Threshold. *Physical Review*, 132(4):1691–1692, 1963.

[165] U. Greife, F. Gorris, M. Junker, C. Rolfs, and D. Zahnow. Oppenheimer-Phillips effect and electron screening in $d+d$ fusion reactions. *Zeitschrift für Physik A Hadrons and Nuclei*, 351(1):107–112, 1995.

[166] A. Krauss, H. W. Becker, H. P. Trautvetter, C. Rolfs, and K. Brand. Low-energy fusion cross sections of $\mathrm{D}+\mathrm{D}$ and $\mathrm{D}+{}^3\mathrm{He}$ reactions. *Nuclear Physics A*, 465(1):150–172, 1987.

[167] D. S. Leonard, H. J. Karwowski, C. R. Brune, B. M. Fisher, and E. J. Ludwig. Precision measurements of precision measurements of $^2\mathrm{H}(\mathrm{d},\mathrm{p})^3\mathrm{H}$ and $^2\mathrm{H}(\mathrm{d},\mathrm{n})^3\mathrm{He}$ total cross sections at Big Bang nucleosynthesis energies. *Physical Review C*, 73(4), 2006.

[168] R. L. Schulte, M. Cosack, A. W. Obst, and J. L. Weil. $^2\mathrm{H}$ + reactions from 1.96 to 6.20 MeV. *Nuclear Physics A*, 192(3):609–624, 1972.

[169] A. Tumino, C. Spitaleri, A. M. Mukhamedzhanov, S. Typel, M. Aliotta, V. Burjan, M. Gimenez del Santo, G. G. Kiss, V. Kroha, Z. Hons, and et al. Low-energy $\mathrm{d}+\mathrm{d}$ fusion reactions via the Trojan Horse method. *Physics Letters B*, 700(2):111–115, 2011.

[170] C. Casella, H. Costantini, A. Lemut, B. Limata, R. Bonetti, C. Broggini, L. Campajola, P. Corvisiero, J. Cruz, A. D'Onofrio, and et al. First measurement of the $\mathrm{d}(\mathrm{p},\gamma)^3\mathrm{He}$ cross section down to the solar Gamow peak. *Nuclear Physics A*, 706(1-2):203–216, 2002.

[171] V. N. Fetisov, A. N. Gorbunov, and A. T. Varfolomeev. Nuclear photoeffect on three-particle nuclei. *Nuclear Physics*, 71(2):305–342, 1965.

[172] K. N. Geller, E. G. Muirhead, and L. D. Cohen. The $^2\mathrm{H}(\mathrm{p},\gamma)^3\mathrm{He}$ reaction at the breakup threshold. *Nuclear Physics A*, 96(2):397–400, 1967.

[173] G. M. Griffiths, E. A. Larson, and L. P. Robertson. The capture of protons by deuterons. *Canadian Journal of Physics*, 40(4):402–411, 1962.

[174] L. Ma, H. J. Karwowski, C. R. Brune, Z. Ayer, T. C. Black, J. C. Blackmon, E. J. Ludwig, M. Viviani, A. Kievsky, R. Schiavilla, and et al. Measurements of ^{1}H$(\vec{d},\gamma)^3$He and ^{2}H$(\vec{p},\gamma)^3$He at very low energies. *Physical Review C*, 55(2):588–596, 1997.

[175] G. J. Schmid, M. Viviani, B. J. Rice, R. M. Chasteler, M. A. Godwin, G. C. Kiang, L. L. Kiang, A. Kievsky, C. M. Laymon, R. M. Prior, and et al. Effects of Non-nucleonic Degrees of freedom in the D$(\vec{p},\gamma)^3$He and $p(\vec{d},\gamma)^3$He Reactions. *Physical Review Letters*, 76(17):3088–3091, 1996.

[176] W. Wölfli, R. Bösch, J. Lang, R. Müller, and P. Marmier. Einfang von Protonen durch Deuteronen. *Helvetica Physica Acta*, 40:946–972, 1967.

[177] L. T. Baby, C. Bordeanu, G. Goldring, M. Hass, L. Weissman, V. N. Fedoseyev, U. Köster, Y. Nir-El, G. Haquin, H. W. Gäggeler, R. Weinreich, and et al. New measurement of the proton capture rate on ^{7}Be and the $S_{17}(0)$ factor. *Physical Review C*, 67(6), 2003.

[178] A. R. Junghans, E. C. Mohrmann, K. A. Snover, T. D. Steiger, E. G. Adelberger, J. M. Casandjian, H. E. Swanson, L. Buchmann, S. H. Park, A. Zyuzin, and et al. Precise measurement of the ^{7}Be$(\mathrm{p},\gamma)^8$B S factor. *Physical Review C*, 68(6), 2003.

[179] A. R. Junghans, K. A. Snover, E. C. Mohrmann, E. G. Adelberger, and L. Buchmann. Updated S factors for the ^{7}Be$(\mathrm{p},\gamma)^8$B reaction. *Physical Review C*, 81(1), 2010.

[180] F. Schümann, S. Typel, F. Hammache, K. Sümmerer, F. Uhlig, I. Böttcher, D. Cortina, A. Förster, M. Gai, H. Geissel, and et al. Low-energy cross section of the ^{7}Be$(\mathrm{p},\gamma)^8$B solar fusion reaction from the Coulomb dissociation of ^{8}B. *Physical Review C*, 73(1), 2006.

[181] J. D. King, R. E. Azuma, J. B. Vise, J. Görres, C. Rolfs, H. P. Trautvetter, and A. E. Vlieks. Cross section and astrophysical S-factor for the ^{13}C$(\mathrm{p},\gamma)^{14}$N reaction. *Nuclear Physics A*, 567(2):354–376, 1994.

[182] E. J. Woodbury and W. A. Fowler. The Cross Section for the Radiative Capture of Protons by C^{13} at 129 kev. *Physical Review*, 85(1):51–57, 1952.

[183] H. W. Becker, K. U. Kettner, C. Rolfs, and H. P. Trautvetter. The ^{12}C + ^{12}C reaction at subcoulomb energies (II). *Zeitschrift für Physik A Atoms and Nuclei*, 303(4):305–312, 1981.

[184] G. Fruet, S. Courtin, M. Heine, D. G. Jenkins, P. Adsley, A. Brown, R. Canavan, W. N. Catford, E. Charon, D. Curien, and et al. Advances in the Direct Study of Carbon Burning in Massive Stars. *Physical Review Letters*, 124(19), 2020.

[185] T. Spillane, F. Raiola, C. Rolfs, D. Schürmann, F. Strieder, S. Zeng, H.-W. Becker, C. Bordeanu, L. Gialanella, M. Romano, and et al. ^{12}C + ^{12}C Fusion Reactions near the Gamow Energy. *Physical Review Letters*, 98(12), 2007.

[186] W. P. Tan, A. Boeltzig, C. Dulal, R. J. deBoer, B. Frentz, S. Henderson, K. B. Howard, R. Kelmar, J. J. Kolata, J. Long, and et al. New Measurement of ^{12}C + ^{12}C Fusion Reaction at Astrophysical Energies. *Physical Review Letters*, 124(19), 2020.

[187] H. Spinka and H. Winkler. Experimental determination of the total reaction cross section of the stellar nuclear reaction ^{16}O + ^{16}O. *Nuclear Physics A*, 233(2):456–494, 1974.

[188] R. Buompane, A. Di Leva, L. Gialanella, A. D'Onofrio, M. De Cesare, J. G. Duarte, Z. Fülöp, L. R. Gasques, G. Gyürky, L. Morales-Gallegos, and et al. Determination of the ^{7}Be$(\mathrm{p},\gamma)^8$B cross section at astrophysical energies using a radioactive ^{7}Be ion beam. *Physics Letters B*, 824:136819, 2022.

[189] D. Gaspard. Connection formulas between Coulomb wave functions. *Journal of Mathematical Physics*, 59(11):112104, 2018.

[190] G. A. Watson and J. J. Moré. *The Levenberg-Marquardt algorithm: Implementation and theory*, volume 630 of *Lecture Notes in Mathematics*, page 105–116. Springer Berlin Heidelberg, 1978.

[191] D. Ramadasan, M. Chevaldonné, and T. Chateau. LMA: A generic and efficient implementation of the Levenberg-Marquardt Algorithm. *Software: Practice and Experience*, 47(11):1707–1727, 2017.

[192] M. A. Branch, T. F. Coleman, and Y. Li. A Subspace, Interior, and Conjugate Gradient Method for Large-Scale Bound-Constrained Minimization Problems. *SIAM Journal on Scientific Computing*, 21(1):1–23, 1999.

[193] T. F. Coleman and Y. Li. On the convergence of interior-reflective Newton methods for nonlinear minimization subject to bounds. *Mathematical Programming*, 67(1-3):189–224, 1994.

[194] L. C. Chamon, B. V. Carlson, and L. R. Gasques. São Paulo potential version 2 (SPP2) and Brazilian nuclear potential (BNP). *Computer Physics Communications*, 267:108061, 2021.

[195] A. Diaz-Torres. OWL: A code for the two-center shell model with spherical Woods–Saxon potentials. *Computer Physics Communications*, 224:381–386, 2018.

[196] I. I. Gontchar and M. V. Chushnyakova. DFMSPH14: A C-code for the double folding interaction potential of two spherical nuclei. *Computer Physics Communications*, 206:97–102, 2016.

[197] P. Descouvemont. An R-matrix package for coupled-channel problems in nuclear physics. *Computer Physics Communications*, 200:199–219, 2016.

[198] I. J. Thompson, R. J. deBoer, P. Dimitriou, S. Kunieda, M. T. Pigni, G. Arbanas, H. Leeb, T. Srdinko, G. Hale, P. Tamagno, and et al. Verification of R-matrix calculations for charged-particle reactions in the resolved resonance region for the ^{7}Be system. *The European Physical Journal A*, 55(6), 2019.

[199] R. E. Azuma, E. Uberseder, E. C. Simpson, C. R. Brune, H. Costantini, R. J. de Boer, J. Görres, M. Heil, P. J. LeBlanc, C. Ugalde, and et al. Azure: An R-matrix code for nuclear astrophysics. *Physical Review C*, 81(4), 2010.

[200] F. Salvat and J. M. Fernández-Varea. RADIAL: A Fortran subroutine package for the solution of the radial Schrödinger and Dirac wave equations. *Computer Physics Communications*, 240:165–177, 2019.

[201] K. Hagino, N. Rowley, and A. T. Kruppa. A program for coupled-channel calculations with all order couplings for heavy-ion fusion reactions. *Computer Physics Communications*, 123(1-3):143–152, 1999.